Expedition 314 Site C0004[1]

Expedition 314 Scientists[2]

Chapter contents

Background and objectives

Integrated Ocean Drilling Program (IODP) Site C0004 (proposed Site NT2-01I) targets the uppermost 400 meters below seafloor at the seaward edge of the Kumano Basin uplift (outer arc high) where the megasplay fault system branches and approaches the surface (Figs. **F1**, **F2**). The Site C0004 summary log diagram is shown in Figure **F1**. Both inline and cross-line three-dimensional (3-D) seismic lines crossing Site C0004 are shown in Figure **F2.** Locations of drill holes at Site C0004 are plotted in Figure **F3** with 3-D seismic profile coverage.

The primary objective of drilling at the NT2-01 series of proposed sites was to access the shallow portion of the megasplay fault system and the thrust sheets uplifted by it, as well as a thin overlying slope sediment cover sequence. The nature of the material in these thrust sheets is unknown. The acoustically nonreflective nature of this section suggests that it may be composed of chaotically deformed accretionary wedge sedimentary mélange transported from significantly greater depth. After drilling at Site C0003 failed to reach the fault reflector objective, Site C0004 was selected for a second attempt to drill and log across the fault zone and associated hanging wall and footwall structures.

The principal objective was to obtain in situ density, resistivity, gamma ray, porosity, *P*-wave velocity, and photoelectric factor data through logging while drilling (LWD) and seismic while drilling at this site. Together with later core samples, logs from this zone will verify our initial interpretations and provide data on physical properties, strength, composition, and structure of the megasplay fault zone and adjacent domains.

At Site C0004, we drilled into the toe of a thrust wedge in the hanging wall of the megasplay fault system along Inline 2675 of the Kumano 3-D seismic volume (Moore et al., 2007). The thrust wedge is draped by a ~70 m thick cover of hemipelagic slope sediments and is thrust over older slope sediments (Fig. **F2A, F2B**). The upper boundary of the wedge is a continuous reflection in the inline direction but is less continuous in the cross-line direction. Faint low-amplitude northwest-dipping reflections within the wedge are interpreted as thrust faults that intersect the thrust splay. A ~40 m thick zone below and parallel to the splay fault is interpreted as a fault zone. A strong reflection separates the fault zone from the underlying slope sediment section.

[1]Expedition 314 Scientists, 2009. Expedition 314 Site C0004. *In* Kinoshita, M., Tobin, H., Ashi, J., Kimura, G., Lallemant, S., Screaton, E.J., Curewitz, D., Masago, H., Moe, K.T., and the Expedition 314/315/316 Scientists, *Proc. IODP,* 314/315/316: Washington, DC (Integrated Ocean Drilling Program Management International, Inc.). doi:10.2204/iodp.proc.314315316.116.2009
[2]**Expedition 314/315/316 Scientists' addresses.**

doi:10.2204/iodp.proc.314315316.116.2009

Operations

Hole C0004A

After confirming the position at 0430 h on 31 October 2007, an 8½ inch pilot hole was spudded without logging tools at 0445 h on 1 November. The hole was jetted-in from the seafloor to 75.5 m drillers depth below seafloor (DSF), and rotary drilling began from that depth. During drilling, a short wiper trip was made between 2888 and 2736 m drillers depth below rig floor (DRF). Total depth (TD) of 400 meters below seafloor was reached at 1845 h and the bottom-hole assembly (BHA) was pulled out of the hole and reached the rig floor at 0345 h on 2 November.

Hole C0004B

The drill string was made up in preparation for drilling from 0515 to 0800 h on 2 November 2007. Like the previous LWD-measurement while drilling (MWD)-annular pressure while drilling (APWD) holes, the LWD tools (6¾ inch [17.15 cm] collars) included the geoVISION resistivity tool with a 23.18 cm button sleeve, sonicVISION tool, MWD (PowerPulse) tool, seismicVISION tool, and adnVISION tool run without a radioactive source for ultrasonic caliper only (see Fig. **F1** in the "Expedition 314 methods" chapter). A summary of operations is given in Table **T1,** and the full BHA is described in Table **T2.**

Following the standard procedure, the tools were assembled, and a first shallow communication and function check was conducted between 0830 and 0845 h. The BHA was immediately lowered while the remotely operated vehicle (ROV) was launched (1415 h on 2 November) and the D/V *Chikyu* moved 2000 m upcurrent. From 1415 to 1845 h, the *Chikyu* slowly drifted to the spud-in position while the bit was lowered. After tagging the seafloor at 2665.5 m DRF (2637 meters below sea level), the hole position was located and surveyed by ROV.

Hole C0002B was jetted-in from 2666.5 to 2726 m DRF (0–60.5 m LWD depth below seafloor [LSF]) at 1845 h on 2 November with an initial surface pump rate of 500–510 gpm (~1900 L/m) and surface pump pressure of 8–9 MPa. Drilling continued with an average rate of penetration (ROP) of ~40 m/h above 100 m LSF and reduced to 30 m/h below. Surface weight on bit (SWOB) was set to minimal values (mostly <150 kkgf) and no torque was observed (<3 kNm). Drilling progressed with normal collar rotation (80 rpm) while surface pump flow progressively increased with depth (700 gpm; ~2650 L/m) with pump pressure (SPPA; 8–12 MPa). At 234 m LSF (2900 m DRF) a short wiper trip was conducted to 99 m LSF (from 0330 to 0430 h on 3 November; 2765 m DRF). Drilling resumed from 234 m LSF to TD (400 m LSF; 3065 m DRF) with localized increase in SWOB (20 kkgf) and no increase in torque. At 1230 h on 3 November, two joints of pipe were removed to create an offset in uphole check shots at every pipe disconnection, and tools were pulled out of the hole. All LWD tools were recovered on the rig floor at 0000 h on 4 November, and all memory data were successfully downloaded. Time versions of the surface drilling parameters and downhole equivalent circulating density (ECD), average annular pressure (APRS), and real-time resistivity-at-the-bit gamma ray (GR_RAB_RT) values are given in Figure **F4.**

Transit to Site C0005

After recovering the ROV, the *Chikyu* moved to proposed Site NT2-01G over a distance of ~600 m with average speed of 0.3 kt at 0240 h on 6 November 2007 and checked the communication with beacons at the site at 0500 h.

Data and log quality

Hole C0004B

Available data

Hole C0004B was drilled with LWD-MWD-APWD tools. MWD-APWD data was transmitted in real time with a limited set of LWD data (see Table **T2** in the "Expedition 314 methods" chapter). Because the only radioactive source on board was cemented with the BHA at the previous site (see **"Operations"** in the "Expedition 314 Site C0003" chapter), density and porosity measurements could not be made. However, the adnVISION tool was deployed without the radioactive source to obtain ultrasonic caliper data. When LWD tools were recovered on the rig floor, memory data were successfully downloaded and processed according to the data flow described in **"Onboard data flow and quality check"** and Figure **F8** in the "Expedition 314 methods" chapter. A list of available LWD data is given in Table **T3** in the "Expedition 314 methods" chapter.

Depth shift

The mudline (seafloor) was identified from the first break in the gamma ray and resistivity logs (Fig. **F5**). In Hole C0004B, a mudline was picked at 2666 m DRF, showing a discrepancy of 0.5 m with drillers depth (2666.5 m DRF; 2637 m mud depth below sea level [MSL]). The depth-shifted versions of the main drilling data and geophysical logs are given in Figures **F6** and **F7,** respectively. Figure **F8** presents the time-depth relationship linking the time (Fig. **F4**) and the depth version (Figs. **F6, F7**) of the data in Hole C0004B.

Logging data quality

Figure F6 shows the drilling control logs. After jet-in to 60.5 m LSF, the initial target ROP of 40 m/h was generally achieved to ~100 m LSF where it was then reduced to 30 m/h to TD of 400 m LSF. SWOB was set to a minimal value (<5 kkgf for most of the drilled interval). SPPA was maintained at constant value (~15–18 MPa) for the entire drilling period, and a normal (hydrostatic) increasing trend in APRS and ECD was observed. The four ultrasonic azimuthal calipers (C15, C26, C37, and C48) showed bad borehole condition with washouts exceeding 2 inches (5.08 cm) in most places, except between 60 and 80 m and below 290 m LSF (last caliper reading at 370 m LSF). Because no density and porosity data were available, these washouts are of minor concern regarding the quality of the available logs.

The geophysical logs are shown in Figure F7. Time after bit (TAB) measurements for ultrasonic caliper logs are always <45 min. TAB measurements were ~5–10 min for the natural gamma ray log, except in a depth interval corresponding to pipe connections and the wiper trip (99–234 m LSF; 0330 to 0430 h on 3 November) where they exceeded 2 h. TAB measurements for resistivity were between 5 and 10 min. Comparison between deep button (RES_BD) and shallow button (RES_BS) resistivity values showed a larger separation, suggesting possible drilling fluid invasion.

The sonicVISION data for Hole C0004B were processed by the Schlumberger Data Consulting Specialist onboard the *Chikyu*. As a result of the processing, two products were delivered. The first product relies on a broad band-pass filter (10–16 kHz) on the data acquired during drilling, referred to as "wide." The second product relies on a very narrow band-pass filter (6–7 kHz) designed to pass only the "leaky-P" arrival applied to the data acquired during drilling. The composite sonic velocity curve prepared for this hole included data from both processed logs (Table T3). In the upper part of the hole (0–94.5 m LSF), the results of the leaky-P processed data were used. The leaky-P processed data were also used for intervals where the formation arrival could not be distinguished from the mud arrival. The wide data were the most reliable in the rest of the hole; therefore, these data were used to assemble the composite log from 94.5 to 389.5 m LSF (last sonicVISION value).

The quality control analysis of the sonic data is based on examination of the plots showing the sonic waveforms and the slowness coherence images for the common receiver data and the common source data. The full versions of these quality control plots are available as picture description standard format files in the raw data for the expedition. Examples of data of quality Types 0 and 1 are shown in "Data and log quality" section of the "Expedition 314 Site C0001" chapter.

As stated above, the uppermost 60.5 m LSF was jetted-in without tool rotation resulting in the lack of resistivity images for this interval. To ~100 m LSF, the ROP was significantly higher than in previous holes (40 versus 30 m/h). The images initially showed some pixel effect that was removed by post-processing (3 × 3 pixels up to 9 × 9 pixels smoothing filtering). The smoothing of the image did not blur the geological features. Unlike previous image data, no depth mismatches have been observed at this hole.

Resistivity images are of very good quality. The resistivity image log from Hole C0004A extends from 129 to 1398 m LSF (Table T4). Overall, the quality of the image data is excellent. The log is marked by three 1 m intervals of poor quality where the image is smeared, perhaps resulting from lack of rotation. A short interval of variable resistivity around the hole circumference occurs from 129 to 197 m, probably caused by hole eccentricity. Two features, absolutely horizontal with respect to the borehole, are suspected artifacts. Sharp changes in resistivity along knife-edge planar horizontal surfaces typically bound decimeter or thicker domains. Centimeter-scale horizontal variations in resistivity are also suspected to be artifacts because of their thinness, regularity, and horizontal orientation. Interpretation of resistivity image data is further discussed in "Structural geology and geomechanics" in the "Expedition 314 Site C0001" chapter.

Log characterization and lithologic interpretation

Log characterization and identification of logging units

Hole C0004B logging units were characterized through visual inspection of the gamma ray, resistivity, sonic velocity, and caliper log responses (Fig. F1). The resistivity images were used to define finer scale characteristics within the units. Three primary logging units were defined based on the variability of the log responses (Table T5).

Logging Unit I (0–67.9 m LSF) is characterized by low-frequency and high-amplitude variation of the gamma ray log (50–75 gAPI). This logging unit is also characterized by constant low ring resistivity values (0.8–1.1 Ωm) and highly variable deep resistivity responses ranging from 0.6 to 1.5 Ωm. Resistivity log values in the lower part of this logging unit (54–68 m LSF) decrease from 1.1 to 0.8 Ωm, ring resistivity

values increase from 0.8 to 1.0 Ωm, and the deep resistivity response increases from 0.8 to 1.2 Ωm with depth, with low-amplitude fluctuations (Fig. F1). The lowermost part of this logging unit is characterized by small borehole diameter values to as little as 8.9 inches. Logging Unit I correlates to slope sediments recognized in the seismic section (see "Log-seismic correlation").

Logging Unit II (67.9–323.8 m LSF) is divided into four subunits (Table T5). Logging Subunit IIA (67.9–96.2 m LSF) is characterized by high-frequency fluctuations in gamma ray value (55–75 gAPI) with an overall increasing trend. Ring resistivity values range from 1.0 to 1.3 Ωm, and deep resistivity values range from 1.3 to 1.8 Ωm. The sonic log shows a slight positive shift from 1570 to 1620 m/s at the top of this subunit. Caliper values increase from 9 to 10.5 inches through this subunit (Fig. F1).

Logging Subunit IIB (96.2–160.3 m LSF) is characterized by continuous high-frequency fluctuation in gamma ray values between 62 and 78 gAPI and constant ring resistivity values (1.1 and 1.5 Ωm). The deep, medium, and shallow resistivity logs significantly deviate from each other and exhibit strong fluctuations (Figs. F1, F9). The shallow resistivity log commonly exhibits strong conductive excursions to 0.7 Ωm throughout the subunit. The sonic log response shows a positive shift from 1660 to 1780 m/s at the top of the subunit and increases to 1890 m/s with depth.

Logging Subunit IIC (160.3–236.4 m LSF) is characterized by low-frequency and high-amplitude variations in gamma ray values (59–84 gAPI). The ring resistivity also exhibits high-amplitude variations (1.0 to 1.5 Ωm). The deep, medium, and shallow resistivity logs show similar trends to those in logging Subunit IIB, significantly deviating from each other and showing strong fluctuations. The shallow resistivity log commonly exhibits strong conductive excursions to 0.6 Ωm in this subunit. Sonic velocity values change from 1760 to 2005 m/s within logging Subunit IIC and increase slightly with depth.

Logging Subunit IID (236.4–323.8 m LSF) is characterized by a decreasing trend in gamma ray values (from 83 to 63 gAPI), with a minor increasing trend over a particular short interval (from 250 to 266 m LSF). The ring resistivity log exhibits large variations between 1.0 and 1.5 Ωm, with repeating intervals of decreasing values. The shallow, medium, and deep resistivity logs show similar trends to the ring resistivity log. The sonic velocity log exhibits a series of decreasing trends, punctuated by intervals with increasing values. There is a particularly sharp increase in sonic velocity values across the interval 283–298 m LSF, above an interval with gradually decreasing values (back to ~1985 m/s) (Fig. F1). This trend in sonic velocity log responses is not observed in any other subunit of logging Unit II or other logging units.

The boundary between logging Units II and III is based on changes in the resistivity and sonic velocity logs. A repeated decreasing trend in the ring resistivity in logging Subunit IID changes to a moderately variable trend in Unit III, and highly variable sonic velocity values in logging Subunit IID change to a normal increasing trend in Unit III (Fig. F1). The caliper baseline is shifted at this boundary from ~10.5 to 9.5 inches (Fig. F1). This boundary coincides with the lower limit of fractured Zone 8 (see "Structural geology and geomechanics").

Logging Unit III (323.8 m LSF to TD) is characterized by a decreasing trend in gamma ray values (74 to 60 gAPI) with a minor increasing trend over a short interval (337–350 m LSF). The resistivity logs exhibit moderately variable values (1.0 to 1.4 Ωm) for the ring resistivity and 1.1 to 1.6 Ωm for the deep resistivity. The sonic log shows a gradually increasing trend from 1980 to 2150 m/s with moderate fluctuations. The average borehole diameter in this logging unit is smaller than in logging Subunits IIB, IIC, and IID. Two distinct negative spikes in the resistivity log at 349–350 m LSF and 366–368 m LSF are interpreted as localized conductive fractures based on the borehole images (Fig. F1). Another negative spike in the resistivity, at 389–390 m LSF, corresponds to a negative spike in the gamma ray log, which is interpreted as a sand layer based on the borehole images. Logging Unit III is correlated to the underthrust sediments estimated from the seismic data (see "Log-seismic correlation").

Figure F10 illustrates the ring and deep resistivity, gamma ray, and sonic transit time (slowness) distributions for the logging units and subunits. The gamma ray and ring resistivity logs exhibit a similar trend of gradually increasing from logging Unit I to Subunit IIC then gradually decreasing to logging Unit III. The deep resistivity shows an increasing trend from logging Unit I to Subunit IIA and then gradually decreases with depth to logging Unit III. Figure F11 shows cross-plots of sonic velocity versus gamma ray and sonic velocity versus ring resistivity. Logging Subunit IIA is isolated from both logging Unit I and other subunits in logging Unit II in both plots. Logging Subunit IID is widely distributed and overlaps with logging Subunit IIC and Unit III in both plots.

Log-based lithologic interpretation

RAB image data from Hole C0004B show distinctive textural, sedimentary, and structural features (Fig.

F12). Deformation zones as defined in "Structural geology and geomechanics" at given depth intervals are easily recognizable in Figure F12 within logging Unit II as conductive bands. Internal trends of the gamma ray log show that each of the logging units, and to some degree the subunits, exhibit different trends. The most distinctive characteristics are observed in logging Unit I (0–67.9 m LSF) and Subunit IIC (160.3–236.4 m LSF).

Logging Unit I (slope sediments)

Logging Unit I exhibits two different trends. The upper ~30 m LSF exhibits low-frequency, decameter-scale fining-upward profiles, whereas the lower section exhibits higher frequency, meter-scale fining-upward profiles (Fig. F13). Across the logging Unit I/II boundary, the gamma ray log exhibits a near-constant baseline with only minor fluctuations in the ~6 m thick zone. From borehole images, southward-dipping well-stratified sediments with layering of centimeter to decameter scale are observed in logging Unit I. A conductive layer at the boundary between Unit I and Subunit IIA is presumed to be an unconformity (Fig. F14). The most likely lithology of logging Unit I is hemipelagic mud.

Logging Subunit IIA (mass transport deposits)

Although logging Subunit IIA can be correlated to the uppermost part of the wedge-shaped body with the major seismic reflector at ~70 m seismic depth below seafloor (SSF) forming its upper boundary, this subunit exhibits unique characters in facies and structure within logging Unit II. Logging Subunit IIA is obviously isolated from other subunits and units based on the cross-plot examination of sonic velocity versus gamma ray and sonic velocity versus ring resistivity (Fig. F11). No bedding surfaces or internal structures were identified from borehole images (Fig. F14). The structureless character with patchy texture suggests a chaotic, mixed, or deformed deposit, probably gravitational in origin.

Logging Subunit IIB (thrust sheet)

The uppermost interval of Subunit IIB (96.2–112.5 m LSF) corresponds to a fractured zone (Fig. F12) (see "Structural geology and geomechanics"). Image facies are characterized by several clear fractures and shear deformation with no clear bedding or sedimentary features throughout this interval. Below 112.5 m LSF, a few north–northeast dipping bedding planes can be identified and measured (Fig. F12). The most likely lithology of logging Subunit IIB is hemipelagic mudstone.

Logging Subunit IIC (thrust sheet)

Logging Subunit IIC is characterized by the difference observed in the gamma ray trends compared to logging Unit II above and below (Fig. F15). The baseline gamma ray value is slightly higher than the sections above and below and exhibits decameter-scale cycles dominated by fining-upward profiles, some of which have sharp bases, whereas others exhibit gradational coarsening-upward profiles. The subunits above and below logging Subunit IIC exhibit meter-scale variations of mostly fining-upward profiles, which have sharp bases (Fig. F15).

Based on interpretation of borehole images the upper part of Subunit IIC (160–190 m LSF) is strongly deformed and bedding features are not easily identified (Fig. F12). Over the interval 190–220 m LSF the formation is characterized by slightly higher resistivity values and weak deformation. Northwest-dipping bedding planes were measured consistently within this interval. The orientation of individual beds of relatively high resistivity can be identified and measured (e.g., at 204 m LSF), matching the general dip trend for this section. Below 220 m LSF bedding measurements indicate a slight change in orientation to northward dipping (Fig. F12). The log responses suggest that the lithology of logging Subunit IIC is hemipelagic mudstone.

Logging Subunit IID

The upper part of logging Subunit IID from 237–292 m LSF is a highly deformed zone. Although northward-dipping alternation of conductive–resistive layers are recognized locally in this interval, most of the original sedimentary features were disrupted at fractured Zones 6 (247–269 m LSF) and 7 (284–292 m LSF) (see "Structural geology and geomechanics"). The lower part of this subunit (292–324 m LSF) is weakly deformed. The angle of bedding dip changes from 20°–50° to <25° at ~298 m LSF (Fig. F12). In the interval 308–324 m LSF corresponding to fractured Zone 8 (see "Structural geology and geomechanics"), bedding-parallel shear zones are commonly observed as conductive bands. These sharp conductive bands can be easily distinguished from the surfaces of subtle alternating conductive–resistive beds. The most likely lithology of logging Subunit IID is hemipelagic mudstone.

Figure F16 shows the boundary between logging Units II and III. There is a distinct sandy interval of negative excursions in gamma ray, resistivity, and sonic velocity values at 311.7–312.6 m LSF. No significant washout is observed from the caliper log over this interval. The ring resistivity values exhibit

oscillation over the intervals 301–311 and 312–324 m LSF above and below the sand layer at 311–312 m LSF. This fluctuation zone is surrounded by stable intervals (294–301 and 324–337 m LSF). The caliper log exhibits high values to 12 inches over the intervals 306–311 and 312–324 m LSF above and below the sand layer. These intervals coincide with a zone of parallel low-angle conductive fractures (fractured Zone 8) and are surrounded by intervals of small borehole diameter (293–306 and 324–336 m LSF). These log responses and images look symmetrical around a central sand layer, which implies a localized deformation zone.

Logging Unit III (underthrust sediments)

Logging Unit III is characterized by reduced deformation. Alternating conductive–resistive bedding is common throughout the unit. Bedding dip in this unit is <25°, except for the base of the unit (~390 m LSF) where it reaches >30°. The top of this unit corresponds to the top of underthrusting sediments at 316 m SSF (see **"Log-seismic correlation"**). Taken together, all log responses suggest that the lithology of logging Unit III is hemipelagic mud with thin sandy layers.

Gamma ray value trends

The gamma ray values exhibited in logging Units I and II in Hole C0004B are very similar to those exhibited by logging Units I and II in Hole C0001D (Fig. **F17**). Considering the proximity of the two sites (Fig. **F2**) it is feasible that the slope sediments are similar in composition (logging Unit I from each site) and that the thrust sheet sediments are similar in composition (logging Unit II from each site). We suggest that the slope sediments at Site C0004 are muddy deposits with thin sand layers, whereas logging Unit II is composed of hemipelagic mud and silt.

Physical properties

This section presents the measurements available for physical property analyses at Site C0004. They include five different sets of resistivity logs (bit; ring; and shallow, medium, and deep button) and sonic log (DTCO) measurement for sonic *P*-wave velocity analysis. Since no radioactive source was available, no neutron porosity or density data were recorded.

As at previous sites, additional analyses were conducted to produce different porosities derived from resistivity. Accordingly, estimations of temperatures and formation factors were carried out.

Resistivity and estimated porosity

Resistivity logs

Figure **F9** shows the caliper log (CCAV; average of the four caliper measurements made at the same depth); ring and bit resistivity measurements; smoothed logs of shallow, medium, and deep button resistivity; and the result of the difference between shallow and deep button resistivity. A moving average using a 21-point (~3 m interval) window was used to smooth the resistivity values. It appears that the range of variation of resistivity is small (from 0.6 to 1.6 Ωm) (Fig. **F9, F18**). The superposition of the deep, medium, and shallow button resistivity measurements shows very good agreement between medium and deep button values. The shallow button measurement departs significantly from the two other button resistivities. A more detailed comparison shows that the deep resistivity is consistently greater than the shallow resistivity and the difference increases inside the fractured zones (Fig. **F9, F19**).

Based on bit resistivity, logging Unit I resistivity values gradually increase from 0.6 to 1.1 Ωm. The increase is steeper in logging Subunit IIA, where the resistivity value reaches 1.45 Ωm at the bottom of the zone. The slightly decreasing trend of resistivity values in Subunit IIB, from 1.4 to 1.3 Ωm, is followed by a slight increase of resistivity values at the bottom (from 140 to 160 m LSF the values vary from 1.2 to 1.4 Ωm). In Subunit IIC, resistivity generally increases from 1.3 to 1.5 Ωm, but the signal contains high-amplitude fluctuations from 1.4 to 1.2 Ωm with three zones of lower resistivity from 165 to 175, 182 to 189, and 210 to 221 m LSF, partly correlated with fractured zones. In Subunit IID the trend of resistivity decreases from 1.5 to 1.2 Ωm with a low-resistivity peak at 311 m LSF and two zones of lower resistivity values from 252 to 265 and 286 to 292 m LSF corresponding to two major fractured zones. In logging Unit III the resistivity trend slightly decreases and is affected by low-resistivity peaks that correlate well with single fractures at 349, 355, 376, and 390 m LSF. (Fig. **F9, F20**).

Estimation of temperature profile

The downhole temperature profile was estimated from a regional surface heat flow of 60 mW/m^2 (Kinoshita et al., 2003), and assuming 1 W/(m·K) thermal conductivity for the upper 68 m LSF and 1.3

W/(m·K) below and 2°C surface temperature. The estimated temperature is 21°C at 399 m LSF.

Estimation of porosity from resistivity

Bit and ring formation factors have been calculated from resistivity logs and temperature-corrected seawater electrical resistivity. They were converted to porosity using Archie's law. In the absence of neutron porosity data to calibrate Archie's law parameters, the same values of a = 1 and m = 2.4 as at the previous sites were used. It should be noted that lithologic variations not taken into account in this estimation could affect the resulting porosity, as could the choice of Archie's law constants.

The general trend of the resistivity-derived porosity log presents several intervals where the average value remains fairly constant (Fig. **F20**). Resistivity-derived porosity decreases from 65% at 6 m LSF to 58% at 54 m LSF. From 54 to 95 m LSF, resistivity-derived porosity decrease is steeper, from 58% to 52%. From 95 to 142 m LSF, resistivity-derived porosity remains nearly constant at 52%. Bit resistivity–derived porosity variations around this average value are <1% in amplitude (2.5% for ring resistivity–derived porosity). From 142 to 191 m LSF, the average resistivity-derived porosity value decreases to ~49%. The moderately fractured interval 170–184 m with conductive fractures corresponds to a low-porosity zone of ~51%. From 191 m LSF to the bottom of the hole, resistivity-derived porosity seems to fluctuate around an average value of 49%. Two intervals of anomalous resistivity-derived porosity can be observed from 207 to 264 m LSF: (1) a 23 m high-porosity interval with a maximum value of 50% at 217 m LSF and (2) a 32 m low-porosity interval with a minimum value of 47% at 238 m LSF. A 50% high-porosity peak anomaly at 289 m LSF corresponds with a major fracture zone. From 292 to 311 m LSF, another low-porosity zone (48%) is present. Between 311 and 313 m LSF, a sharp high-porosity anomaly reaches 52% for the bit resistivity, which may correspond to a sand layer (see **"Log characterization and lithologic interpretation"**). Below 316 m LSF, four high resistivity-derived porosity peaks occur at 349, 368, 389, and 394 m LSF.

Bit resistivity–derived porosity anomalies do not clearly coincide with the position of the fractured intervals. High ring resistivity–derived porosity seems to coincide more clearly with such intervals, even if the relation is not systematic.

Estimation of density

Because of the absence of bulk density measurements, we estimated bulk density from the resistivity-derived porosity (Fig. **F20**). Resistivity-derived porosity was converted to density using standard methods (see **"Physical properties"** in the "Expedition 314 methods" chapter).

P-wave velocity

The sonic *P*-wave velocity log in Hole C0004B is of good quality (see **"Data and log quality"**). In this hole, the sonic response appears to reflect well the effects of fracture zones and lithology variation.

Figure **F21** shows the *P*-wave velocity log juxtaposed with logging units and major and minor fracture zones. Below the first 60 m jet-in interval, in which only mud arrivals are detected, the log begins to respond to actual formation velocity, sharply increasing with depth. At the lower portion of logging Subunit IIA, a low-velocity zone forms, attributable to several possible reasons, such as increasing breakout widths and/or decreasing resistivities with depth. It is not clear whether the low-velocity zone is only due to hole condition or a result of low formation velocity. However, it should be noted that no clear variation in gamma ray values, as well as no clear fractures, are associated with this low-velocity zone (Fig. **F1**), which implies that the low velocity might be an artifact caused by increasing breakout width (Fig. **F22**). At the boundary between logging Subunits IIA and IIB, a notable jump in velocity (from 1580 m/s at 92 m LSF to 1826 m/s at 99 m LSF) is detected. It is followed by a gradual increase in velocity, although a minor fracture zone is encountered at the interval 96–112 m LSF. A slight decrease in velocity with depth from 112 to 133 m LSF appears to be related to lithology because subtle changes in gamma ray values and resistivity are also observed at this depth interval. Thereafter, velocity increases steadily throughout logging Subunit IIB.

The upper part of logging Subunit IIC (0–213 m LSF) is characterized by a nearly constant or decreasing velocity. The main control over such velocity behavior seems to be major and minor fracture zones (170–184 and 208–213 m LSF, respectively) and associated borehole breakouts. For the rest of logging Subunit IIC, velocity increases because hole condition was nearly intact.

Logging Subunit IID, including the lowest formations of the thrust sheet and the major fault and fracture zones, exhibits a drastic velocity variation. Velocity decreases almost continually through logging Subunit IID as depth approaches the main fault zone (~290 m LSF). Velocity then increases abruptly across the fault, from 1909 m/s at 291 m LSF to 2115 m/s at 293 m LSF. Immediately below the fault, velocity remains high, averaging ~2120 m/s in a depth

interval between 293 and 311 m LSF. A minor fracture interval from 308 to 324 m LSF appears to cause a velocity decrease in this zone.

Logging Unit III (underthrust sediments) is characterized by a general increase in velocity with depth. However, it is also affected by several velocity lows, which could correspond to either fractures, lithologic variations, or possibly fluid overpressures.

Comparisons between *P*-wave velocity and other physical properties

Comparisons of *P*-wave velocity with resistivity (Fig. F23) and with resistivity-derived porosity (Fig. F24) are made using cross-plots between these properties. Note that resistivity-derived porosity is, in principle, a modified expression of resistivity, although it incorporates the estimated pore fluid temperature as an independent parameter.

Figure F23 shows two cross-plots between *P*-wave velocity and bit and ring resistivity. Individual logging units and subunits show unique velocity-resistivity relations. Logging Unit I and Subunit IIA have positive relations in which both velocity and resistivity increase (albeit at different slopes). The rest of logging Unit II (Subunits IIB, IIC, and IID) show constant increasing velocity with depth, with resistivity remaining at an average of ~1.3 Ωm. Logging Unit III is characterized by a lower resistivity and higher velocity than in logging Unit II, resulting in a reversal in the data trend in the cross-plot. Such behavior is more clearly visible in the cross-plot with bit resistivity.

In the cross-plot between velocity and ring resistivity-derived porosity (Fig. F24), there is a consistent negative relationship between the two properties with increasing slope with increasing velocity.

In all cross-plots shown in Figures F23 and F24, logging Subunit IIA appears to be a transition between the upper slope sediments (Unit I) and the thrust sheet (Subunits IIB, IIC, and IID). Also note that the two clusters of data for logging Subunit IID and Unit III are not clearly differentiated, even though there is a major structural and lithologic change between these groups of data.

Structural geology and geomechanics

Our interpretations of structure and in situ stress are based on resistivity images (see the "Expedition 314 methods" chapter). We used a variety of images of three different depths of investigation and both statically and dynamically normalized images, but final interpretation was primarily based on the shallow dynamic image. The quality of the image data is excellent, permitting clear interpretation of planar features; therefore, our interpretation results should have a high degree of accuracy (see the "Expedition 314 methods" chapter for interpretation errors in subhorizontal planes).

Site C0004 is located at the tip of a deformed thrust sheet above a thrust fault. The site penetrated shallow slope sediments, the deformed thrust sheet, and underthrust slope sediments. The structural characteristics identified in the borehole images define three structural domains (Fig. F25).

Since the lithology of this hole is predominantly homogeneous fine-grained sediments, we sometimes encountered difficulties distinguishing bedding planes and fractures. Most of the fractures are also bedding parallel. Therefore, some conductive planes have been interpreted both as bedding planes and conductive fractures.

Structural domains

Three structural domains were defined based on the pattern of fractures and borehole breakouts and sediment resistivity texture in the images (Fig. F25). Structural Domain 1 (0–95 m LSF) is characterized by a lack of fractures and weak breakouts. The background texture of the sediments in the images shows little variation within this domain. Structural Domain 2 (95–292 m LSF) is characterized by a series of heavily or moderately fractured conductive zones and intensive development of borehole breakouts. Structural Domain 3 (292–396 m LSF) includes a minor fractured zone, but most fractures are patchily developed. Breakouts in Domain 3 continue from Domain 2 but are generally reduced in width. Domain 3 has bedding planes that dip more shallowly than those in Domain 2. See the next section for discussion of the fractured zones.

Bedding

Bedding planes in structural Domain 1 (0–95 m LSF) are consistent and mostly strike east–west and dip 30°–40° to the south (Figs. F25, F26). The beds in structural Domain 2 are more scattered both in dip and azimuth but generally strike northeast–southwest and dip to the north. Beds dip at 20°–70°. Structural Domain 3 shows a less scattered distribution of poles to bedding planes. The dominant bedding plane strike is similar to Domain 2 (northeast–southwest) but the dips are generally gentler (average = ~20°; range = 5°–55°) and to the north.

Natural fractures and fractured zones

Fractures in borehole images have been analyzed according to their azimuth, dip, aperture, and conduc-

tivity and are classified into three types: conductive, resistive, and uncertain fractures (Fig. F27). Most fractures we identified are conductive, but this may be due to the better visibility of conductive sinusoids against the background sediments. The uncertain fractures were defined where breakouts show discontinuity, and these discontinuous features can be picked as a partial sinusoid. Such discontinuity in breakouts may also be caused by variability in lithology; therefore, there is a small possibility that these picked fractures are bedding planes or, alternatively, not real features. Tensile fractures were not observed at this site with the exception of some examples in the uppermost part of the image (56–61 m LSF).

Fractures in structural Domain 2 are mostly conductive but also include some resistive and uncertain fractures (Fig. F27). The fractures are scattered both in strike and dip but with a dominant trend of northeast–southwest and mostly steeply dipping (~30°–70°) to the north (Fig. F27A).

Structural Domain 3 includes fewer fractures than Domain 2. Most are conductive, but Domain 3 also exhibits some resistive and uncertain fractures (Fig. F27). The poles to the fracture planes form a dominant cluster corresponding to planes of northeast–southwest trend and gentler dip (10°–20°) to the north (Fig. F27A). There are also two minor clusters of northwest–southeast striking fractures with both eastward and westward dips.

Eight fractured "zones" in Hole C0004B (Fig. F28) were defined by intense development of fractures (mostly conductive) and wide breakouts and were classified as "major" or "minor" based on their intensity of deformation and conductivity. It is difficult to identify individual fractures and to determine their dip and azimuth within the very conductive parts of these fractured zones. The characteristics of each fractured zone are shown in Figure F28. In structural Domain 2, three major fractured zones and four minor fractured zones are identified (Zones 1–7). Structural Domain 3 includes a minor fractured zone (Zone 8). The uppermost part of fractured Zones 3 and 6 is characterized by merged breakouts of extremely broad width producing uniform high conductivity. The depth ranges of each fractured zone are

- Fractured Zone 1 (minor): 96–112 m LSF,
- Fractured Zone 2 (minor): 133–141 m LSF,
- Fractured Zone 3 (major): 170–184 m LSF (broad breakout conductive zone: 170–175 m LSF) (Fig. F29),
- Fractured Zone 4 (minor): 208–213 m LSF,
- Fractured Zone 5 (minor): 230–235 m LSF,
- Fractured Zone 6 (major): 247–269 m LSF (broad breakout conductive zone: 247–251 m LSF),
- Fractured Zone 7 (major): 284–292 m LSF (Fig. F30), and
- Fractured Zone 8 (minor): 308–324 m LSF.

Borehole breakouts

Breakouts were well developed in structural Domains 2 and 3, and the breakout orientation is approximately the same in these two domains (Figs. F25, F29, F30). Breakout widths range from 10° to >180° but with a modal range of ~50°–80° and an average of 70° (Fig. F31). Structural Domain 1 has patchy narrow breakouts.

Breakout azimuth is generally constant but width varies with depth (Fig. F22). Figure F31 illustrates that the azimuth scatters around a mean of 050° throughout the borehole. The main exception is the azimuth within structural Domain 1, which is ~040°. Breakout width at the borehole wall (Fig. F22) shows a significant increase from ~30° to ~70° at ~100 m LSF at the boundary between structural Domains 1 and 2 and a minor drop at ~290 m LSF at the boundary between structural Domains 2 and 3. These agree with changes in physical properties of the sediments at these boundaries (see **"Physical properties," "Log characterization and lithologic interpretation,"** and discussion in the next section).

The mean azimuth of breakouts is 050° (northeast–southwest) with a range of 020°–080°, indicating that S_{Hmax} is oriented northwest–southeast (~140° or 320°). Our statistical analysis on 1289 breakout measurements throughout the borehole shows that the standard deviation is 15.82 and the 95% confidence interval is <1° of azimuth (Table T6). This orientation of S_{Hmax} is therefore similar to, but statistically distinct from, the orientation at Site C0001 (mean breakout azimuth = 066°; standard deviation = 14°; 95% confidence interval = 0.82°; mean S_{Hmax} orientation = 156° or 336°).

Stress magnitude analysis from breakout widths

Attempts to constrain in situ stress magnitudes were made using empirically estimated rock strengths based on physical properties (see the **"Expedition 314 methods"** chapter). Two depths were chosen for stress magnitude analyses within structural Domains 2 (200 m LSF) and 3 (325 m LSF). Average widths of borehole breakouts at these depths are 75° and 60°, respectively. Figure F32 shows stress polygons for the two depths. Formation pressures are assumed to be hydrostatic. The two stress polygons show that the

unconfined compressive strengths of rocks at respective depths should be >0.9 MPa (200 m LSF) and >1.6 MPa (325 m LSF).

Physical properties that are useful for strength estimation in these clay-rich rock formations are *P*-wave velocity and porosity. Velocities at 200 and 325 m LSF were ~1890 and ~1990 m/s, respectively; only a 5% difference. Since no measurement of porosity was conducted in this hole, indirect porosities (derived from resistivity) were used (see **"Physical properties"**). Estimated porosities at the two depths are ~49.5% and ~50%, respectively; therefore, the rocks at the two given depths appear to possess very similar physical properties, which in turn suggest similar strengths.

A series of empirical relations between physical properties and strengths give a strength range between 1.0 and 5.8 MPa, with an average of 4.1 ± 2.0 MPa. Because of a relatively large uncertainty in rock strength and the relatively small size of polygons, it is not clear which stress regime should fit the state of stress. If only average values of strengths are used, the stress states at both depths will be either in the strike-slip or thrust fault stress regime. For a given strength value, the stress state at 200 m LSF lies in a region more favorable for strike-slip or thrust fault regimes than that at 325 m LSF.

Discussion and conclusions

Correlation of structural domains and logging units

The characteristics of the structural domains correspond to physical properties of the sediments as well as structural character and can therefore be generally correlated with the logging units. Structural Domain 1 (0–95 m LSF) includes logging Unit I and Subunit IIA; we see no structural evidence for division at the Unit I/IIA boundary. The minimal change in structural character in the resistivity images between these logging units suggests small changes in physical properties (and therefore rock mechanics parameters) within structural Domain 1. This is supported by the characteristics of the sonic log, which shows that both logging Unit I and Subunit IIA have extremely slow *P*-wave velocities (see **"Log characterization and lithologic interpretation"**). The structural features and log characteristics of structural Domain 1 could be interpreted as two sedimentation stages of slope deposits; the upper slope sediments correspond to Unit I and the lower slope sediments correspond to Subunit IIA. The strong reflectivity at the Unit I/Subunit IIA boundary suggests that the reflection coefficient is larger than at the boundary between Subunits IIA and IIB. Subunit IIA may therefore be composed of reworked or slumped sediments, mostly from the deformed thrust sheet.

The boundary between structural Domains 2 and 3 at 292 m LSF lies within logging Subunit IID, a proposed transition zone between the thrust sheet deposits and overridden sediments (see **"Log characterization and lithologic interpretation"**). Deformation characteristics from resistivity images at the boundary of structural Domains 2 and 3 suggest a thin (a few meters) transition zone (Fig. **F30**) between the thrust sheet and underthrust section around fractured Zone 7 (284–292 m LSF), contrasting with the relatively thick logging Subunit IID (236.4–323.8 m LSF).

Structural comparisons between borehole and seismic reflection data

The structural features identified in the borehole resistivity images are well correlated with the structural style in the seismic reflection profiles. Bedding planes in structural Domain 1 dip to the south, consistent with the reflection horizons. The scattered seismic pattern in the thrust sheet can be explained by steeply dipping beds in Domain 2. The beds in Domain 3 dip gently north and agree with the structural style of the underthrust section in the seismic profile, although the borehole beds tend to show higher dips.

The fractured zones also match the seismic profile well (Fig. **F33**). The major fractured Zone 3 (170–184 m LSF) is exactly at the crosscutting point of a possible landward-dipping thrust fault at this site. The major fractured Zones 6 (247–269 m LSF) and 7 (284–292 m LSF) match with distinct positive reflection surfaces both inclined to the north. The boundary between the thrust sheet and underthrust sediments is at fractured Zone 7 and correlates with a major increase in velocity (impedance).

Breakouts and convergence directions

The breakout directions show mean S_{Hmax} shortening at 320° (Figs. **F22, F31**), which is between the mean S_{Hmax} direction at Site C0001 (336°) and the convergence direction (300°–315°) of the Philippine Sea plate and southwest Japan (Miyazaki and Heki, 2001; Seno et al., 1993; Heki, 2007). The difference between the plate convergence direction and the S_{Hmax} direction at Site C0004 may be due to partitioning of oblique shortening within the forearc. The 16° difference in the S_{Hmax} direction between Sites C0001 and C0004 may be caused by minor strike-slip faulting (partitioning of strain) or seafloor topography. Such a topographic effect on the local stress field is observed at the northern margin of the Kumano forearc

basin (Yamamoto, 2006) and also in numerical models of accretionary prisms (Yamada et al., 2006). However, Site C0004 is located where the seafloor slopes gently toward the trench; therefore, topographic effects should be minimal.

Log-seismic correlation

Overall logging unit correlation

Logging Unit I/II boundary and the base of slope sediments

The base of the slope sediment section corresponds to the logging Unit I/II boundary (Figs. **F34, F35;** Table **T7**). Sonic velocity increases at the boundary from little more than drilling fluid velocity to ~1600 m/s (Fig. **F36**). Gamma ray and resistivity logs similarly increase (Figs. **F37, F38**). The change in gamma ray value suggests that Unit II is somewhat more clay rich than Unit I. The caliper log shows that hole size drops to nearly in-gauge at the boundary and continues nearly in-gauge in the uppermost ~20 m of Unit II (Fig. **F39**). The transition in each of the logs is gradual rather than abrupt. These gradual changes likely account for the relatively low frequency character of the reflection at the base of the slope sediments.

Logging Subunit IID: fault zone between thrust sheet and underthrust sediments

Logging Subunit IID corresponds to a thick zone of roughly parallel, northwest-dipping reflections caused by a system of faults along which older accreted rocks have been thrust over slope deposits (Figs. **F34, F40;** Table **T7**). In Hole C0004B the zone of parallel reflections form a peak, wide-trough, peak pattern from ~252 to 323 m SSF. However, the seismic reflections on both the inline and cross-line (Fig. **F2**) adjacent to the hole show considerable 3-D variation in this pattern on a scale of 50–100 m. Therefore, it is not reasonable to expect an exact correlation between log values in a single hole and the seismic data, which smear the image laterally on a scale of 20–40 m.

The velocity in the upper half of the dipping reflection package decreases from ~1900 to ~1800 m/s over the range from 243 to 291 m LSF (Fig. **F40**). This corresponds to the upper peak and about half of the broad low-amplitude trough. The sonic log begins a significant increase in interval velocity, from ~1900 to 2100 m/s, at 291 m LSF. Velocity remains high to ~313 m LSF before decreasing to ~2000 m/s. This high velocity corresponds to the base of the broad trough and top of the basal peak of the dipping reflection section. A thin layer with dramatically lower velocity at ~306 m LSF is within the basal bright peak of the dipping sequence. The nearly flat horizons below have velocities varying between 2000 and 2100 m/s and form a series of bright peaks and troughs.

Check shot survey data

Check shot data were acquired at 23 depths in Hole C0004B. Because of excessive noise levels, two of the stations were not useable, but the remaining 21 stations yielded excellent quality waveforms (Fig. **F41;** Table **T7**). These data sample depths from the seafloor to 376 m LSF. Approximately 15 air gun array shots were fired at each station during the LWD drilling and 8 shots were fired at each station during the pipe trip out of the hole. Noisy traces and traces with poor first arrival waveforms were deleted. The remaining traces were filtered (trapezoidal, minimum phase, and 30-40-150-200 Hz band-pass) and stacked to produce the traces shown in Figure **F41.** The first arrival wavelet is unambiguous on all traces.

The first arrival time was picked manually. These are the "raw first arrival" times in Table **T8.** We applied a damped least-squares inversion to the observed depth-time data (Lizarralde and Swift, 1999). This inversion determines a smooth velocity depth curve by varying the arrival times by amounts that are within their uncertainty. We estimated the uncertainty of the arrivals to be ~0.3 ms. We used an inversion damping coefficient of 0.5 because it produced a χ^2 value consistent with the optimal balance between over- and underfitting the data. The smoothed interval velocities and adjusted arrival times are shown in Table **T8.** The improvement in estimated interval velocities, indicated by the smoothness of the curve and the general downward increase of velocity (Fig. **F42**), is dramatic. The accompanying changes in arrival times are very small. We used the smoothed arrival picks and the tool depths as the check shot curve, which we then used for synthetic seismogram preparation.

Beyond the general increase of interval velocity from 1500 m/s at the seafloor to 2100 m/s at 400 m LSF, there is not an exact match between the check shot velocity curve and the sonic log values (Fig. **F42**). Between the seafloor and ~60 m LSF, the sonic velocity is low. This is the region where it was not possible to distinguish the sonic arrival through the drilling fluid (mud arrival) and the formation. Below 60 m LSF, the sonic velocity merges with the check shot velocity. From ~100 to 250 m LSF, the check shot velocity matches the lower envelope of the sonic velocities. The difference between the trend of the sonic velocity and the check shot velocity is ~600 m/s. The check shot curve fails to resolve the zones of low ve-

locity above, and high velocity below, ~290 m LSF. This is partly due to sparse sampling, with data points spaced at an average of 39 m. It is probably also affected by the smoothing applied to the check shot velocities. This technique treats interval velocity variations from station to station as noise and smoothes them out. Whereas this method is necessary to get rid of real noise, it may need to be applied differently to avoid misinterpreting abrupt geological velocity variation with depth.

We were not able to construct a meaningful vertical seismic profile using these data. We tried a number of filtering and gain combinations but could not identify coherent upward-traveling reflections. We attribute this to noise from the banging of the drill pipe in the current and other sources of downhole noise.

Synthetic seismogram

In order to construct a synthetic seismogram for Site C0004, we used the high-quality DTCO log, but because of the absence of an azimuthal density neutron log, we used a pseudodensity log calculated from resistivity (see **"Physical properties"**). The resulting synthetic seismogram correlates well with the seismic reflection data at several depths, but there are also several discrepancies.

Good to excellent correlations were made for the following regions:

1. The base of the slope sediments (logging Unit I/II boundary),
2. Some individual reflections within the thrust sheet (hanging wall),
3. The top of the main fault zone (logging Subunit IIC/IID boundary), and
4. Nearly every reflection within the footwall underthrust sediments (Fig. **F43**).

Two locations that match poorly include a zone from 93 to 99 m LSF, which exhibits low then high sonic velocity values and produces an antisymmetric high-amplitude reflection, and a zone from 236 to 248 m LSF, which is a high and then low zone of sonic velocity values that results in an anomalous negative polarity reflection.

The reflection at the base of the slope sediments in the synthetic seismogram is a positive polarity reflection with a complicated base in the form of a double positive peak. This reflection in the seismic data locally is also a positive polarity reflection with a complicated base, but usually the base is in the form of a small negative peak.

The synthetic seismogram matches the top of the main fault zone well but has a strong long-wavelength positive polarity reflection within the zone that obscures any reflection at the base of the zone.

No reflection seems to correspond exactly to the gradual but significant increase in sonic log velocity within the fault zone at 291 m LSF.

Discussion and synthesis

The primary goals of drilling and logging at Site C0004 were, in order of priority, the characterization of

1. The major splay fault,
2. The overlying thrust sheet,
3. The underthrust sediments originally deposited in a now-overridden slope basin setting, and
4. The young slope deposits in the uppermost unit.

Log data are consistent with the various units being clastic sediments ranging from hemipelagic to turbiditic origin. The logging units divide the drilled formations into young slope deposits, with logging Unit I representing well-stratified deposits (and logging Subunit IIA being likely slump deposits incorporated into the thrust wedge), the thrust sheet represented by logging Unit II, and the underthrust section, also stratified clastic deposits, marked by logging Unit III. Physical properties and structural interpretations support division into three structural domains that overlap but are distinct from the logging units. Logging Unit I and Subunit IIA lack distinct fractures or well-developed breakouts and are assigned to a structural domain (1) that has seen little or no apparent tectonic deformation. Structural Domain 2 is the thrust sheet, exhibiting numerous zones of fracturing and intense breakouts. The interpretation of logging Subunits IIB–IID as finer grained hemipelagic sediments is consistent with the structural interpretation of a distinct domain if it is an uplifted thrust package, perhaps of older Shikoku Basin sediments. Within structural Domain 2, a number of intervals of concentrated fractures likely correlate with subsidiary thrust faults within the thrust sheet (Fig. **F33**).

The interval between the two major conductive fractured zones at 247–269 m LSF and 284–292 m LSF (see **"Structural geology and geomechanics"**) may represent either a zone of anastomosing thrusts forming a ~50 m thick broad fault zone or a sliver of relatively intact sedimentary strata bounded by two distinct thrusts. Discriminating between these alternatives will require analysis of Expedition 316 cores.

One perhaps surprising discovery is that the section immediately underthust beneath the splay fault below 292 m LSF is a zone of higher *P*-wave velocity

and resistivity, when the opposite might be expected, based on the assumption that older, more deeply buried and denser rocks were thrust over younger slope sediments. It is possible that intense fracture development through tectonic deformation of the ~50 m thick thrust zone has lowered its resistivity and velocity locally. The resistivity below the fault zone is only elevated for ~20–30 m, then declines to values lower than those above 247 m LSF. This may represent the actual contrast between the bulk properties of the thrust sheet and underthrust section, unaltered by local fracturing. Again, core analysis may shed light on this log observation.

The observation that breakouts are well developed in both the thrust sheet (structural Domain 2) and the underthrust section (structural Domain 3) suggests that this fault is not a locus of a strong stress decoupling; that is, both domains are still subject to the overall present-day tectonic stress. The breakout orientation is similar in general to that at Site C0001 but differs by ~16° in a statistically significant way. This deviation is likely a product of relatively small 3-D variations of the stress field caused by local structural variability, perhaps as a result of surface slope and gravitational stresses.

References

Heki, K., 2007. Secular, transient and seasonal crustal movements in Japan from a dense GPS array: implication for plate dynamics in convergent boundaries. *In* Dixon, T., and Moore, C. (Eds.), *The Seismogenic Zone of Subduction Thrust Faults:* New York (Columbia Univ. Press), 512–539.

Kinoshita, M., Goto, S., Hamamoto, H., and Yamano, M., 2003. Heat flow distribution and thermal regime across the Nankai accretionary complex. *Eos, Trans. Am. Geophys. Union,* 84(46)(Suppl.):T42C-06. (Abstract)

Lizarralde, D., and Swift, S., 1999. Smooth inversion of VSP traveltime data. *Geophysics,* 64(3):659–661. **doi:10.1190/1.1444574**

Miyazaki, S., and Heki, K., 2001. Crustal velocity field of southwest Japan: subduction and arc-arc collision. *J. Geophys. Res.,* 106(B3):4305–4326. **doi:10.1029/2000JB900312**

Moore, G.F., Bangs, N.L., Taira, A., Kuramoto, S., Pangborn, E., and Tobin, H.J., 2007. Three-dimensional splay fault geometry and implications for tsunami generation. *Science,* 318(5853):1128–1131. **doi:10.1126/science.1147195**

Seno, T., Stein, S., and Gripp, A.E., 1993. A model for the motion of the Philippine Sea plate consistent with NUVEL-1 and geological data. *J. Geophys. Res.,* 98(B10):17941–17948. **doi:10.1029/93JB00782**

Yamada, Y., Baba, K., and Matsuoka, T., 2006. Analogue and numerical modelling of accretionary prisms with a décollement in sediments. *In* Buiter, S.J.H., and Schreurs, G. (Eds.), *Analogue and Numerical Modelling of Crustal-Scale Processes*. Geol. Soc. Spec. Publ., 253:169–183.

Yamamoto, K., 2006. Stress evaluation of shallow formation in Nankai Trough area by the data of METI Exploratory Test Wells Tokai-oki to Kumano-nada [Japan Geoscience Union Meeting 2006, Chiba, Japan, 14–18 May 2006].

Publication: 11 March 2009
MS 314315316-116

Figure F1. Summary log diagram, Site C0004. LSF = LWD depth below seafloor, VE = vertical exaggeration. Black tadpoles = bedding, red tadpoles = fracture, tadpole line = dip direction of plane.

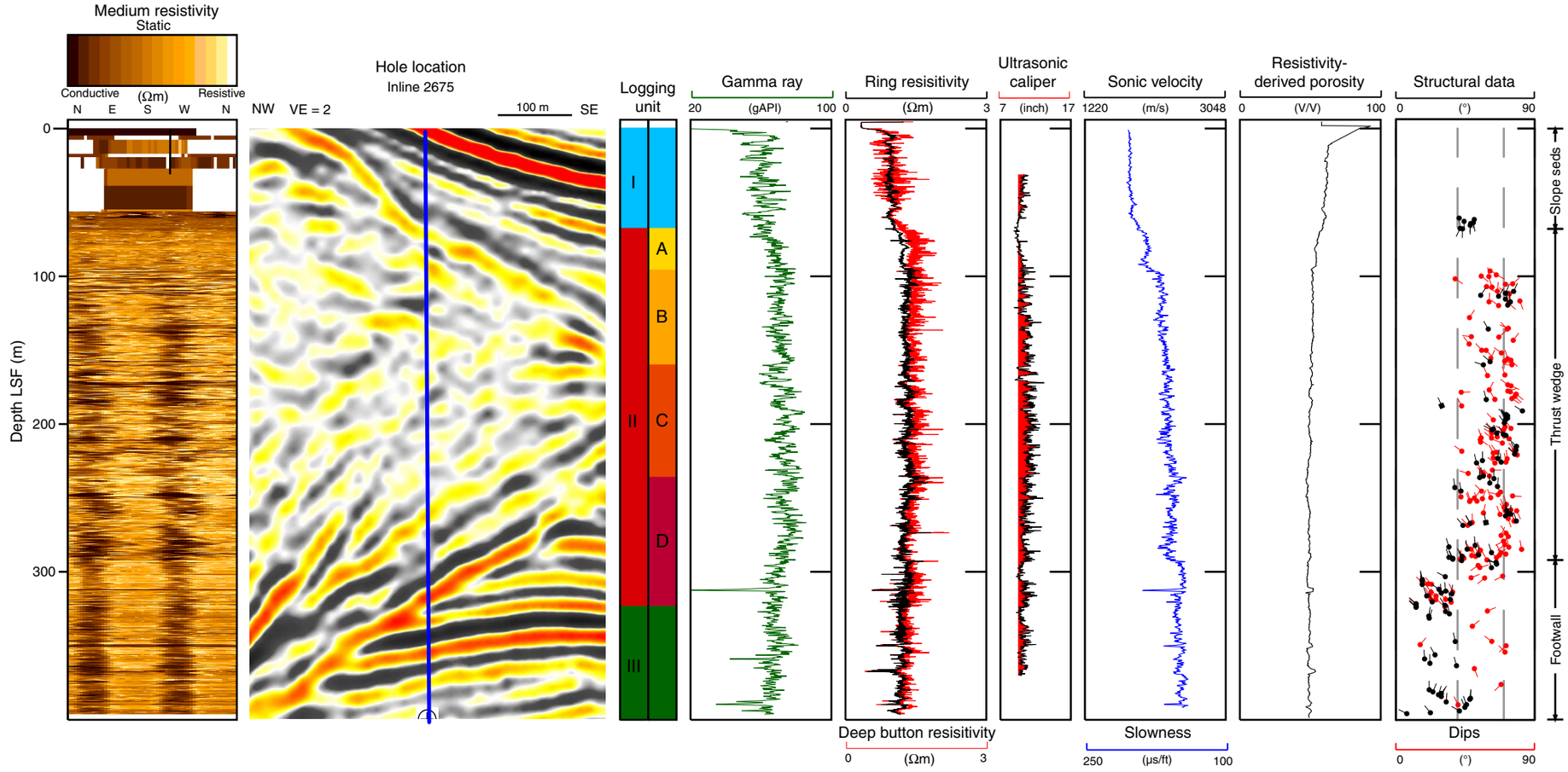

Figure F2. Three-dimensional seismic profile crossing Site C0004 (Moore et al., 2007). Location of the profile is plotted in Figure F3. **A.** Inline 2675. **B.** Cross-line 5295. VE = vertical exaggeration.

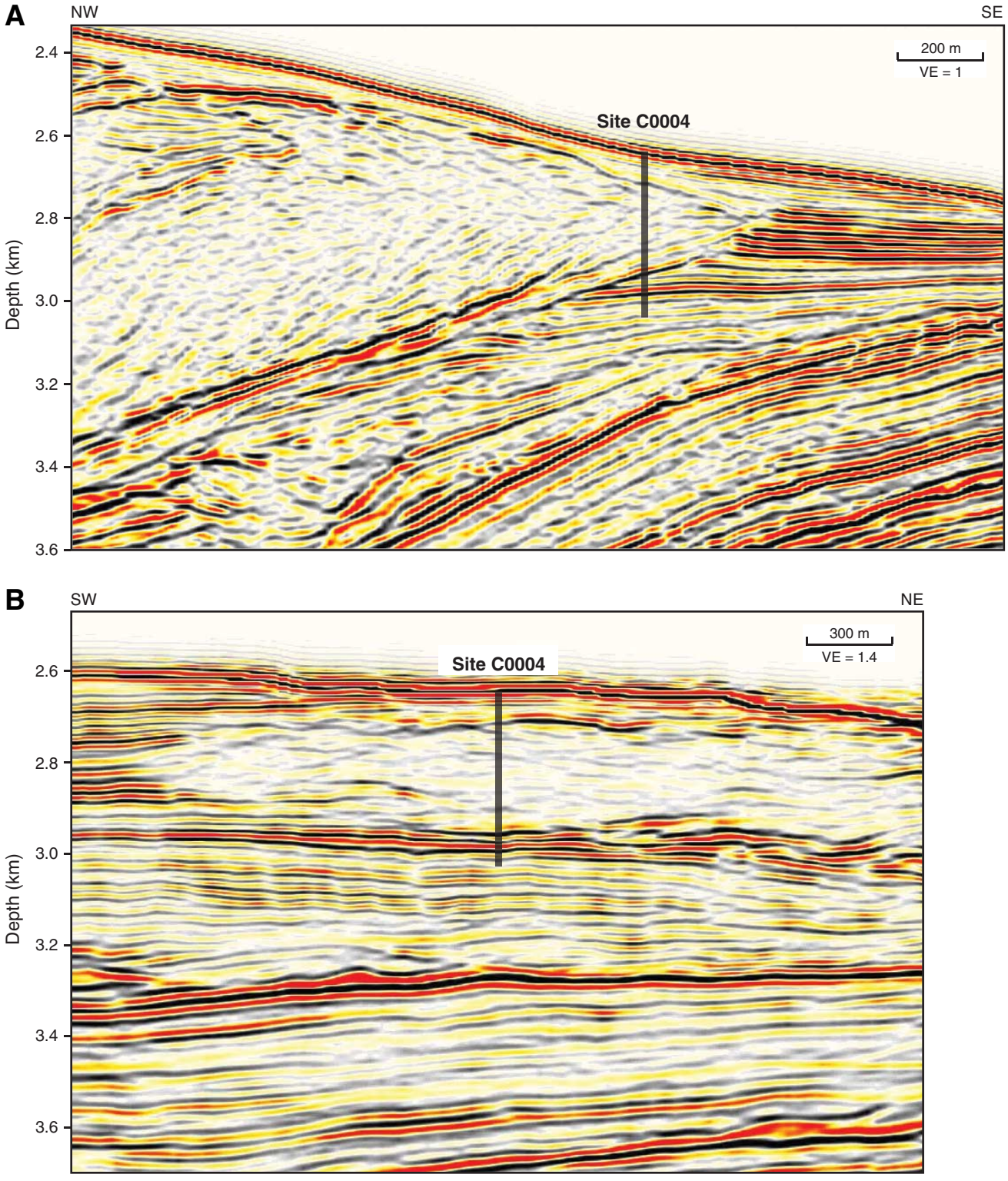

Figure F3. Hole locations, Site C0004. Solid lines = three-dimensional seismic line tracks.

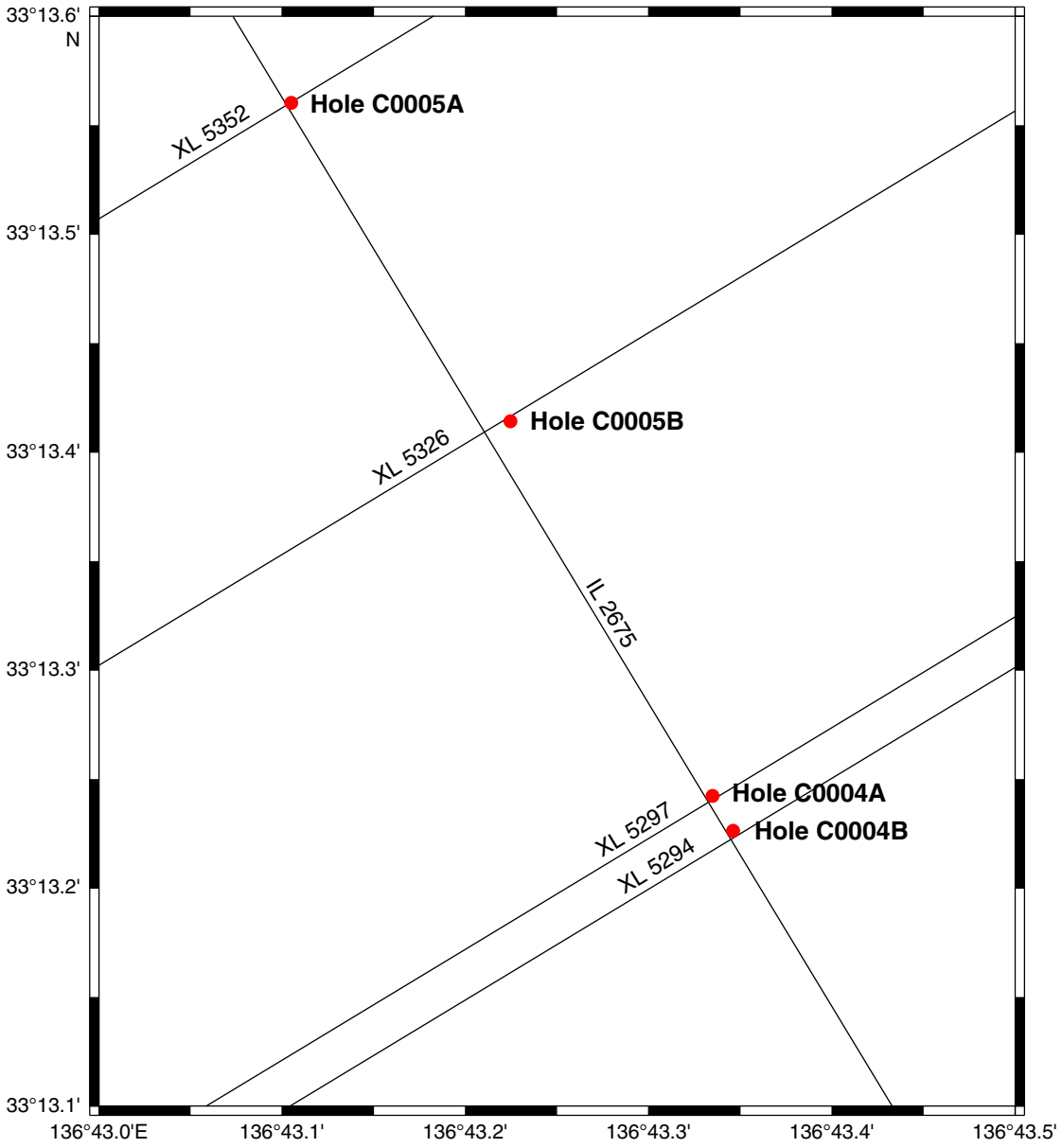

Figure F4. Drilling parameters and gamma ray log plotted vs. time for MWD-APWD operations in Hole C0004B. GR_RAB_RT = gamma ray resistivity at bit (real time), ECD = equivalent circulating density, APRS = average annular pressure, TRPM = MWD turbine rotation speed, TRPM_RT = TRPM (real time), CRPM = collar rotation, SWOB = surface weight on bit, HKLD = hook load, SPPA = standpipe pressure, ROP = rate of penetration, ROP_5ft = 5 feet averaged ROP, LSF = LWD depth below seafloor, DRF = drillers depth below rig floor.

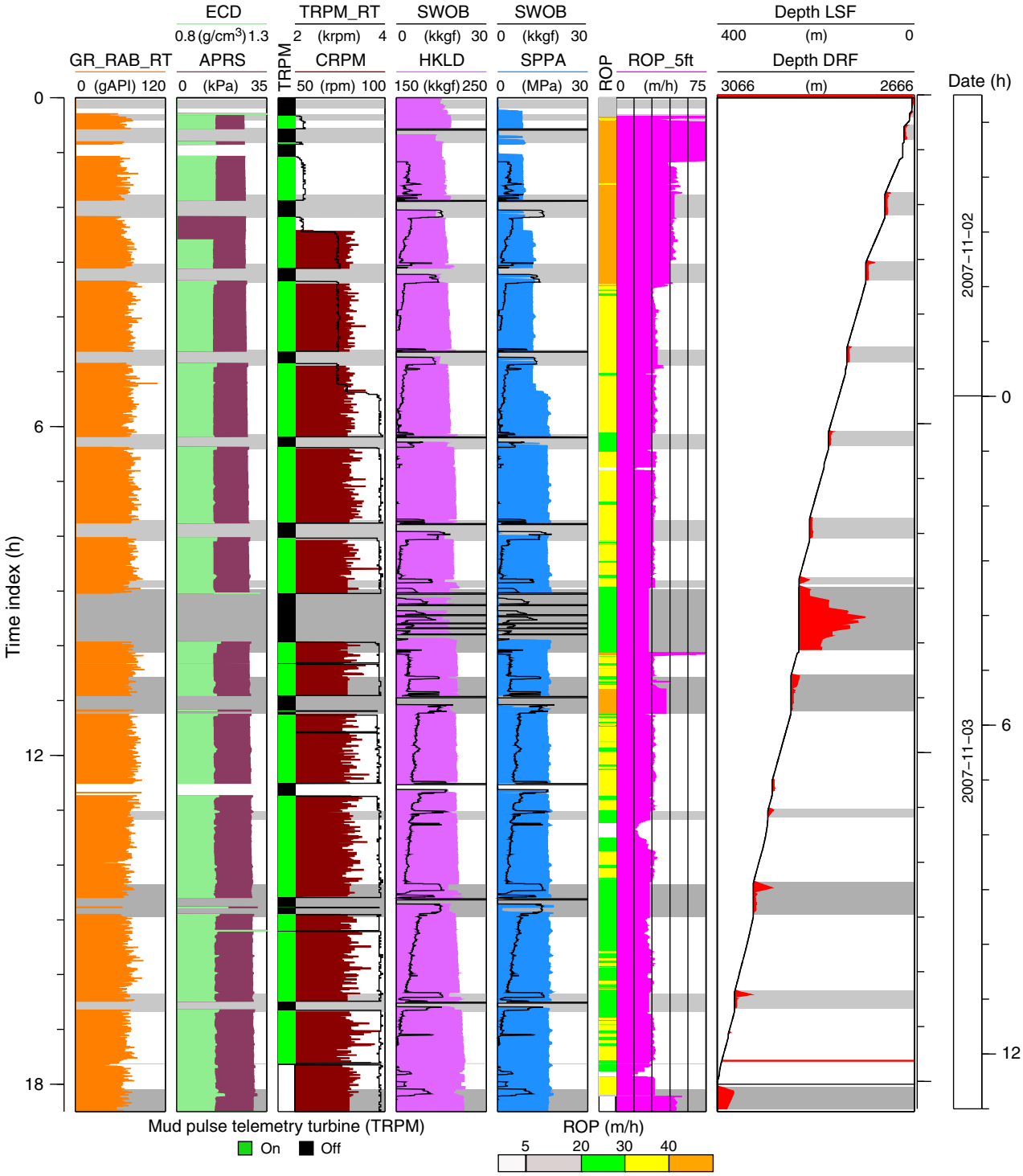

Figure F5. Mudline (seafloor) identification in Hole C0004B using gamma ray and resistivity logs from the geoVISION resistivity tool (memory data). The seafloor is defined by a break in the gamma ray and resistivity logs at 2666 m drillers depth below rig floor (DRF). Resistivity data are plotted on a linear scale. LSF = LWD depth below seafloor.

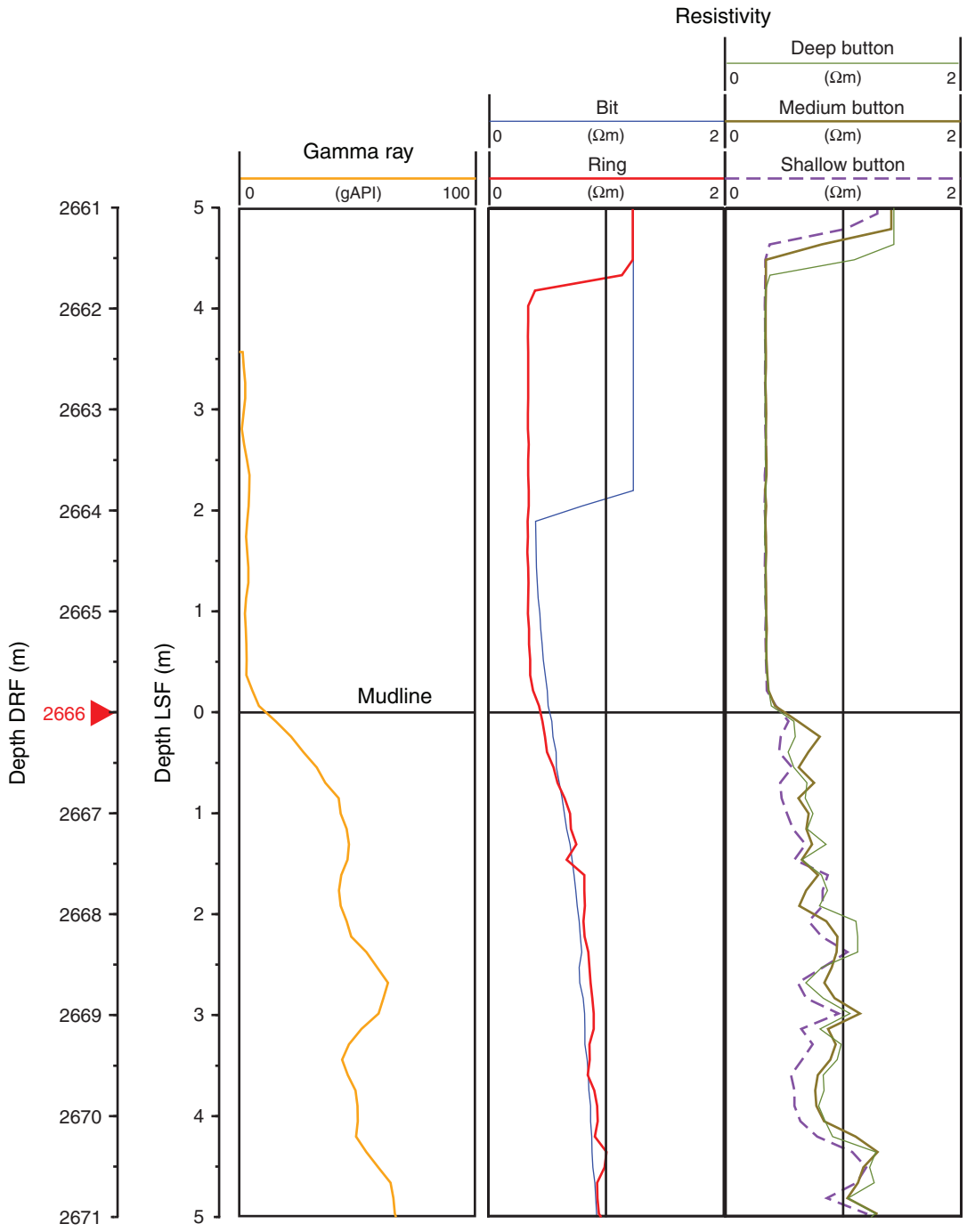

Figure F6. Control logs in Hole C0004B. LSF = LWD depth below seafloor; ROP = rate of penetration; SWOB = surface weight on bit; HKLD = hook load; SPPA = standpipe pressure; ECD = equivalent circulating density; APRS = average annular pressure; CC15, CC26, CC37, and CC48 = Azimuthal Density Neutron (ADN) tool ultrasonic calipers; GR_RAB = gamma ray (geoVISION tool).

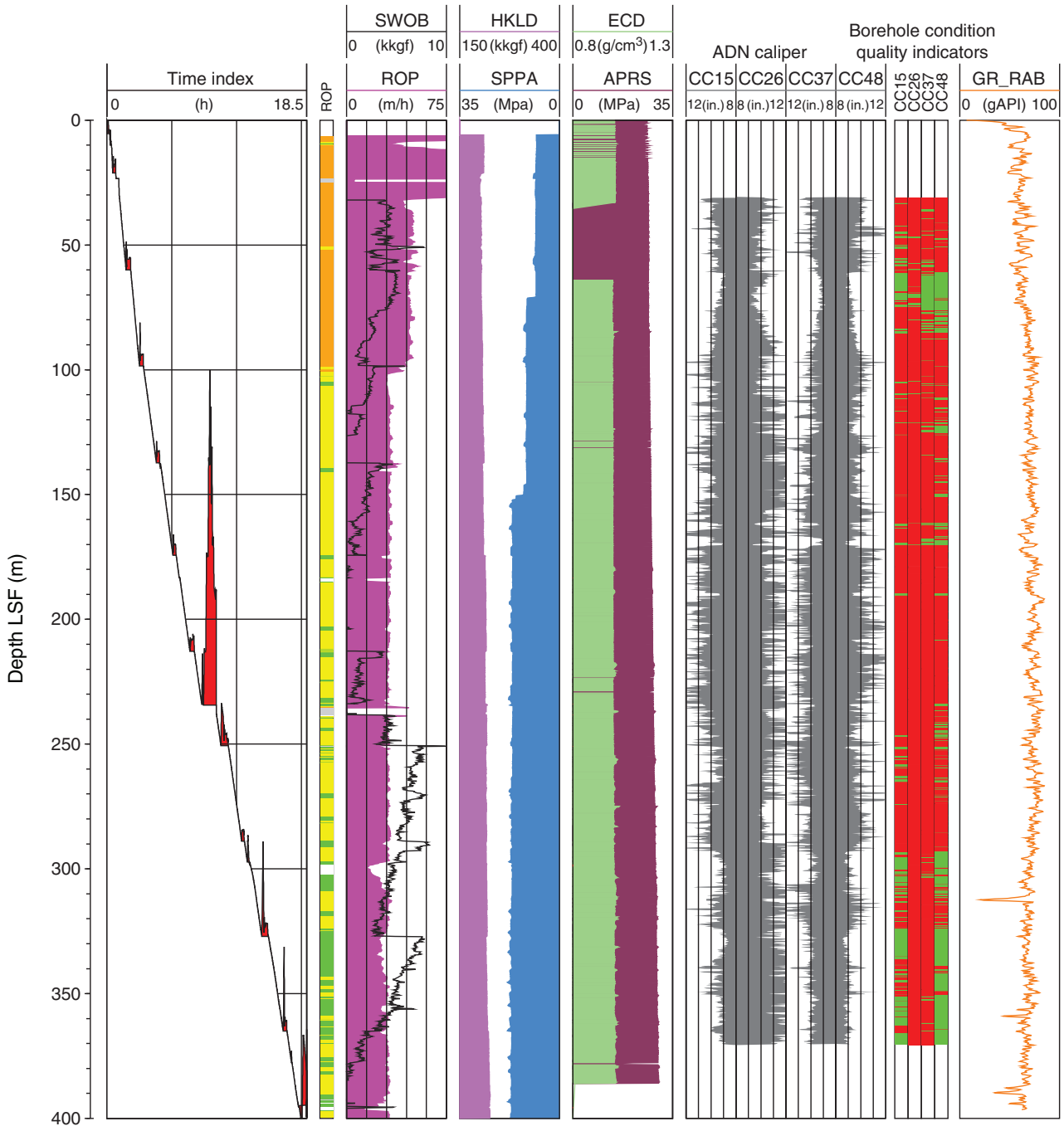

Figure F7. Geophysical logs in Hole C0004B. LSF = LWD depth below seafloor, ROP = rate of penetration, TAB_DEN = time after bit (TAB) of ADN density measurement, GR_RAB = gamma ray log (geoVISION resistivity [GVR] memory data), TAB_RAB_GR = TAB of gamma ray measurement by the GVR tool, color coded borehole condition indicators based on ADN ultrasonic calipers (Cxy = CC15, CC26, CC37, and CC48), TAB_RAB_BD = TAB of GVR deep button resistivity, TAB_RAB_BIT = TAB of GVR bit resistivity, V_P = sonic compressional velocity

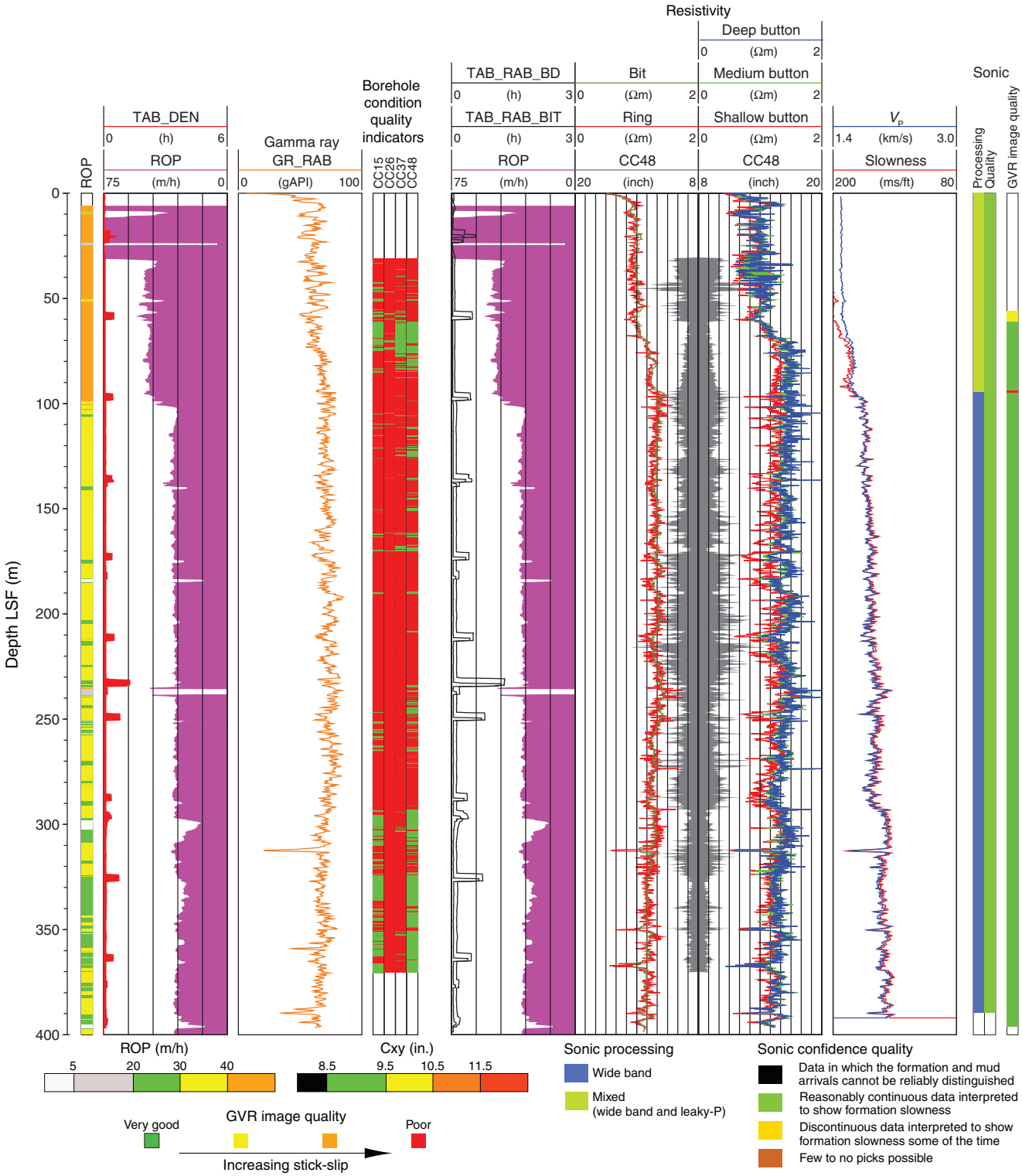

Figure F8. Plot of time-depth relationship in Hole C0004B.

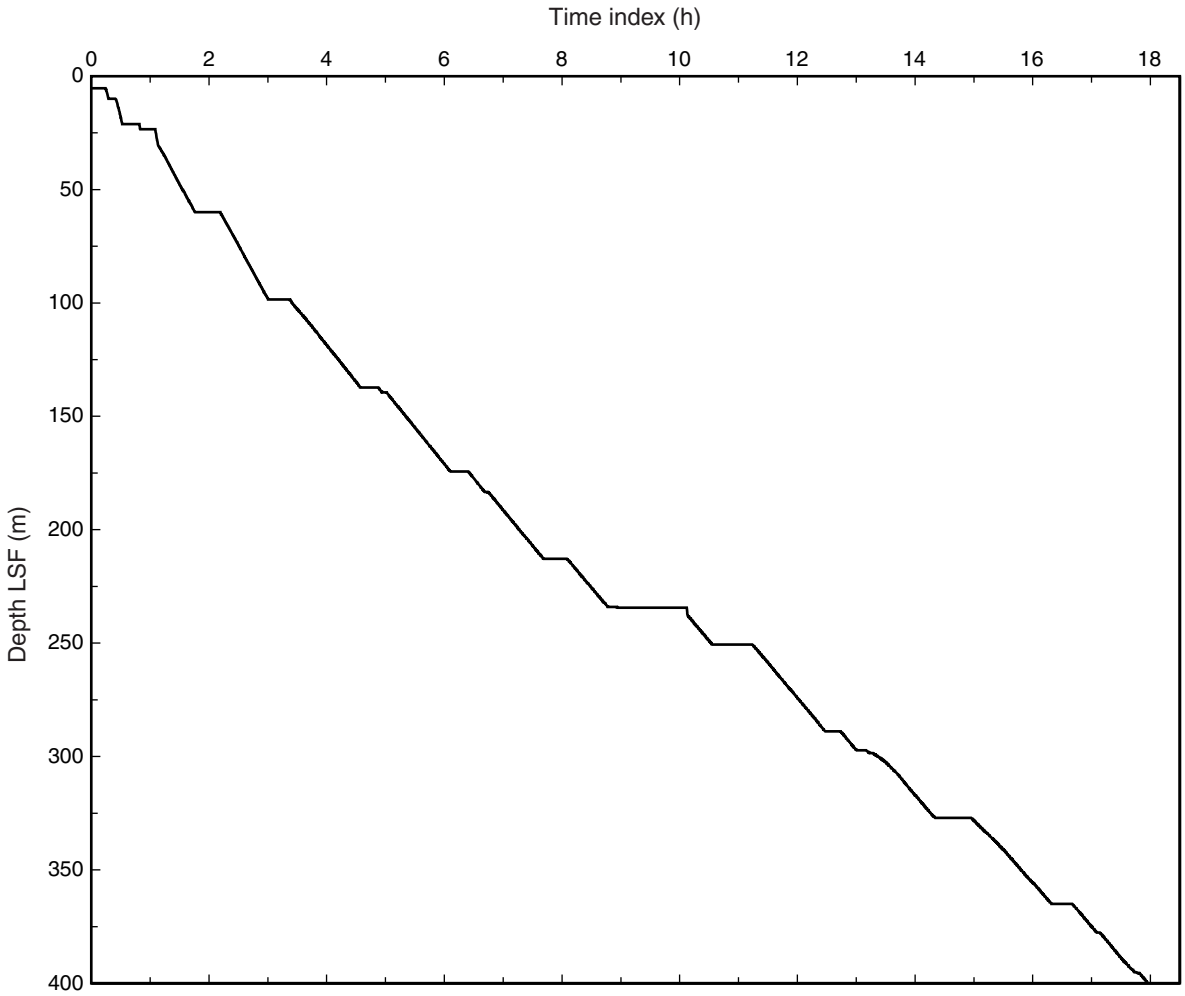

Figure F9. Average caliper (CCAV) and resistivity logs and curve of the difference between deep and shallow button resistivity data. Smoothing results from moving average of resistivity values using a 21-point window. Red zone in caliper log = caliper values higher than 9.5 inches. Light gray bands = minor fracture zones, dark gray bands = major fracture zones (see Fig. F28).

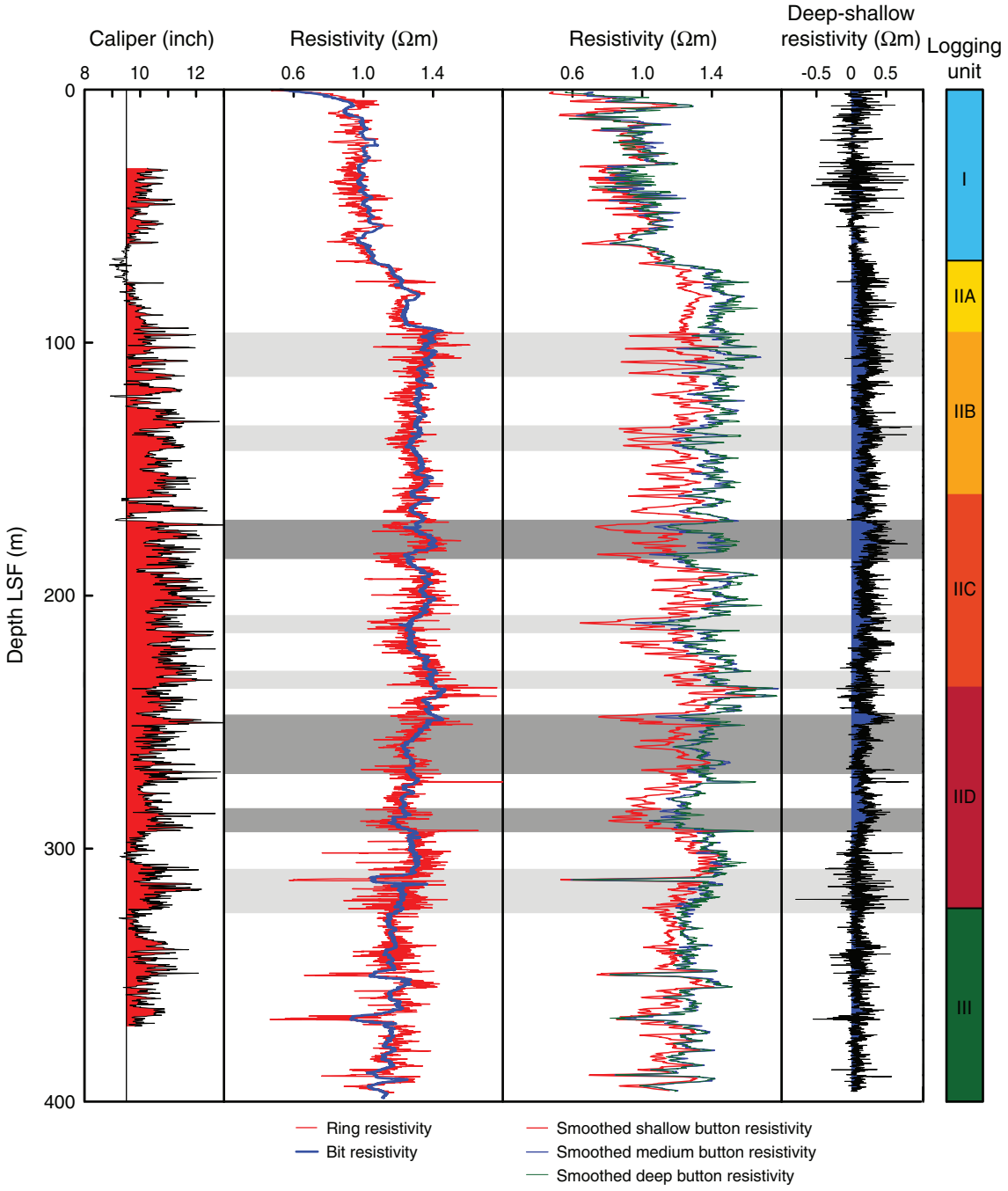

Figure F10. Ring and deep resistivity, gamma ray, and sonic transit time (slowness) distributions for the logging units and subunits.

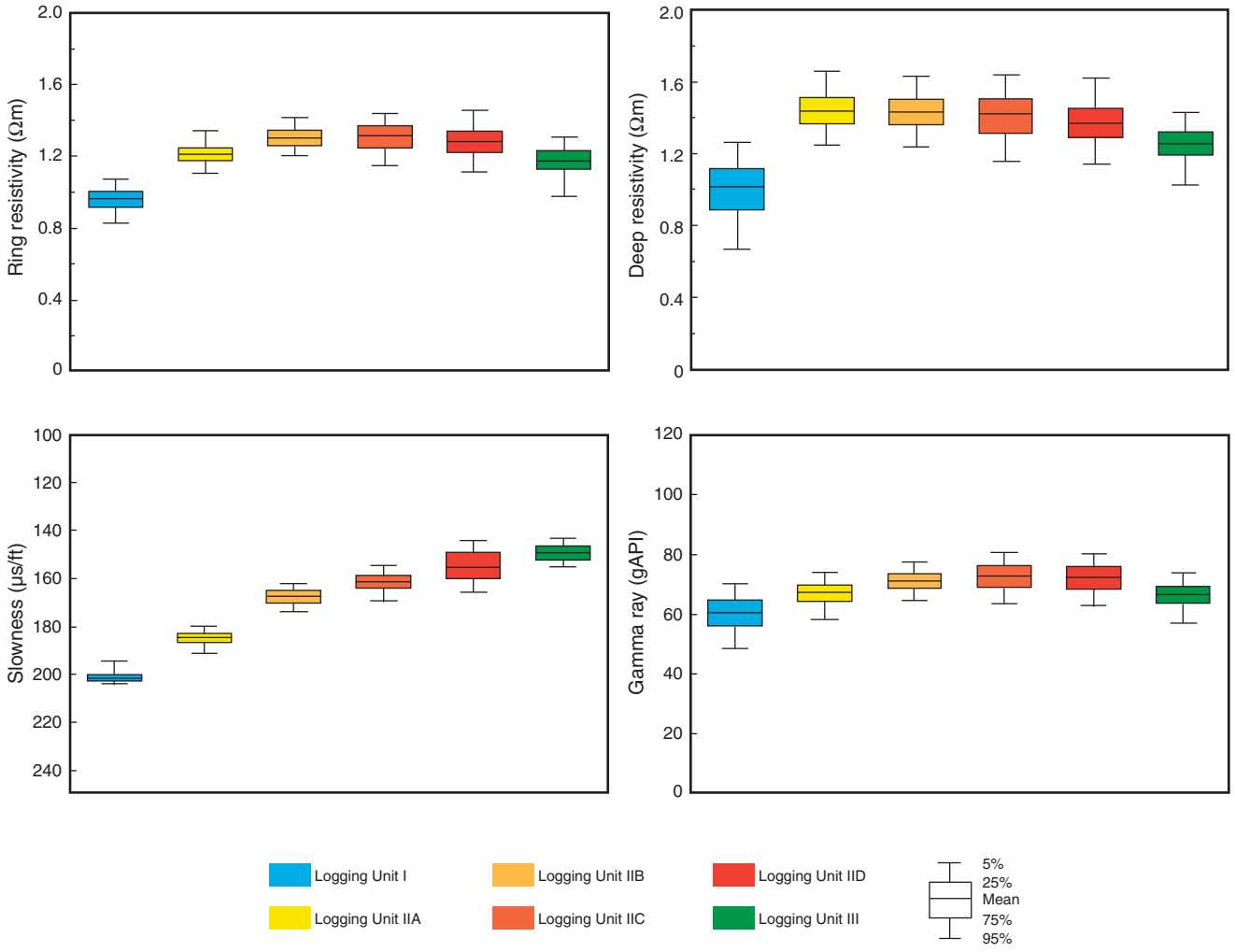

Figure F11. Plots of sonic transit time (slowness) vs. (**A**) gamma ray and (**B**) ring resistivity.

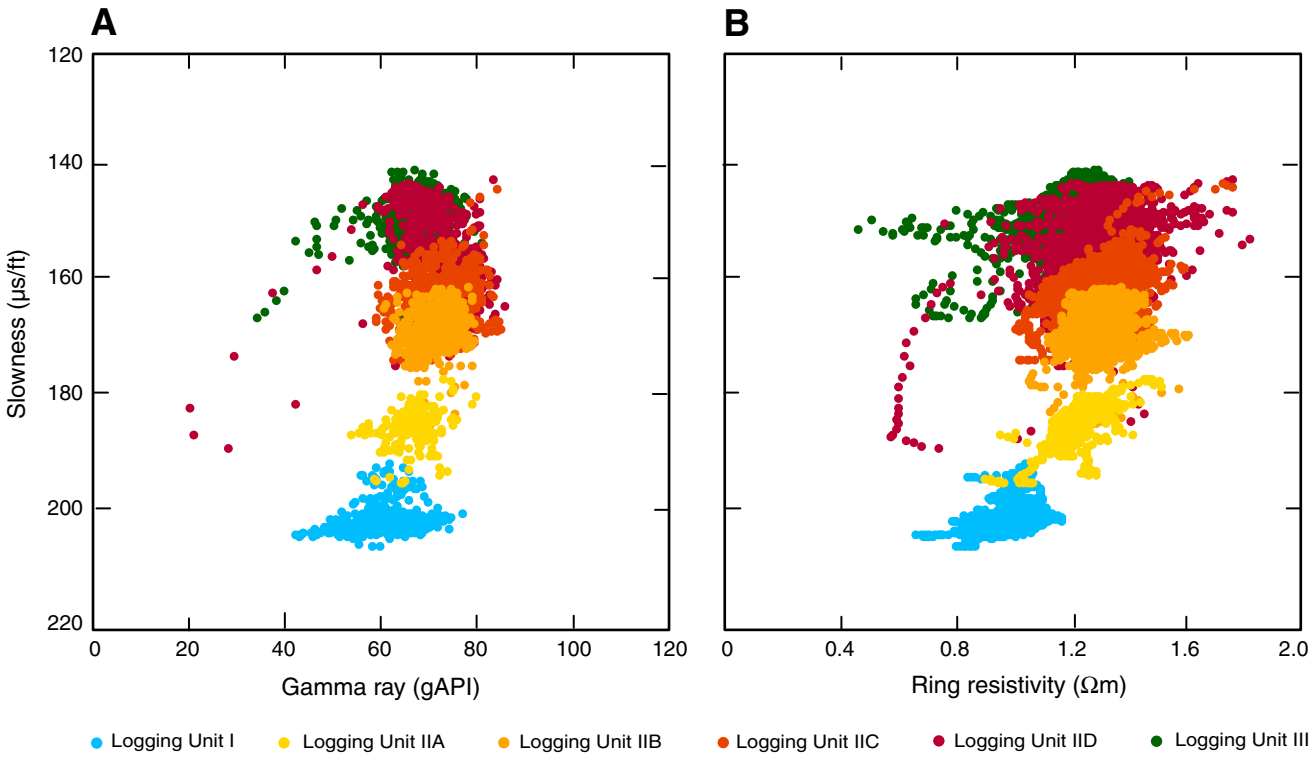

Figure F12. Summary plot of bedding dips derived from image data. Circled tadpole groups described in text. Rose diagrams = dominant bedding dip direction. LSF = LWD depth below seafloor, RAB = resistivity-at-the-bit, GR = gamma ray.

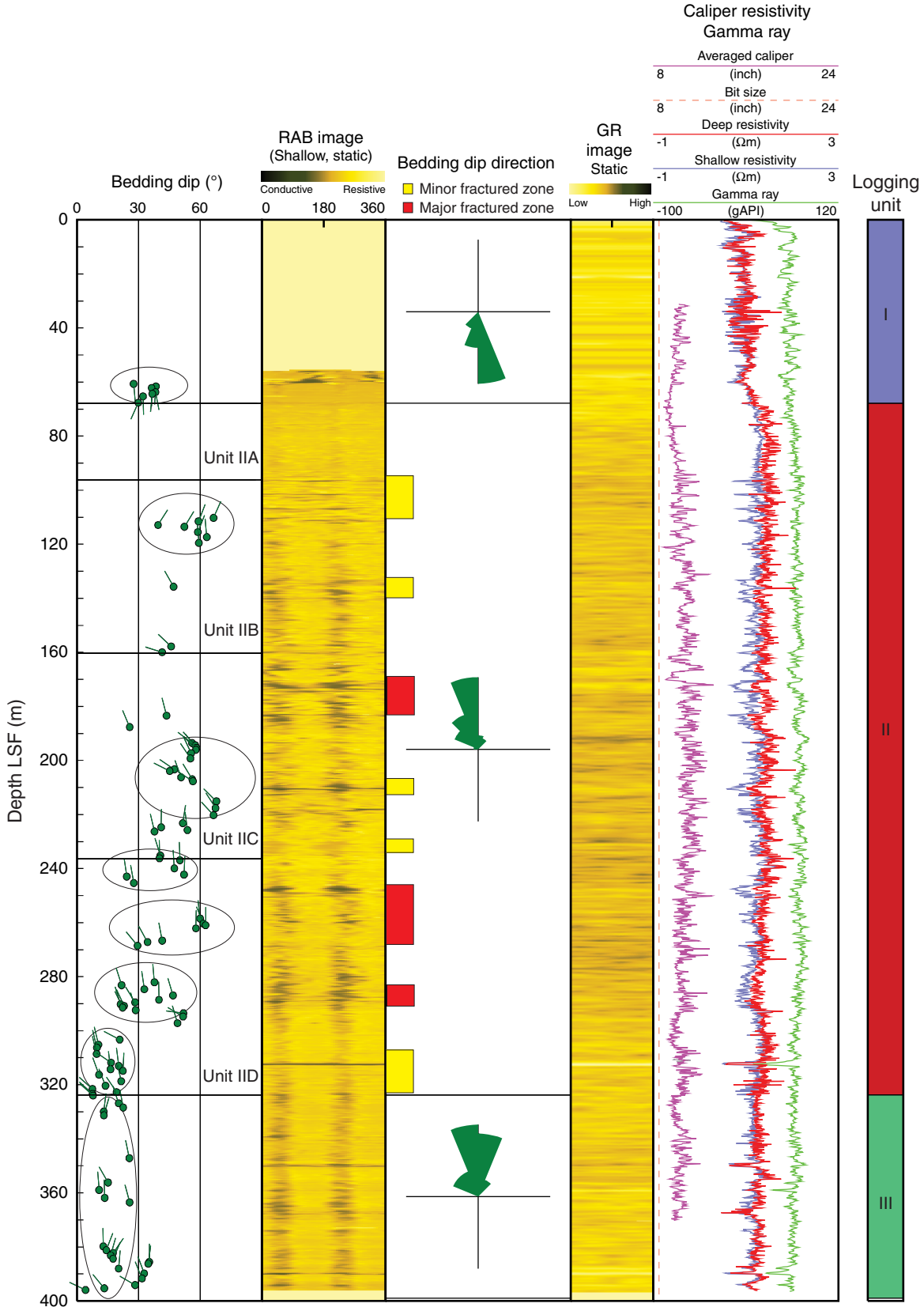

Figure F13. Detailed section of logging Unit I showing the dominant gamma ray trends at logging Units I and II. LSF = LWD depth below seafloor.

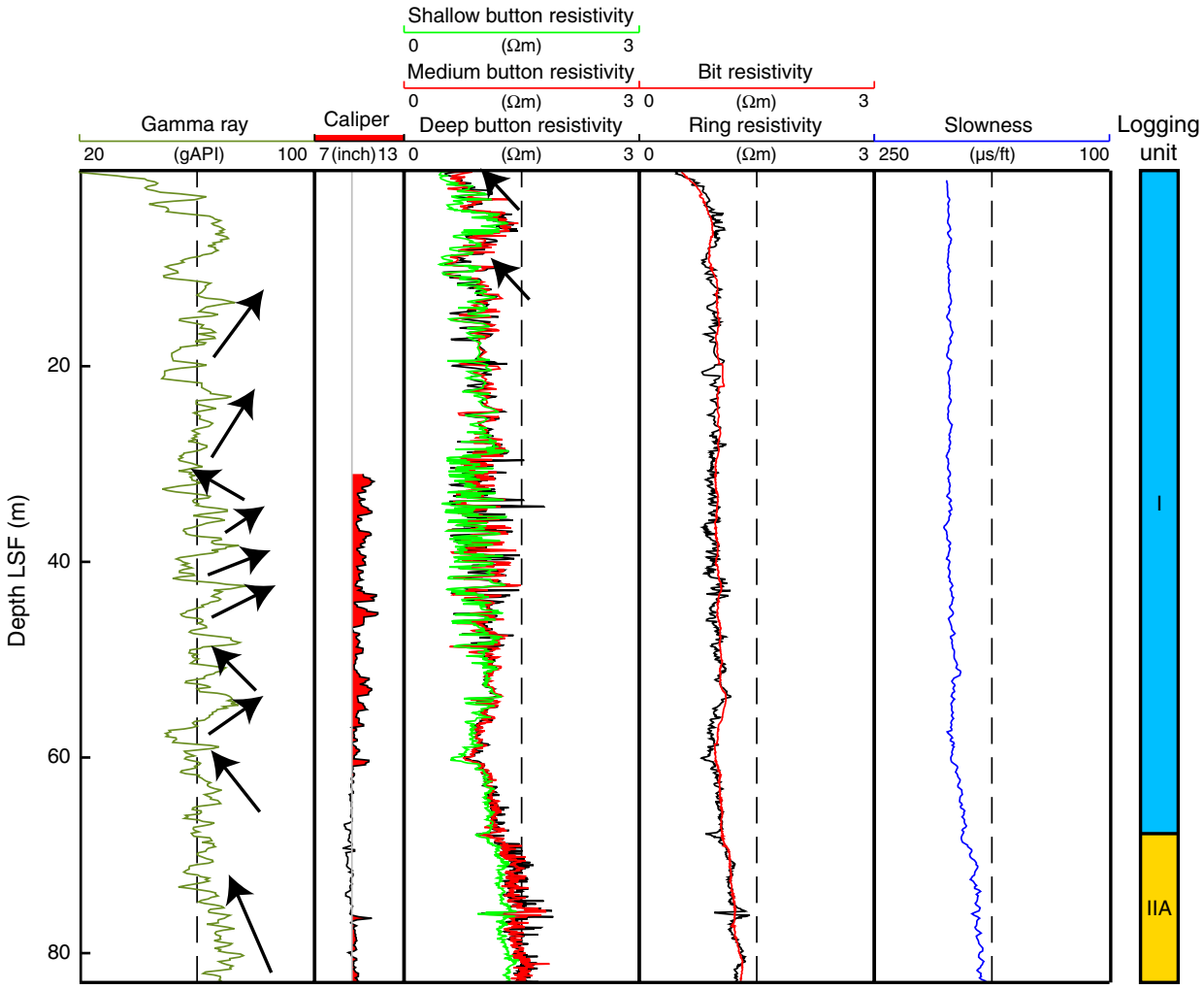

Figure F14. Boundary between logging Units I and II. Stratified and laminated sediments in logging Unit I and structureless sediments in logging Unit II separated by a conductive unconformity surface. LSF = LWD depth below seafloor.

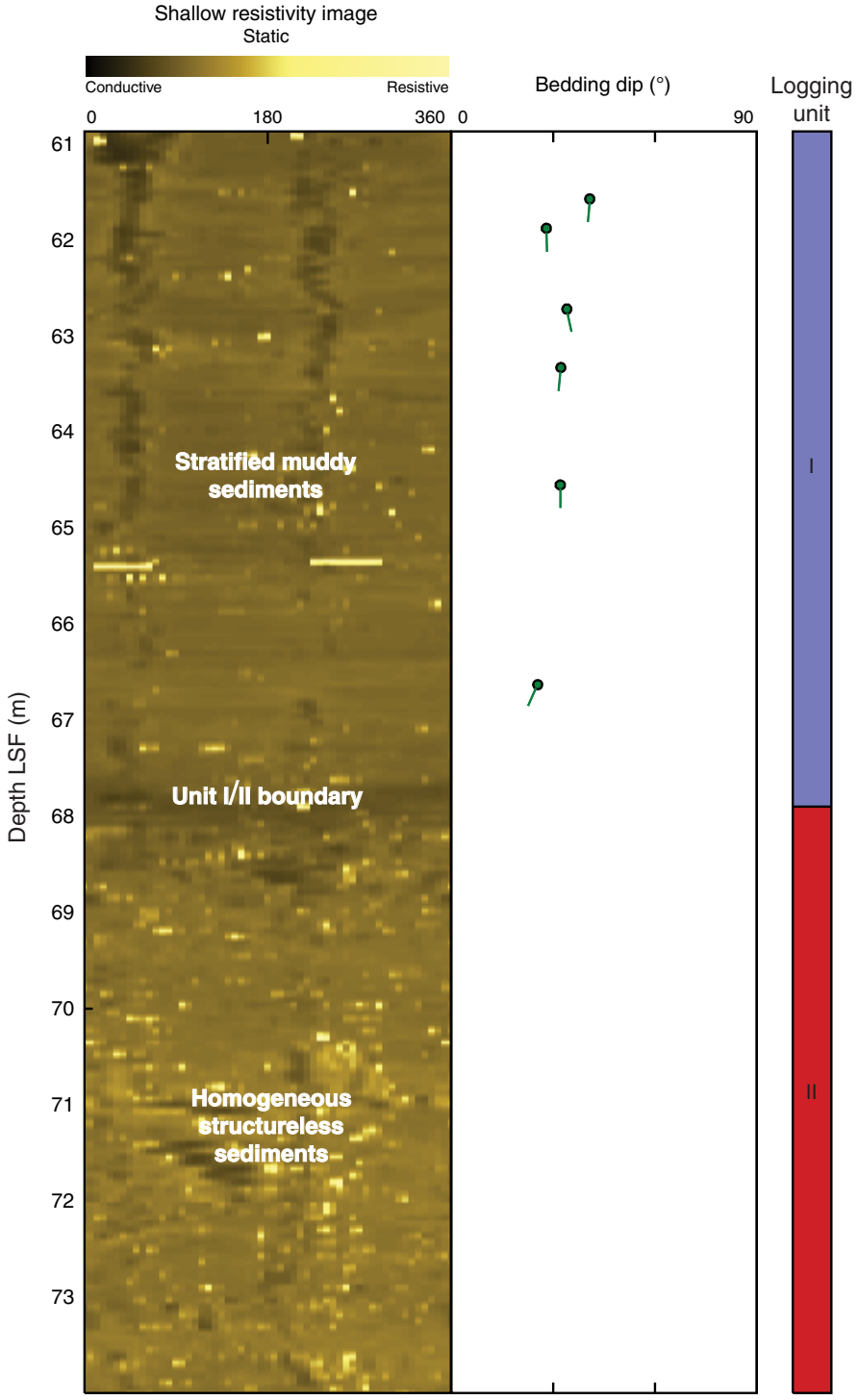

Figure F15. Detailed section of logging Subunit IIC showing the dominant gamma ray trends. LSF = LWD depth below seafloor.

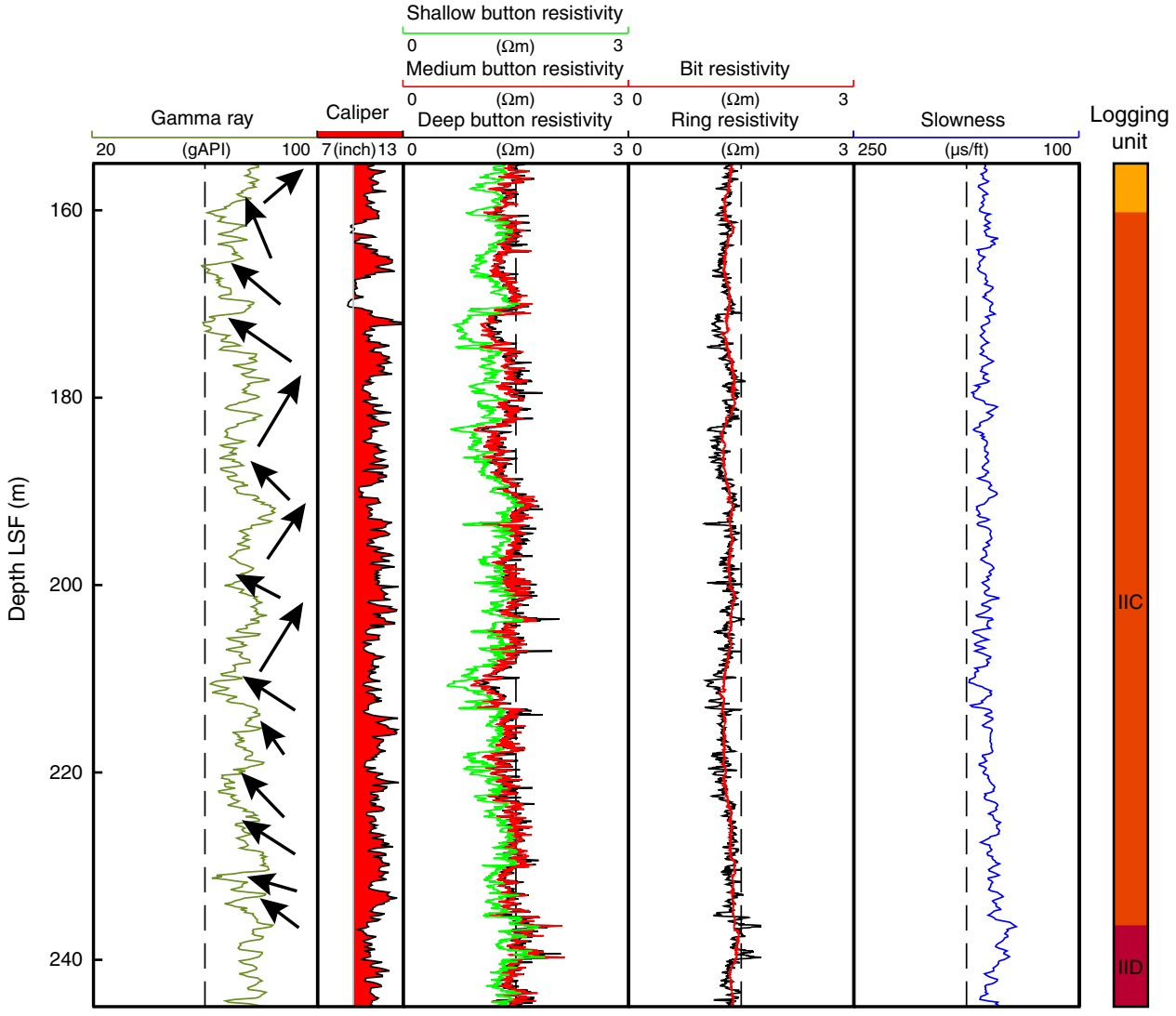

Figure F16. Boundary between logging Units II and III. Pink = zones of fluctuating resistivity and larger borehole diameter, light blue = zones of constant resistivity and smaller borehole diameter. LSF = LWD depth below seafloor, RAB = resistivity-at-the-bit.

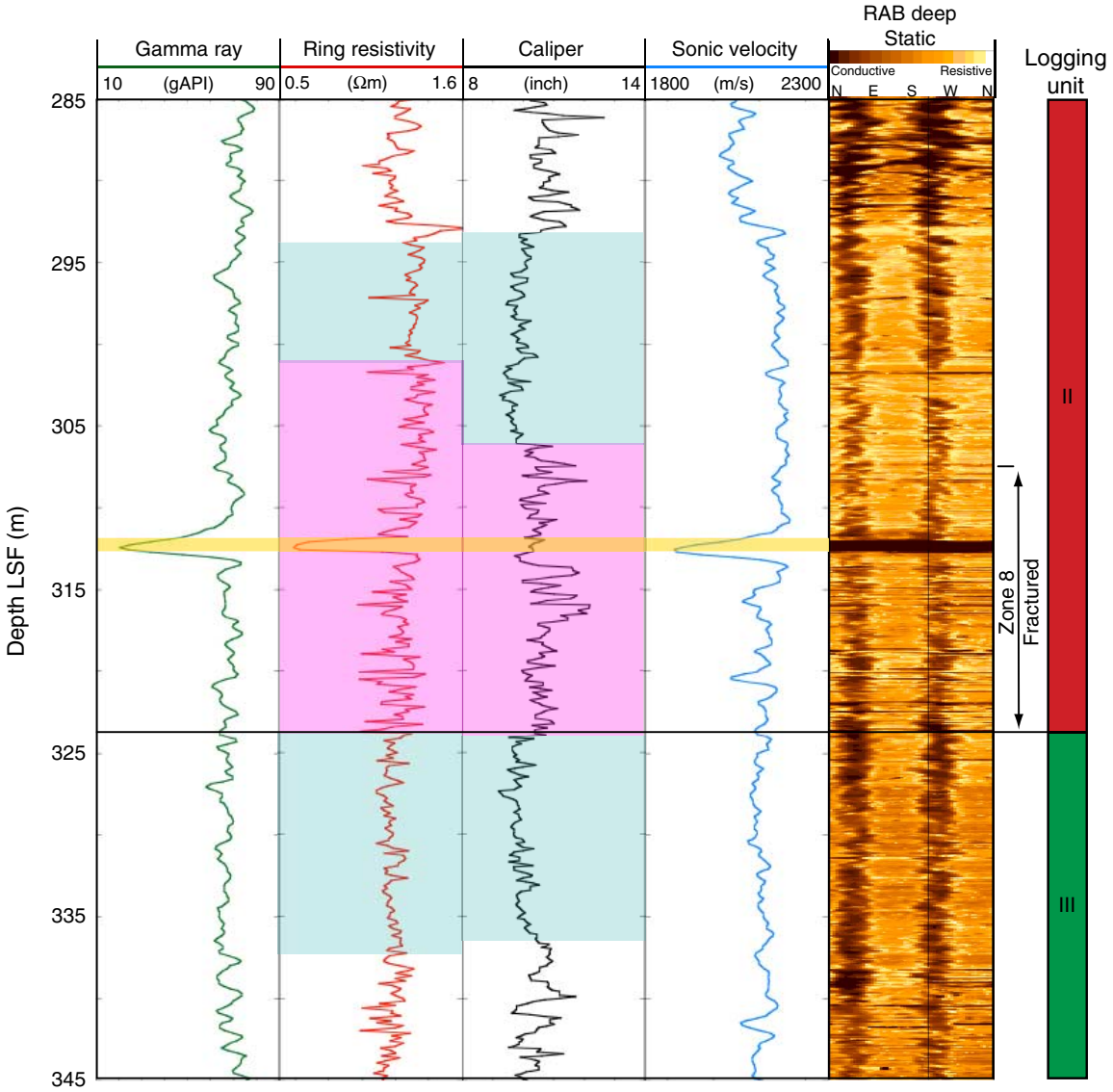

Figure F17. Statistical distribution of gamma ray values for the logging units at each site. Box outline = 25th to 75th percentile, separated by the mean. All units shown in the figure are logging units. Logging Unit I in Holes C0001D and C0004B have a very similar range, as does logging Unit II from those two sites.

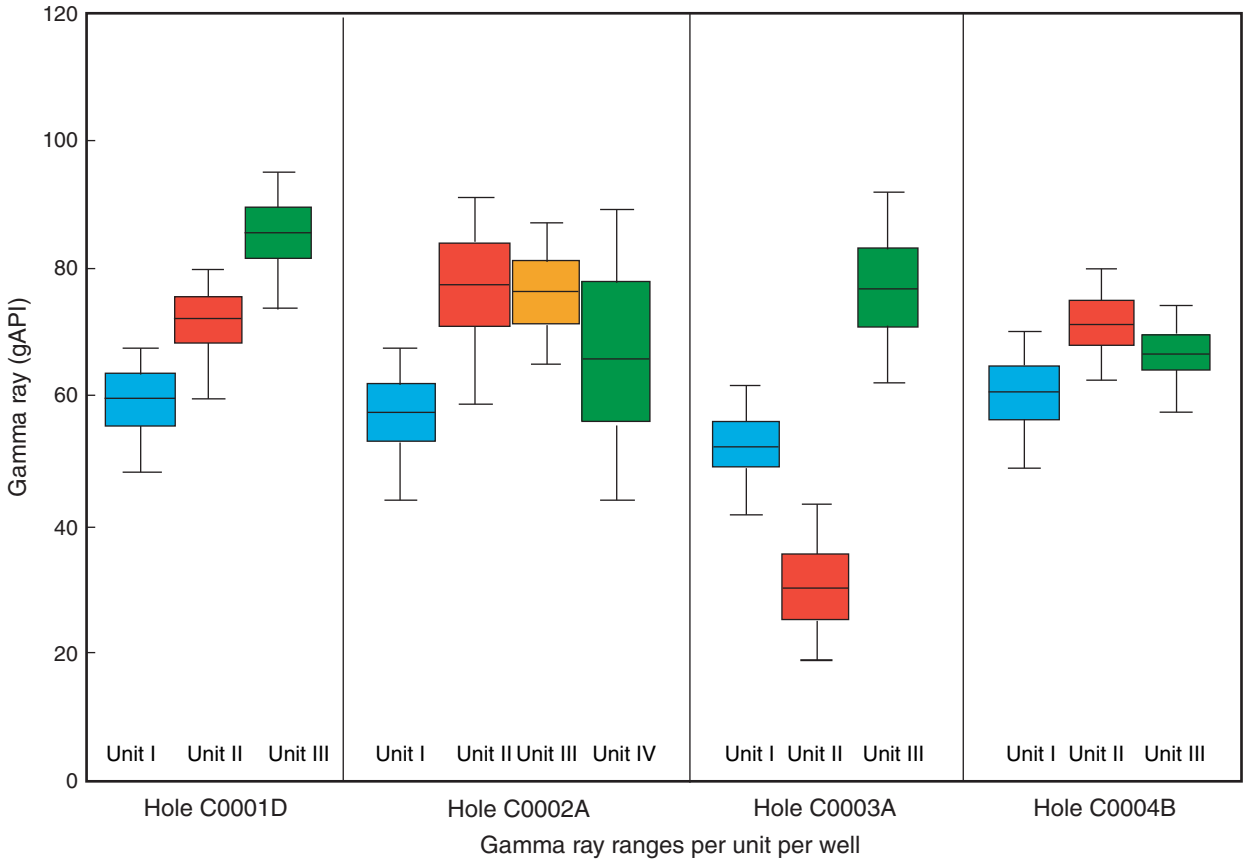

Figure F18. All resistivity curves acquired at Site C0004. Light gray = minor fracture zones, dark gray = major fracture zones (see Fig. F28). LSF = LWD depth below seafloor.

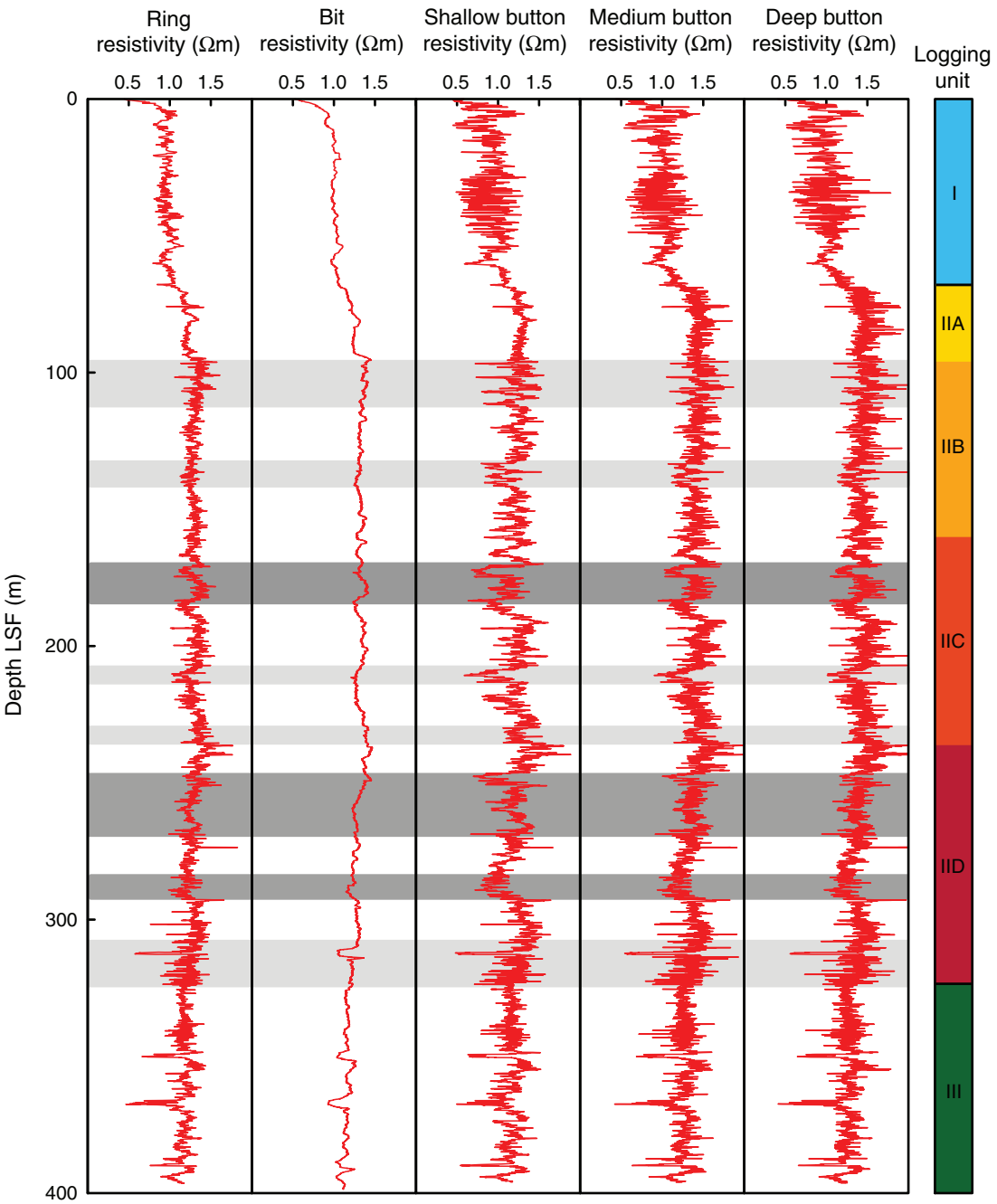

Figure F19. Plots of (**A**) bit vs. ring resistivity and (**B**) deep vs. shallow button resistivity. Black line = line of unit slope passing through the origin.

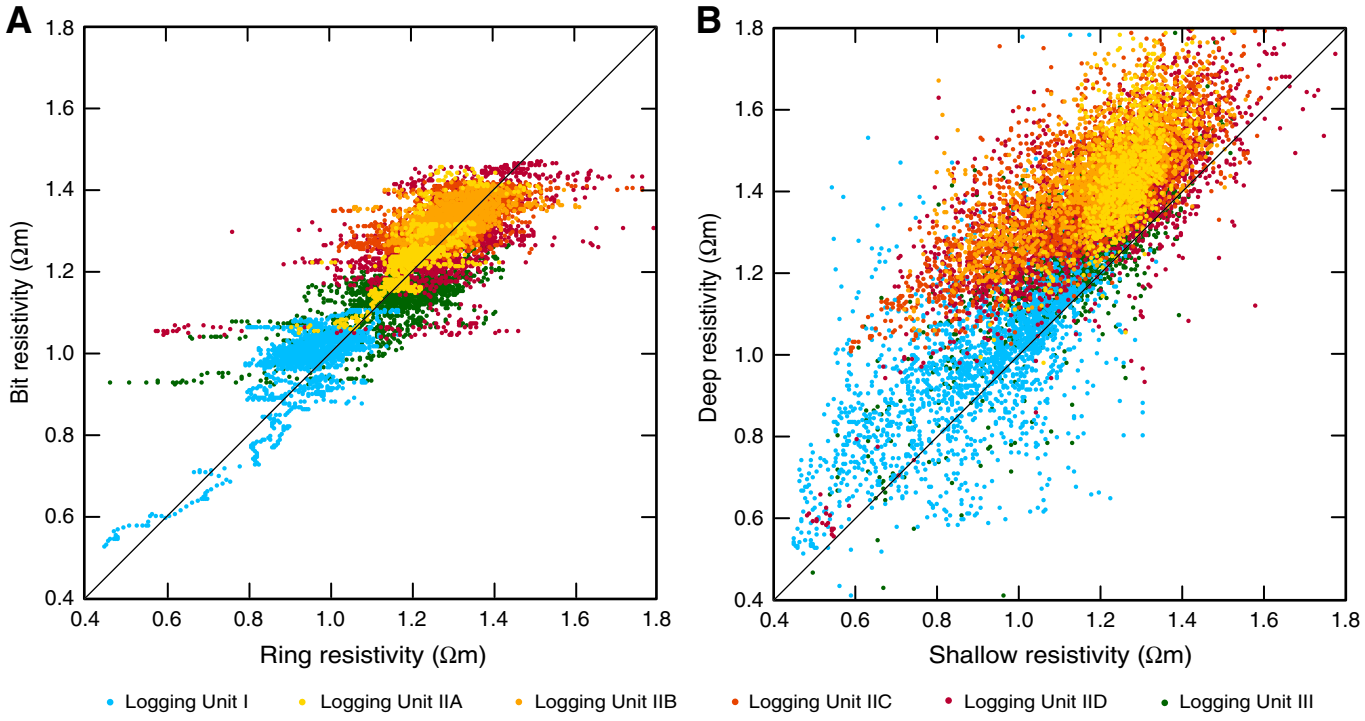

Figure F20. Bit and ring resistivity–derived porosity and density calculated from them. Porosity derived using Archie's law with parameters a = 1 and m = 2.4. Light gray = minor fracture zones, dark gray = major fracture zones (see Fig. F28).

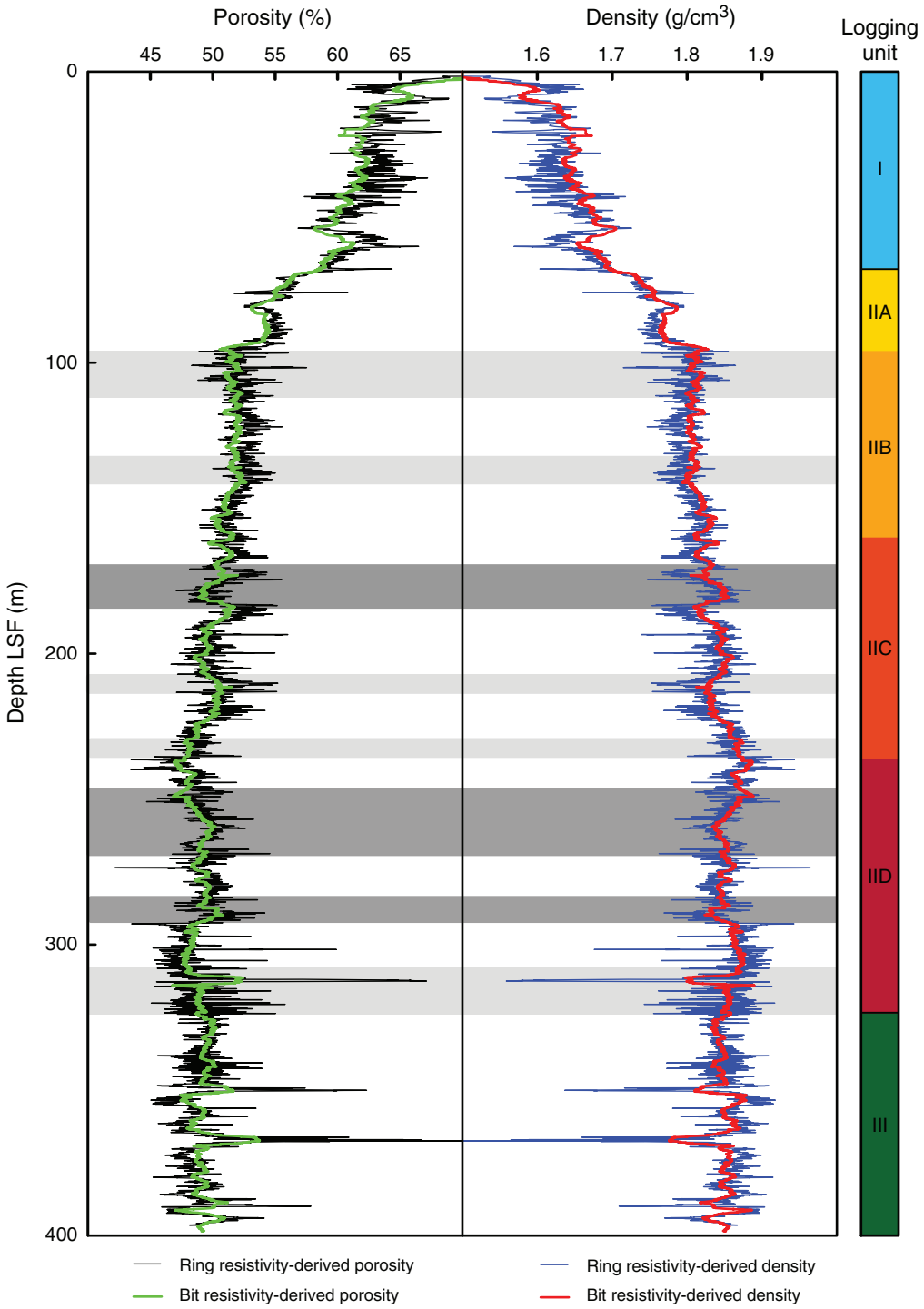

Figure F21. Sonic *P*-wave velocity log at Site C0004. Light gray = minor fracture zones, dark gray = major fracture zones (see Fig. F28).

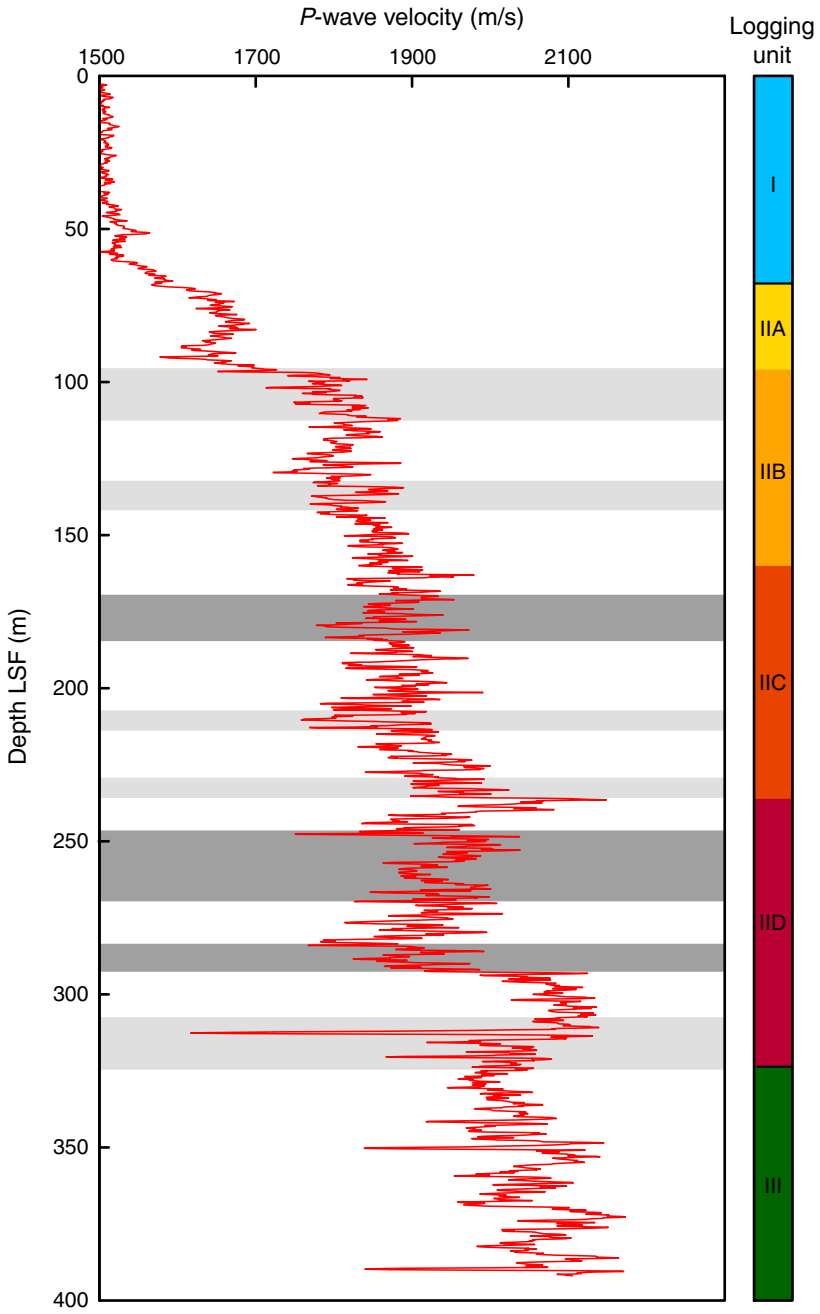

Figure F22. A. Breakout azimuth vs. depth. Note that breakouts in structural Domain 1 show more northerly azimuths than those in Domains 2 and 3. Also note that the variation of azimuth orientation is greatest in structural Domain 2. **B.** Breakout width vs. depth. Note that breakouts in structural Domain 2 are wider than those in Domains 1 and 3.

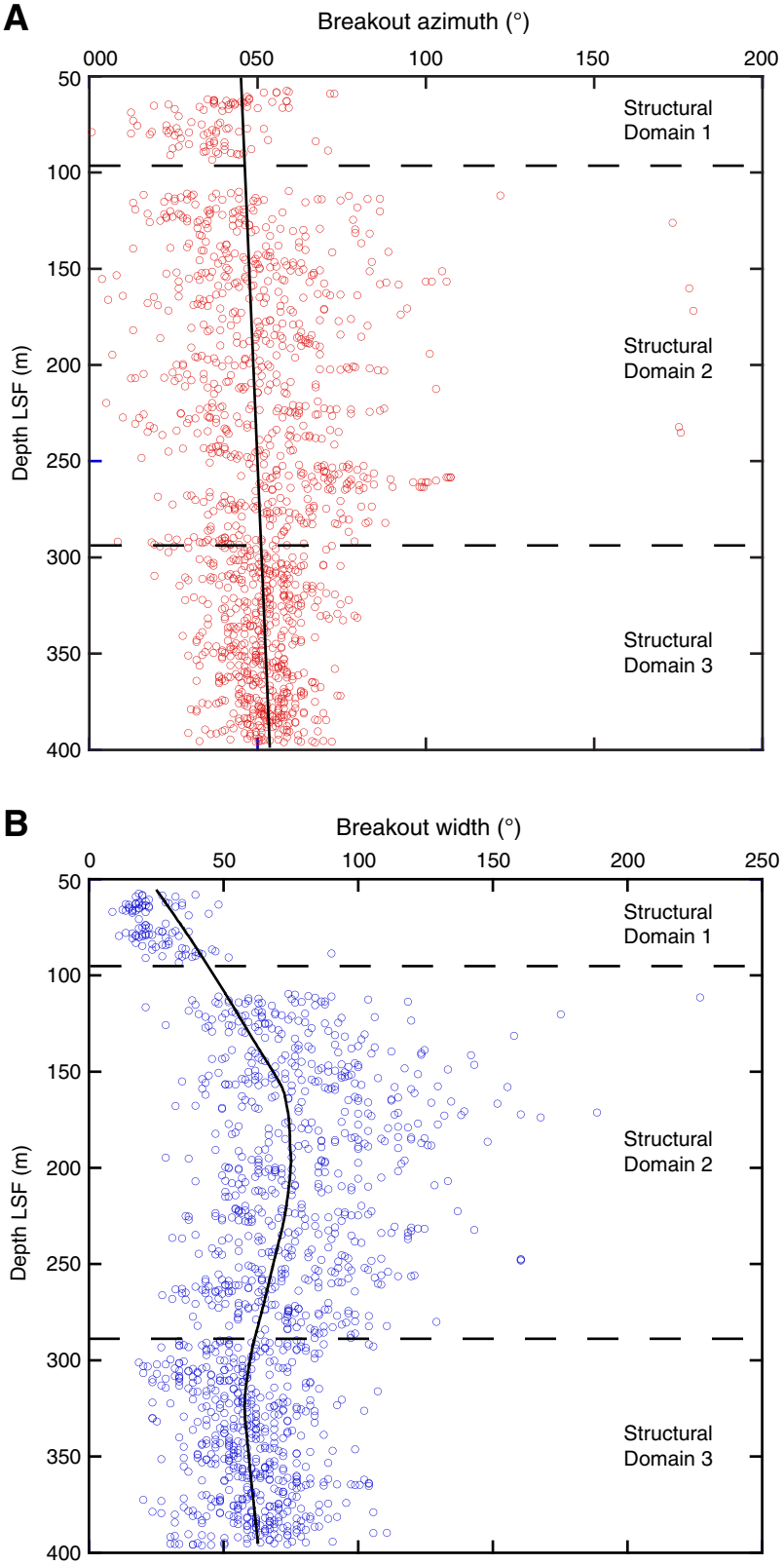

Figure F23. Plots of sonic *P*-wave velocity vs. (**A**) bit resistivity and (**B**) ring resistivity.

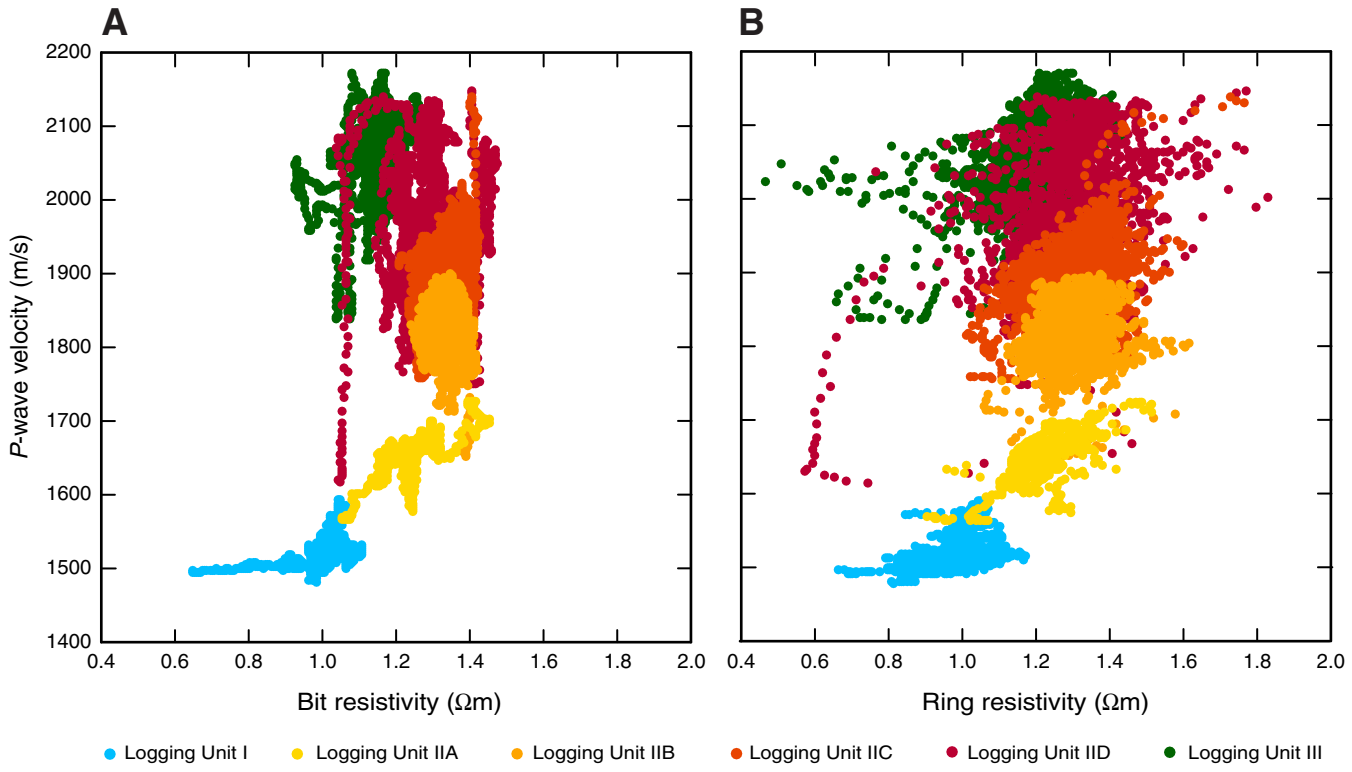

Figure F24. Plots of sonic *P*-wave velocity vs. (**A**) bit resistivity-derived porosity and (**B**) ring resistivity-derived porosity.

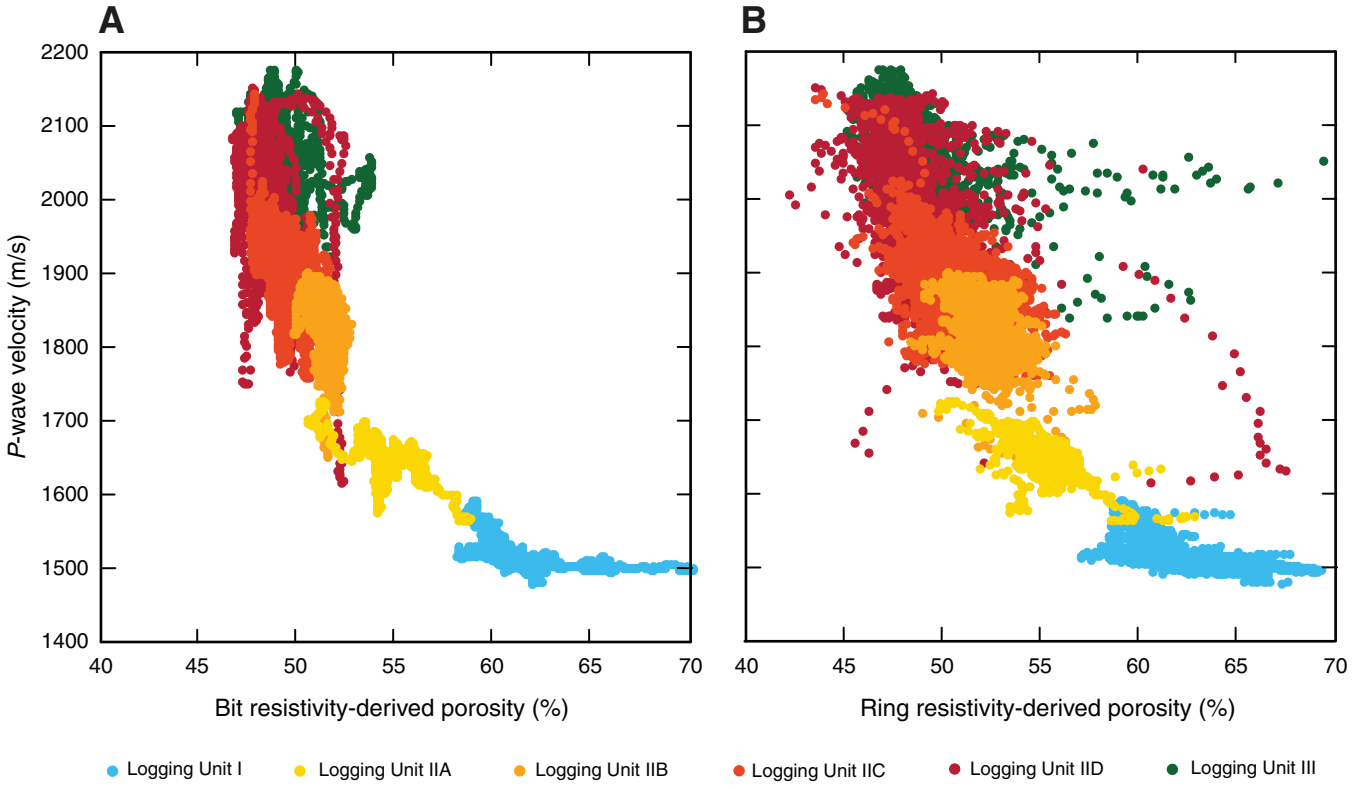

Figure F25. Shallow resistivity image (dynamic normalization) in Hole C0004B and measured orientations and dips of bedding (pink, left) and fractures (right). Tadpole lines = dip direction of the plane. LSF = LWD depth below seafloor.

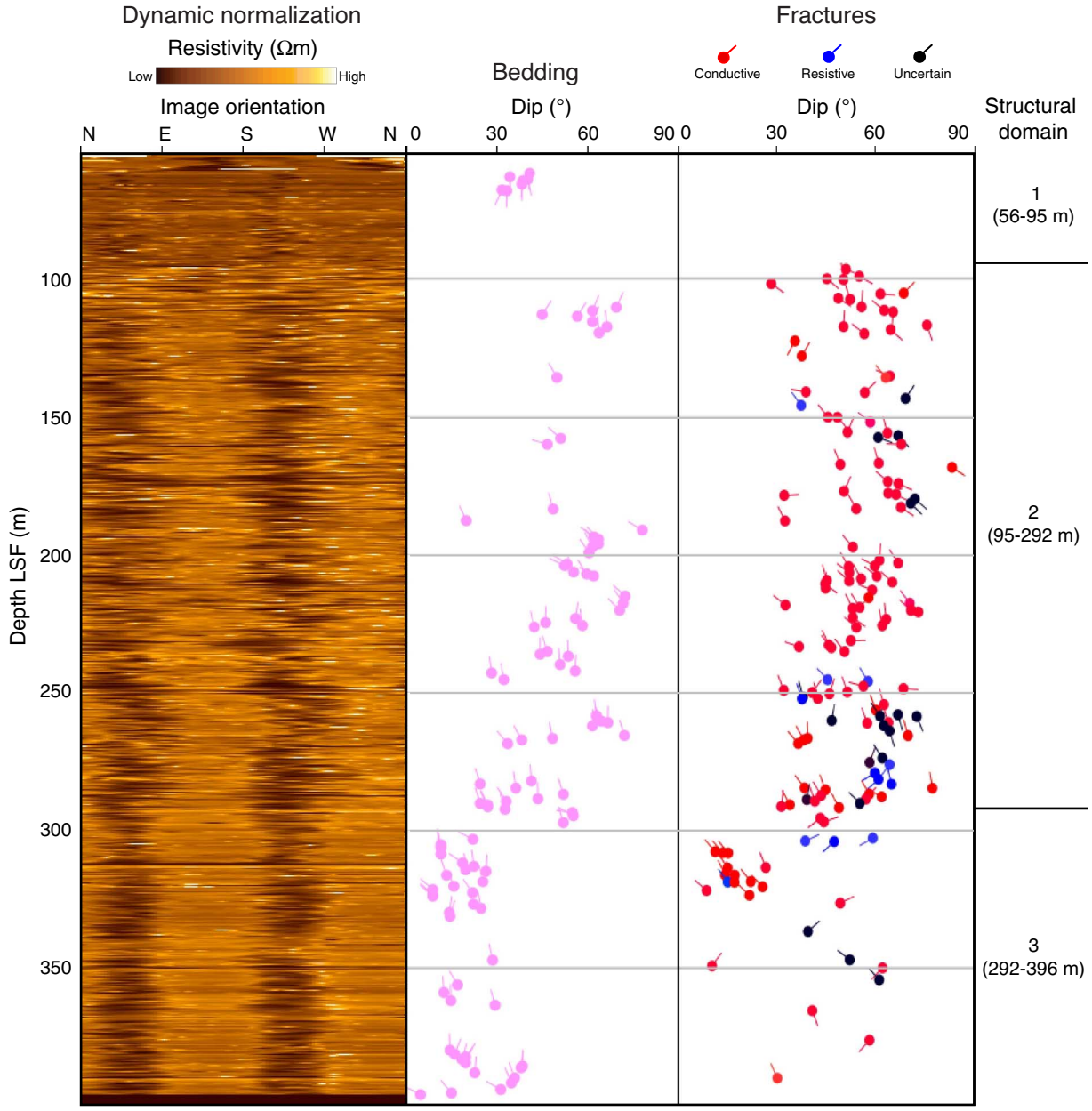

Figure F26. Equal area lower hemisphere stereographic projection of poles to bedding planes in structural Domains 1, 2, and 3.

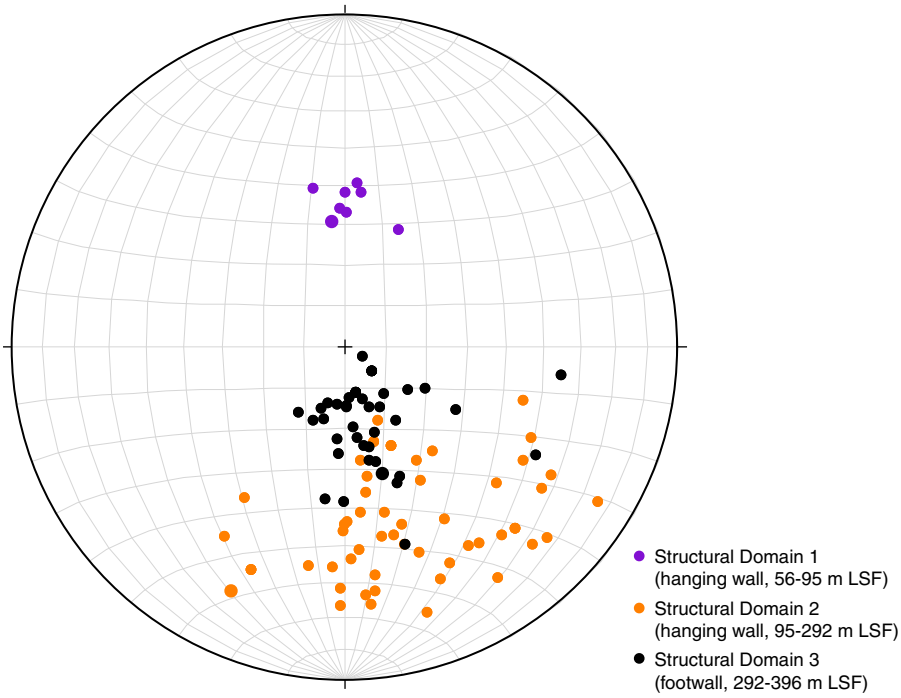

Figure F27. Equal area lower hemisphere stereographic projections of poles to fracture planes (left). **A.** Fractures divided into structural Domains 2 and 3 (no natural fractures were identified in structural Domain 1). Rose diagrams (right) represent fracture azimuths (shown as dip direction –90°), preserving dip direction information. **B.** Poles of all fractures within the borehole differentiated according to conductivity.

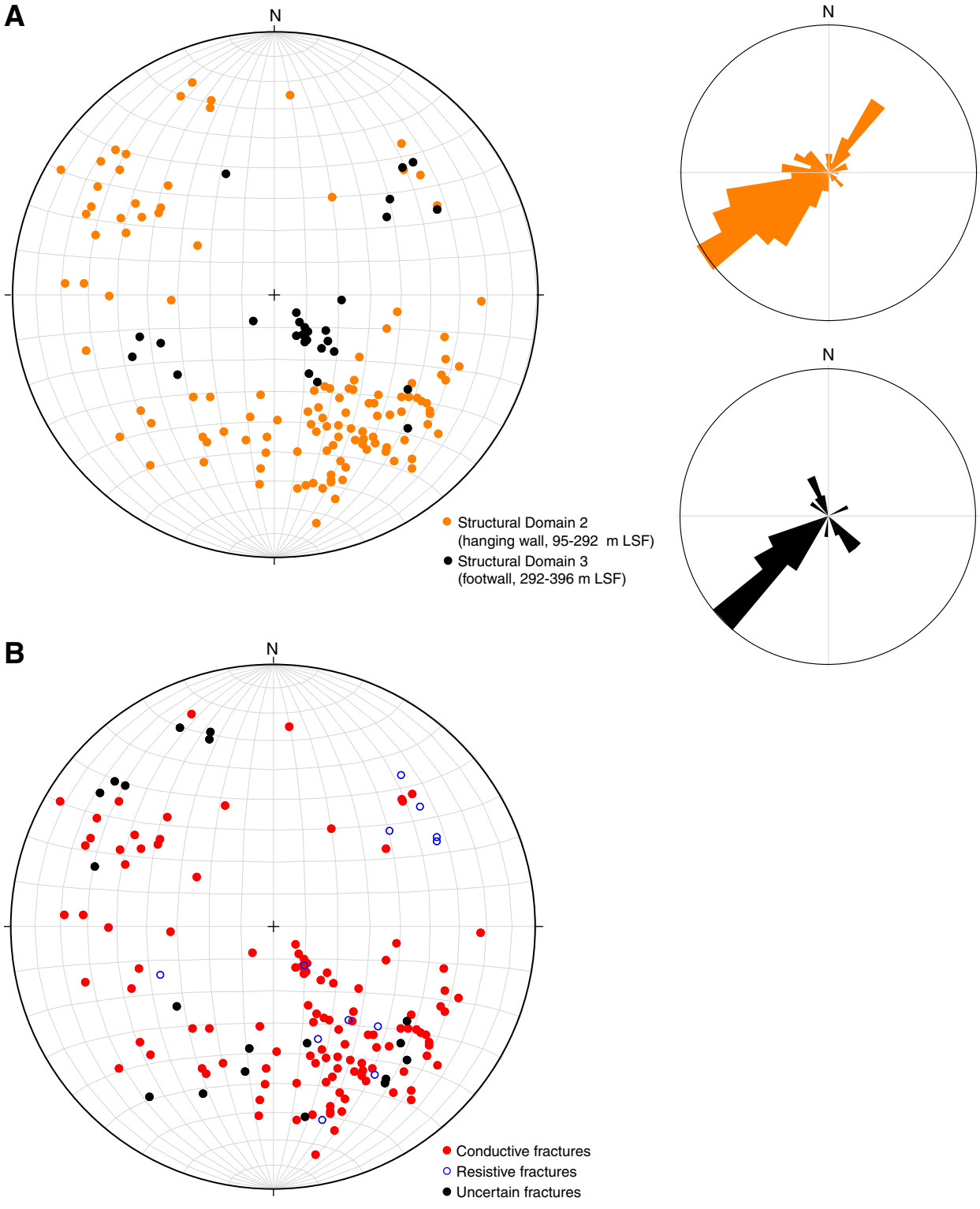

Figure F28. Fracture frequency (bin size = 3.3 m) and fractured zones with depth. Several prominent fractured zones were identified, predominantly within structural Domain 2 (thrust sheet or hanging wall; 95–292 m LWD depth below seafloor [LSF]), characterized by the frequent occurrence of conductive fractures, widened breakouts, and/or broad conductive zones. The shallowest zone (95–112 m LSF) is distinct with no breakouts and a patchy texture.

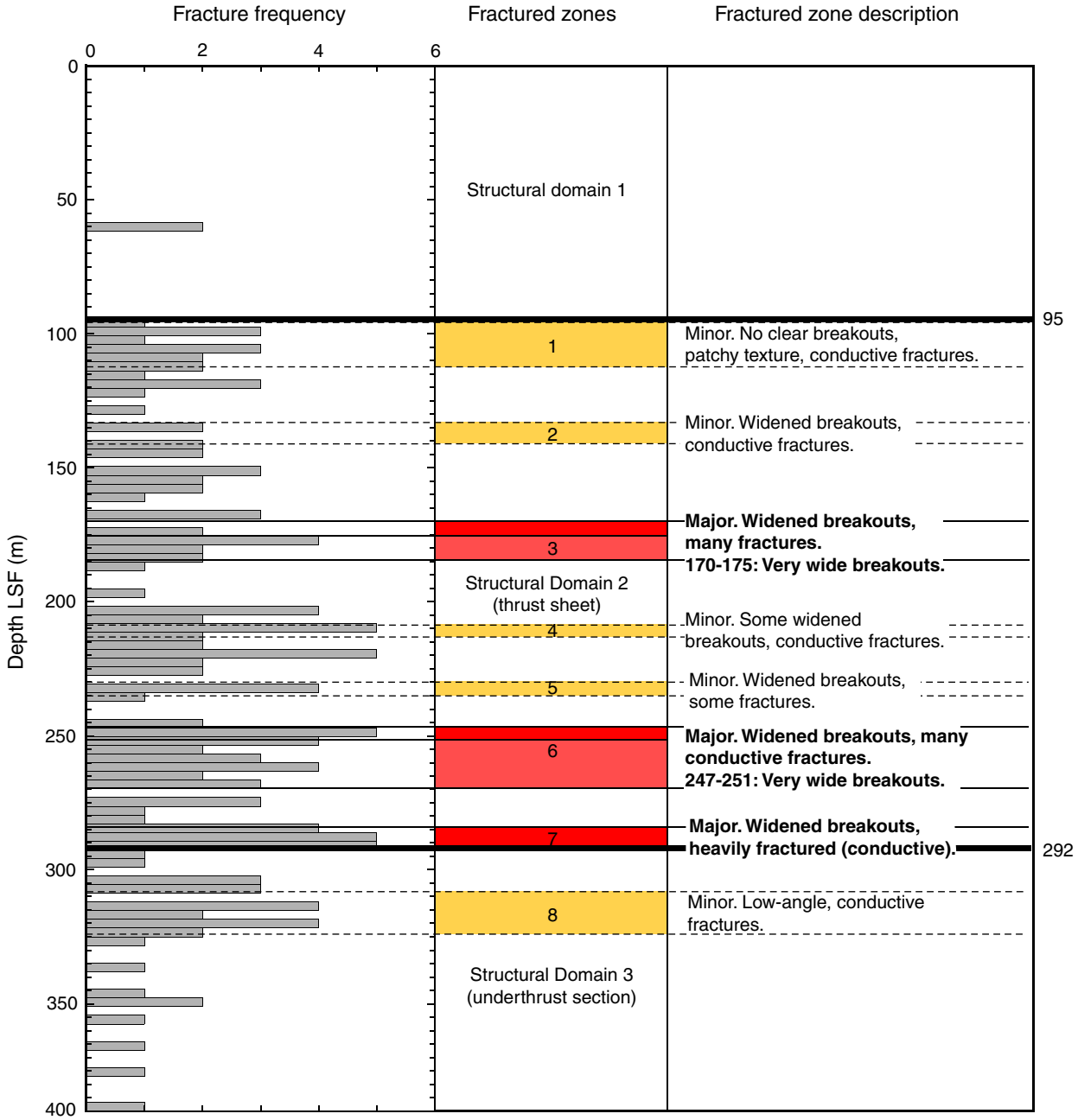

Figure F29. Borehole image of fractured Zone 3 (162–188 m LWD depth below seafloor [LSF]). Prominent conductive fractures occur as dark areas cutting across the image. Breakouts are imaged as irregular vertical conductive bands 180° apart. Breakouts tend to widen and become more irregular near fractures. Tadpole lines = dip direction of fracture planes.

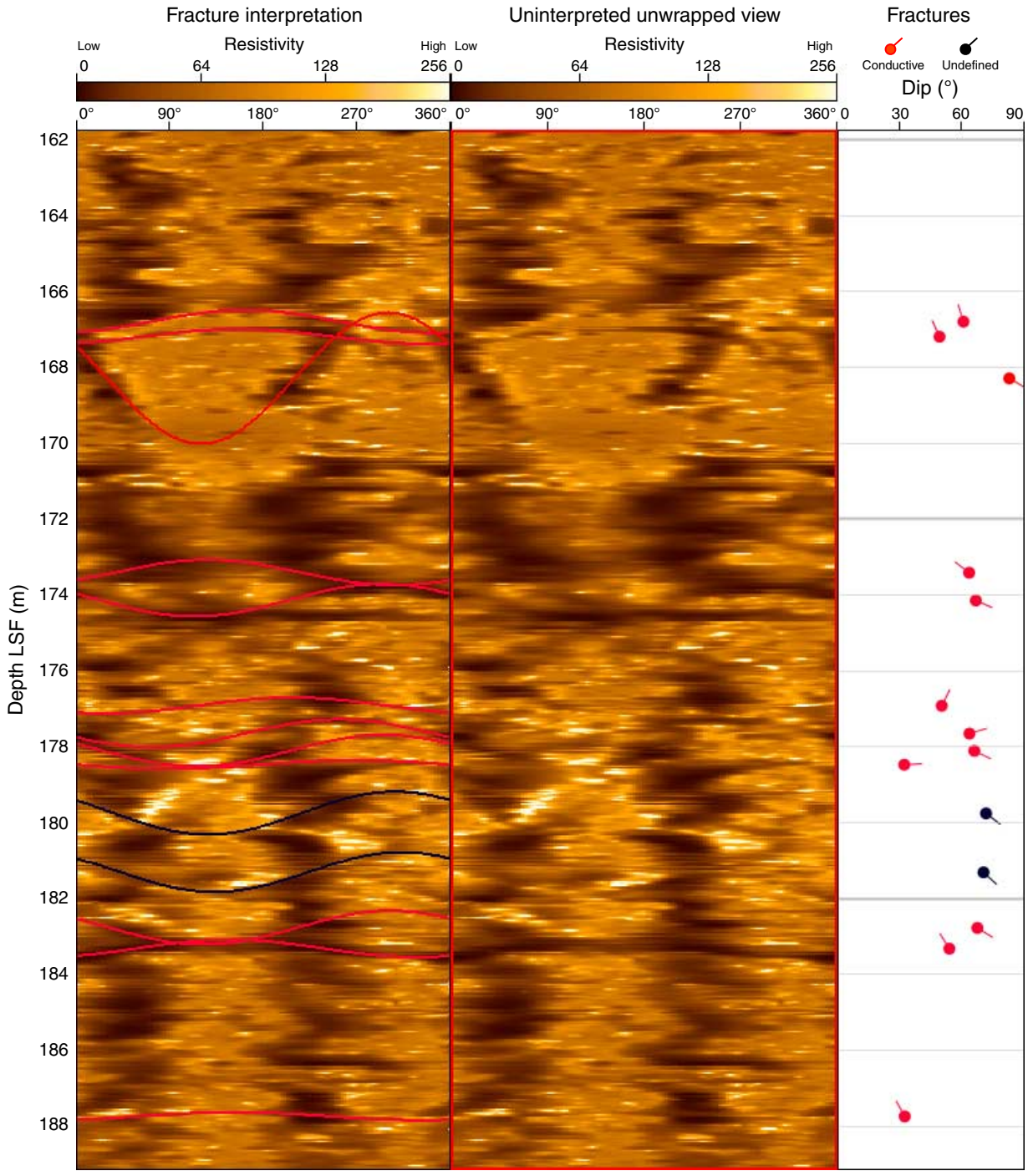

Figure F30. Borehole image of transition between structural Domains 2 and 3 between the hanging wall (thrust sheet) and footwall (underthrust sediments) of the main thrust fault. Note that breakouts are narrower and more uniform in width and fractures are less frequent below 290–292 m LWD depth below seafloor [LSF] in the footwall. Tadpole lines = dip direction of fracture planes.

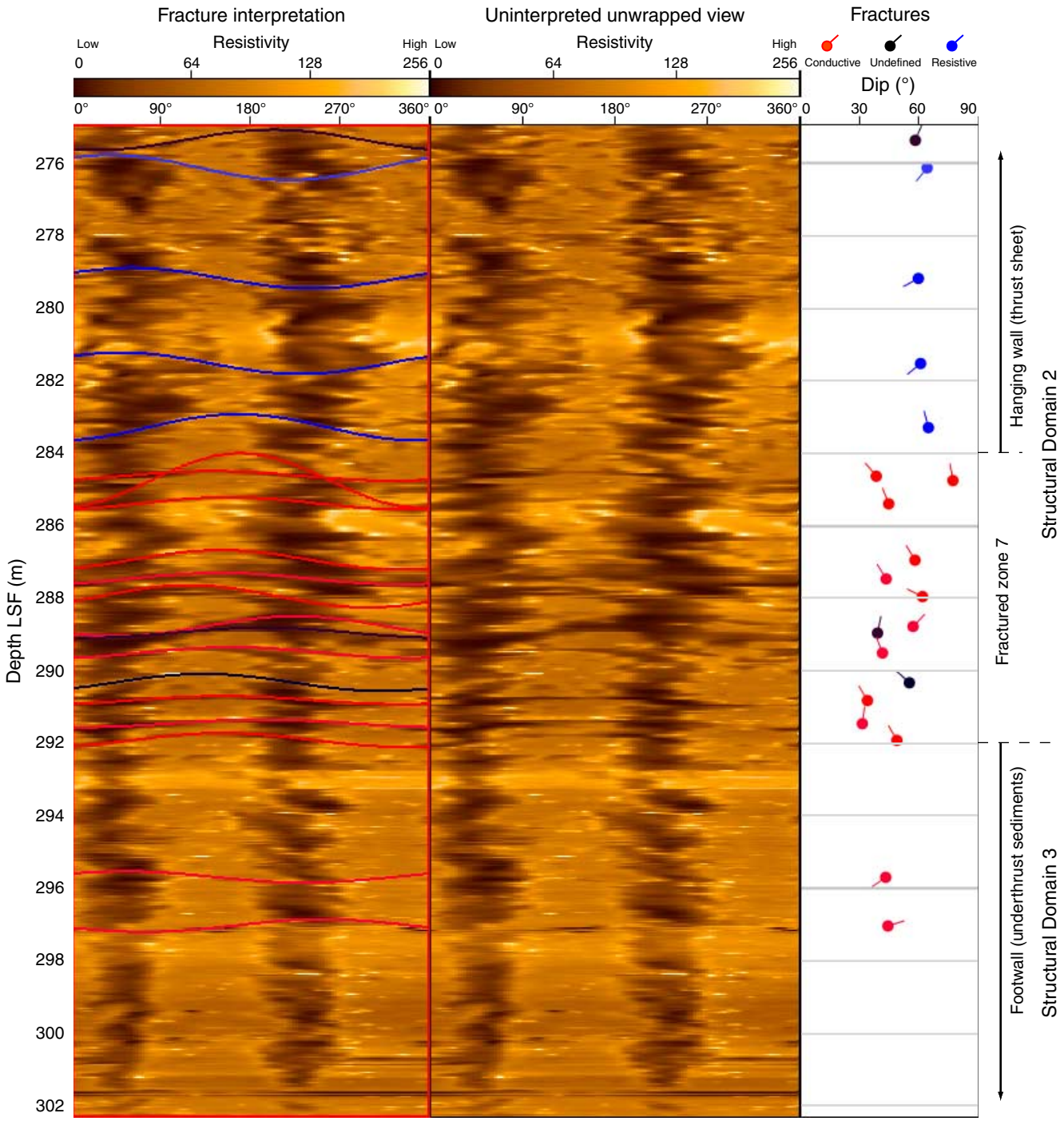

Figure F31. A. Histogram of breakout azimuth in Hole C0004A. **B.** Histogram of breakout width.

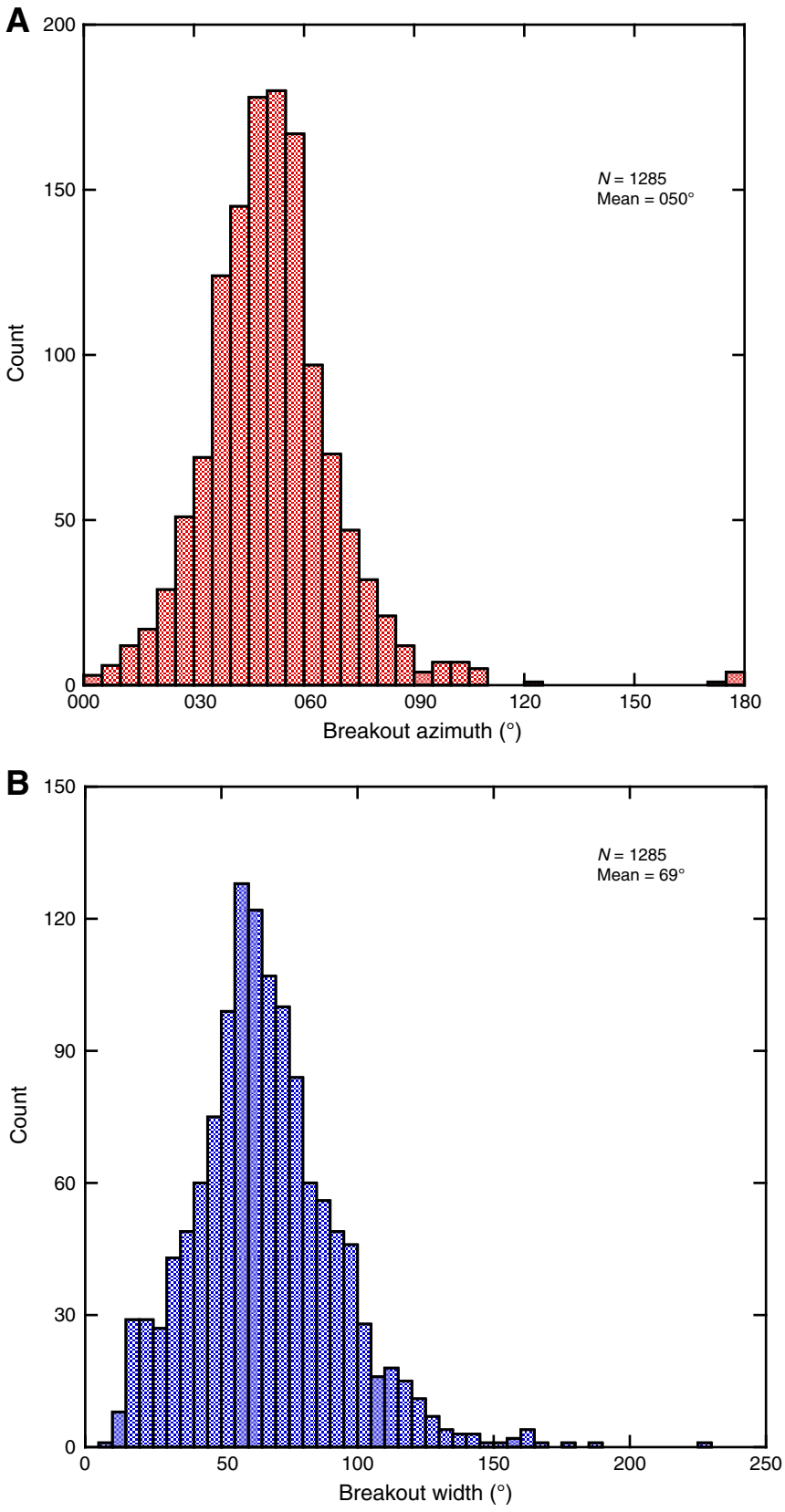

Figure F32. Stress polygons and likely stress regimes based on breakout widths and estimated uniaxial compressive strength (UCS) values at two depths in Hole C0004B. S_{Hmax} and S_{hmin} lie within the stress polygon, to the right of (or below) the red line and along a trajectory of rock strength, parallel to the blue lines. **A.** Structural Domain 2 (thrust sheet) at 200 m LSF. **B.** Structural Domain 3 (underthrust section) at 325 m LSF.

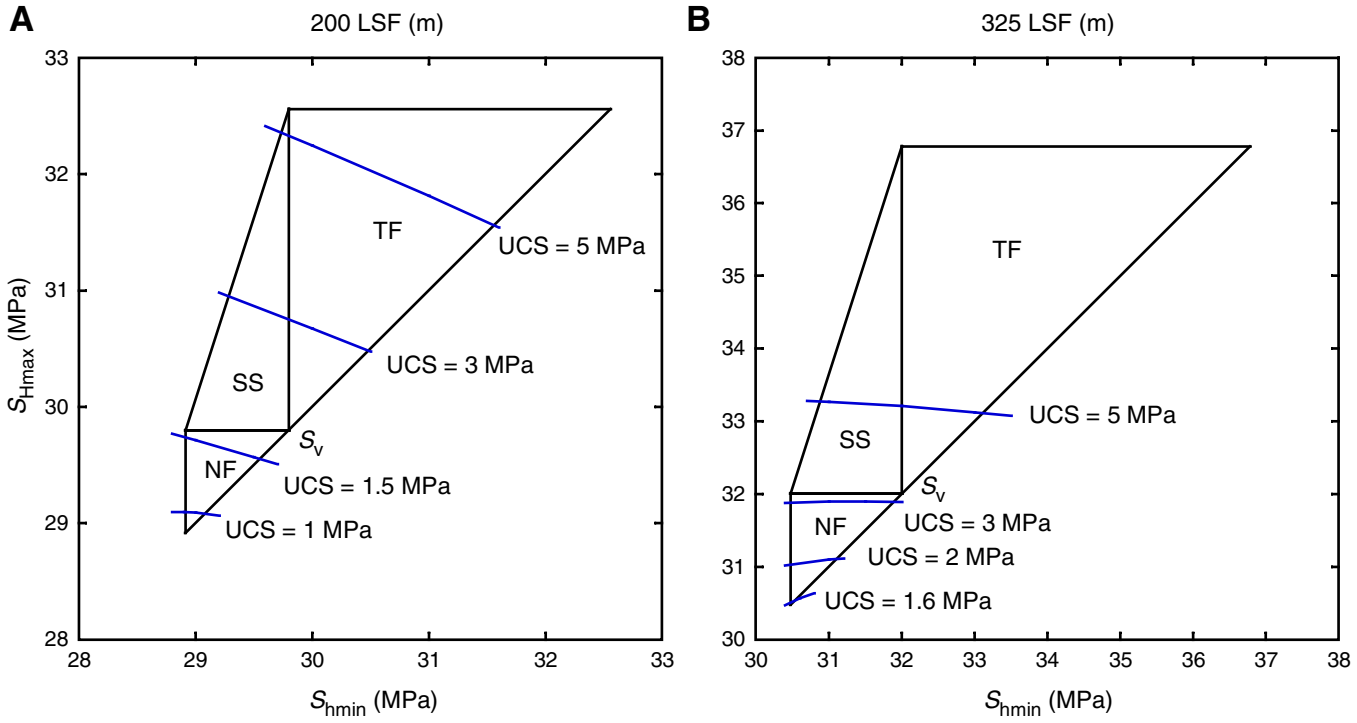

Figure F33. Correlation of fractured zones and seismic profile. Red = major fractured zones, yellow = minor fractured zones. LSF = LWD depth below seafloor.

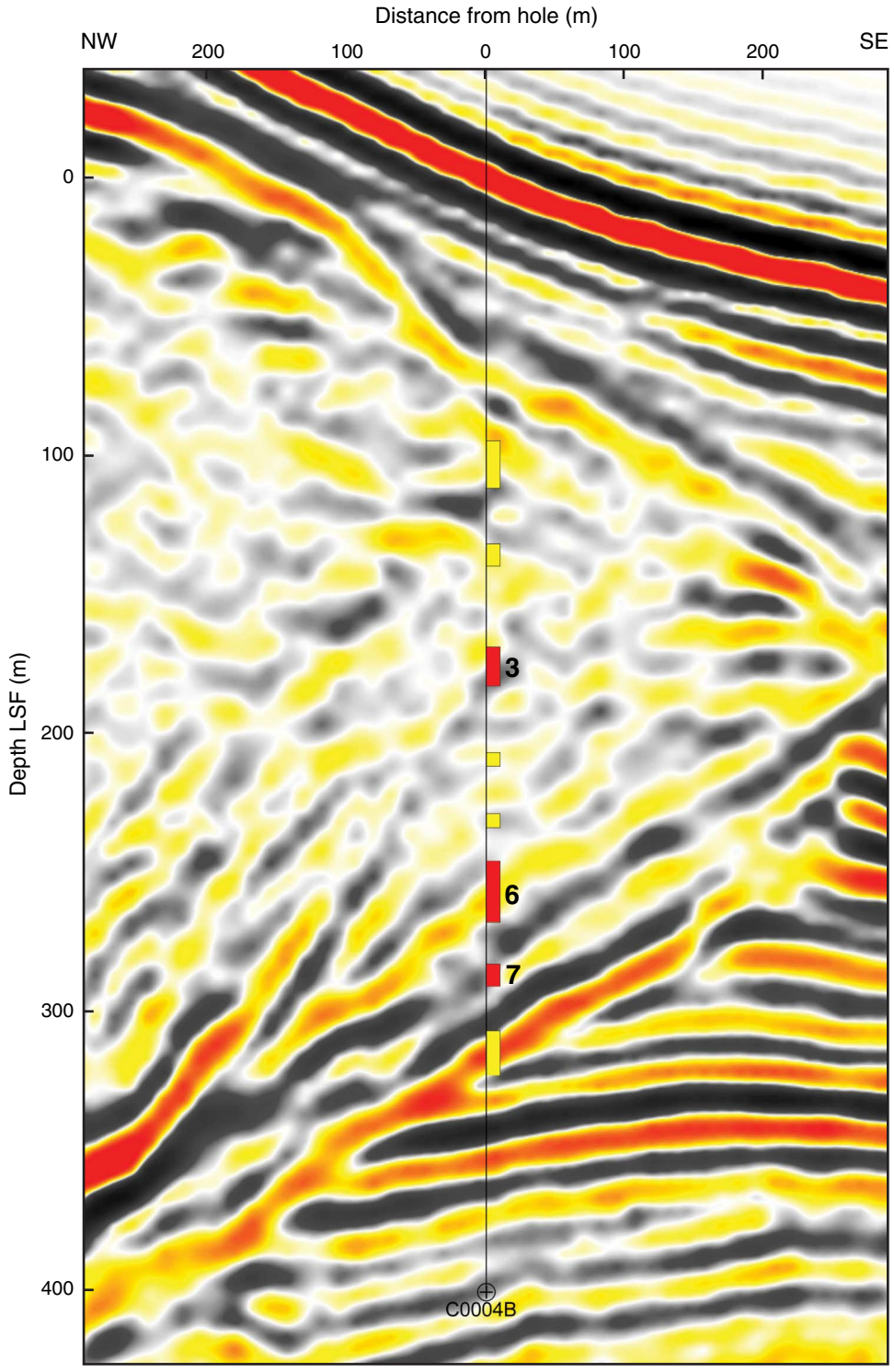

Figure F34. Seismic reflection section (check shot–corrected depth section for prestack depth-migrated Inline 2675) through Site C0004, with positive (red) and negative (black) seismic amplitudes. SSL = seismic depth below sea level, SSF = seismic depth below seafloor. Dashed lines in the vicinity of the site correspond to the reflectors shown in Table T7. Cyan = base of slope, dark blue = top of faulted section, green = bottom of faulted section, yellow = Footwall 1, magenta = Footwall 2. No vertical exaggeration.

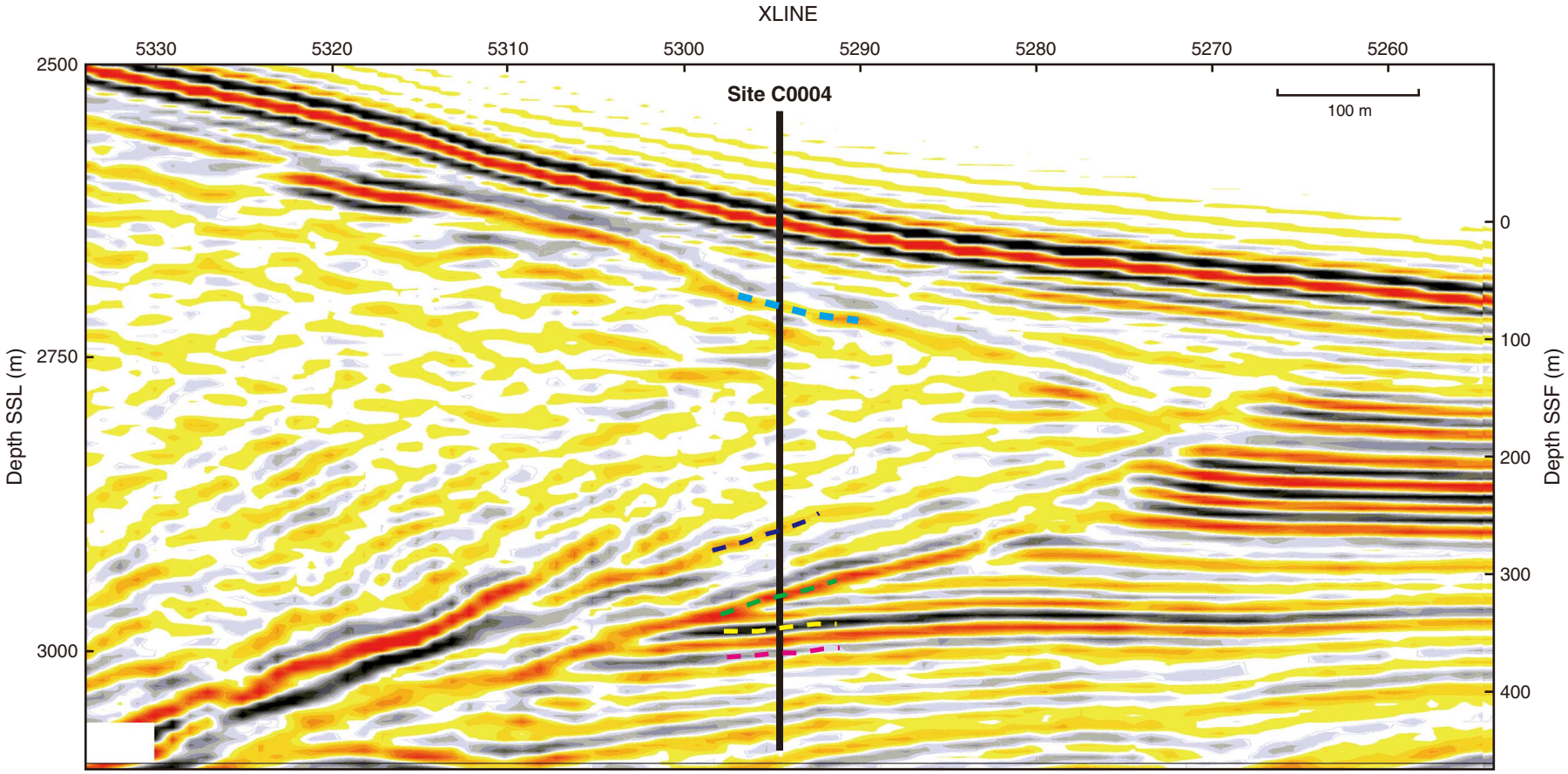

Figure F35. Logging units and subunits superimposed on check shot–corrected prestack depth-migrated seismic profile through Hole C0004B. LSF = LWD depth below seafloor, VE = vertical exaggeration.

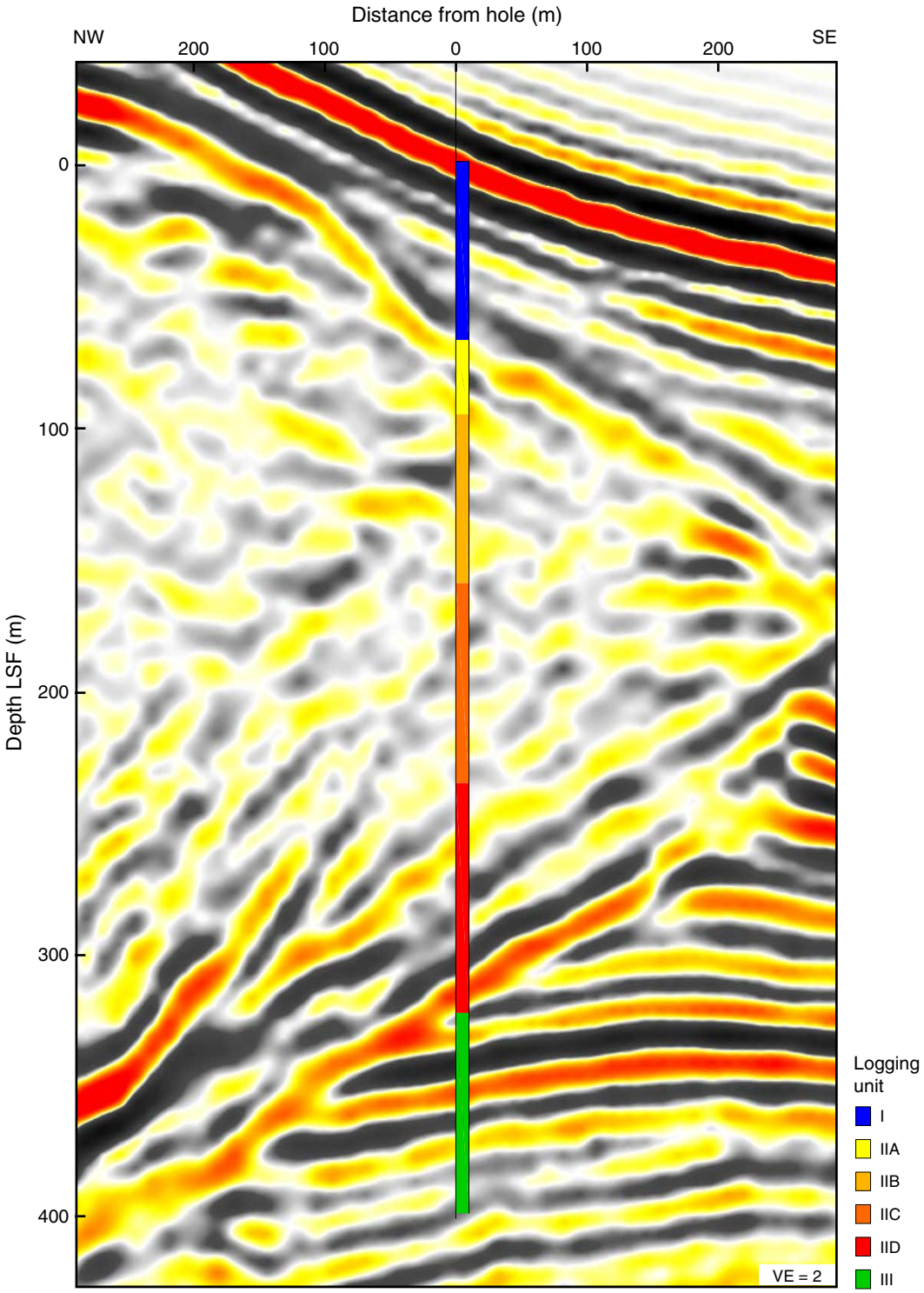

Figure F36. *P*-wave interval velocity from check shots (left) and sonic log (right) superimposed on check shot–corrected prestack depth-migrated seismic profile through Hole C0004B. LSF = LWD depth below seafloor, VE = vertical exaggeration.

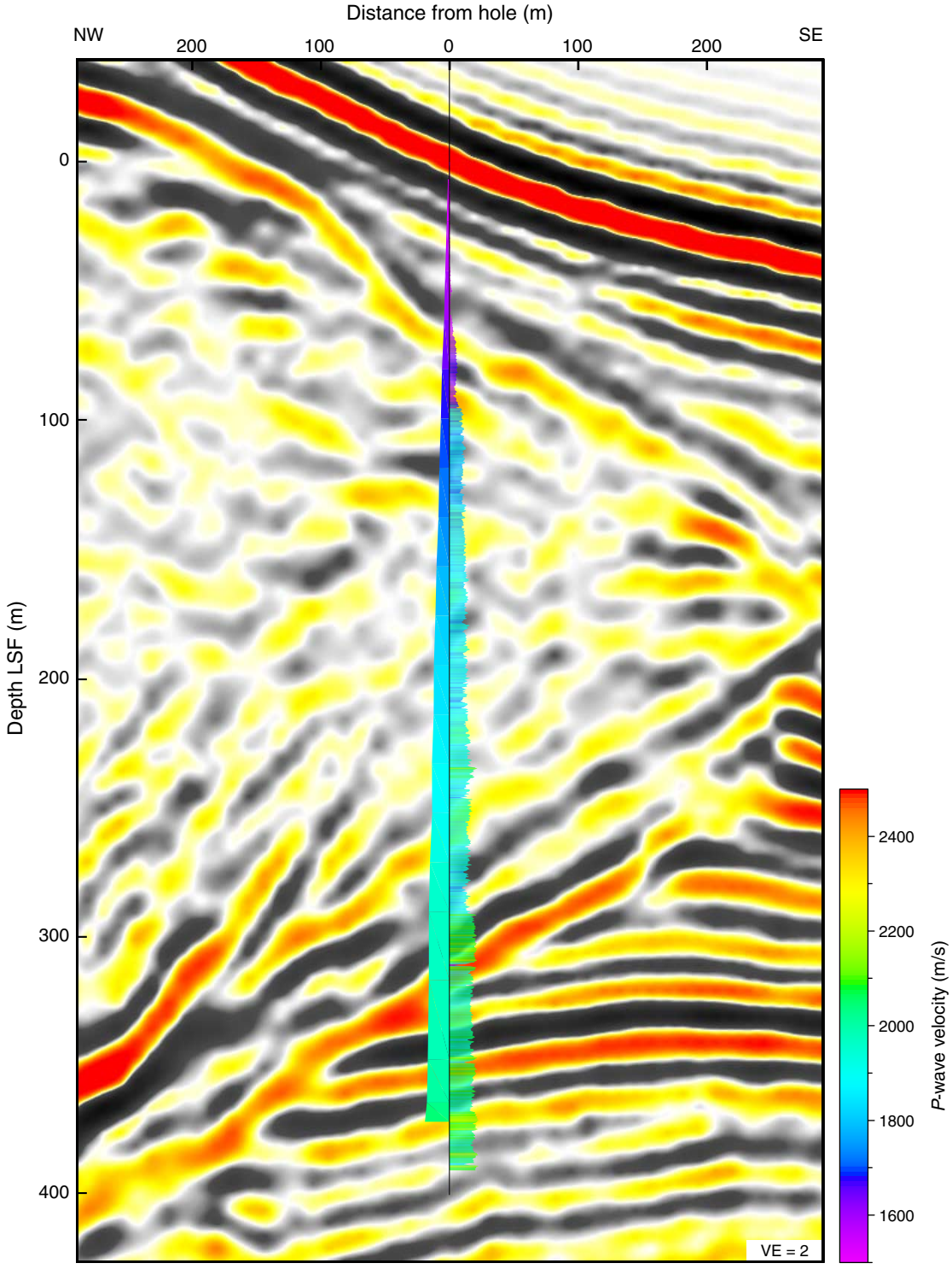

Figure F37. Gamma ray log superimposed on check shot–corrected prestack depth-migrated seismic profile through Hole C0004B. LSF = LWD depth below seafloor, VE = vertical exaggeration.

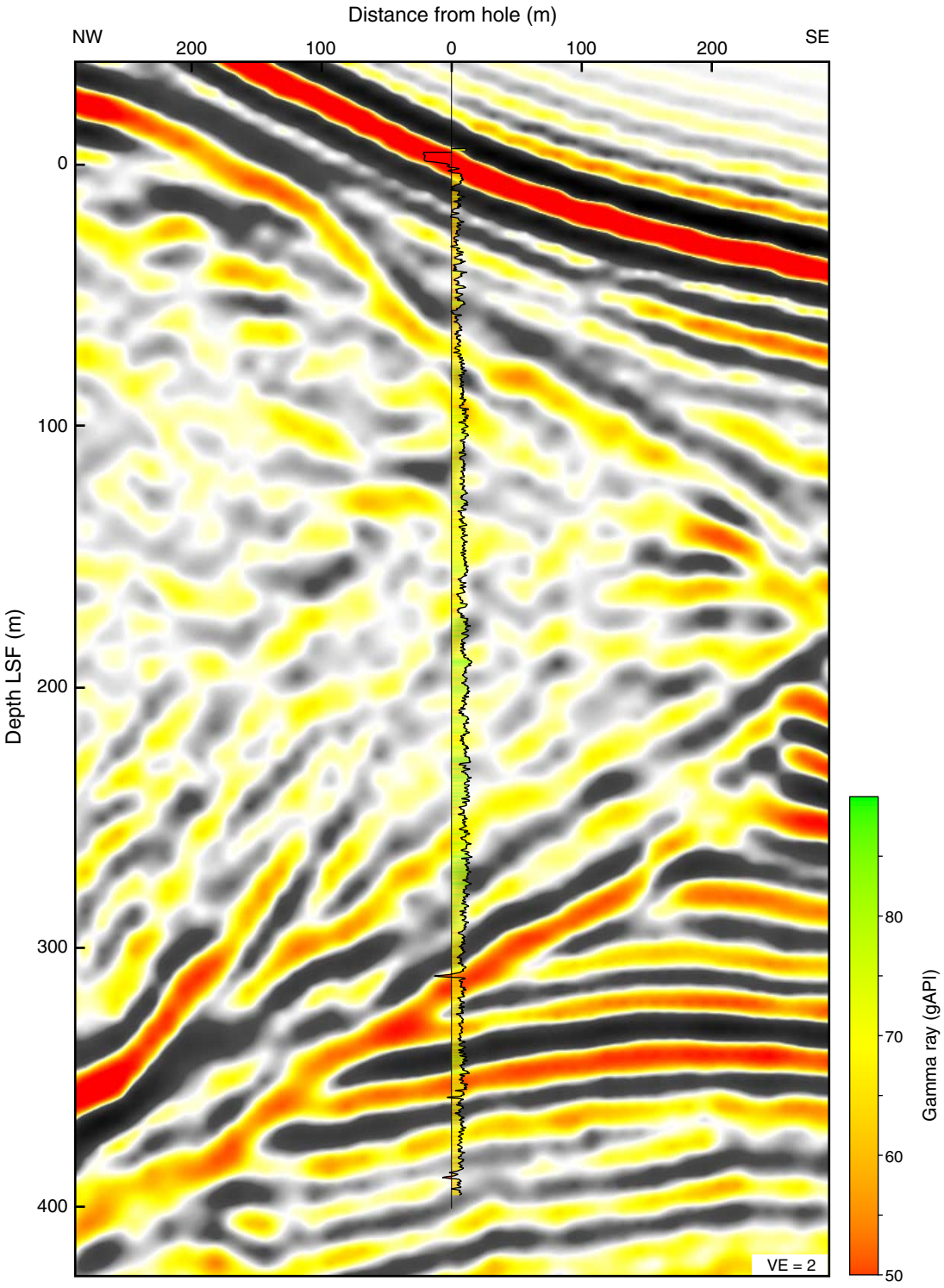

Figure F38. Ring (left) and bit (right) resistivity logs superimposed on check shot–corrected prestack depth-migrated seismic profile through Hole C0004B. Color scale is logarithmic. LSF = LWD depth below seafloor, VE = vertical exaggeration.

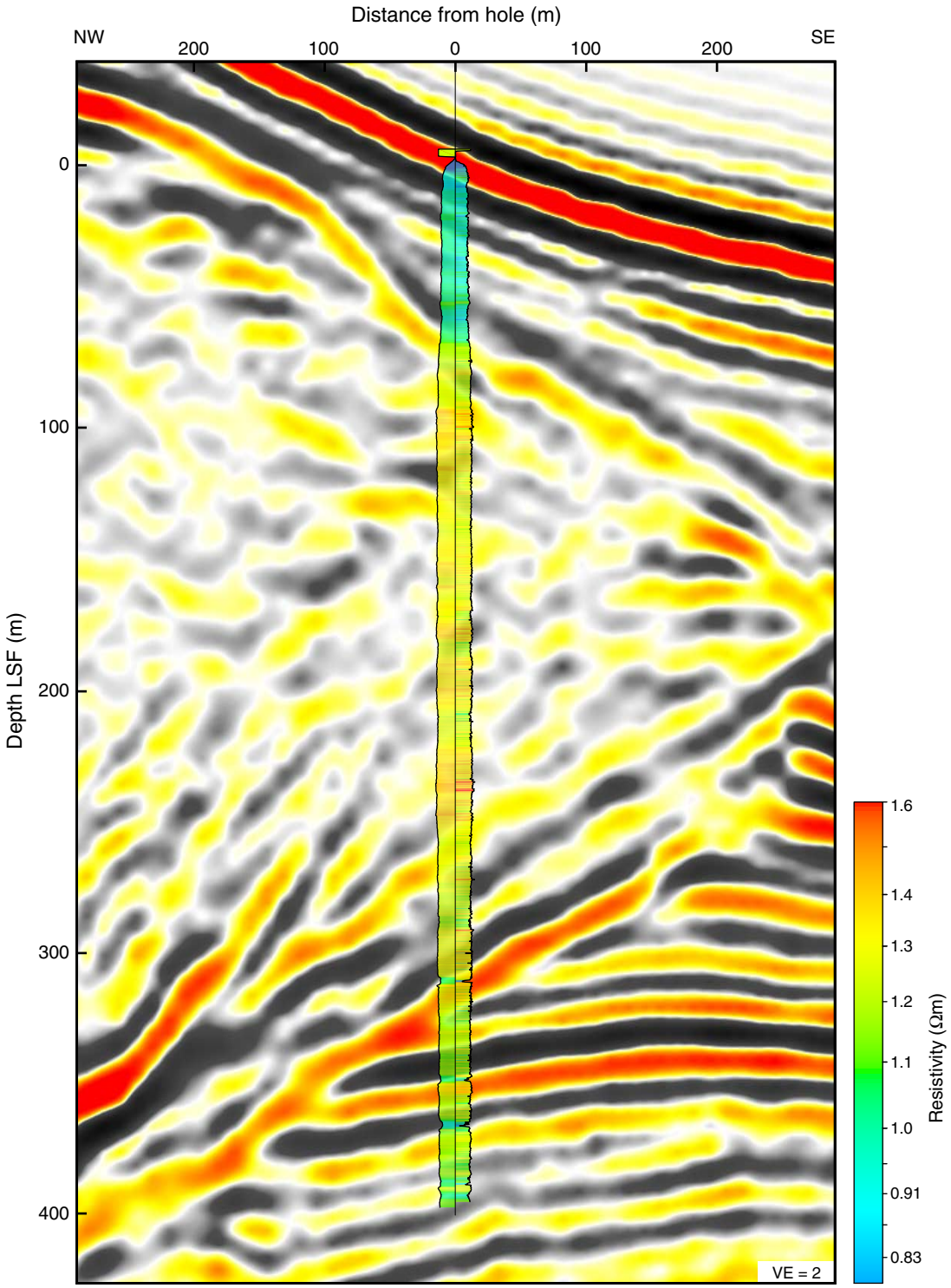

Figure F39. Caliper (hole diameter) log superimposed on check shot–corrected prestack depth-migrated seismic profile through Hole C0004B. LSF = LWD depth below seafloor, VE = vertical exaggeration.

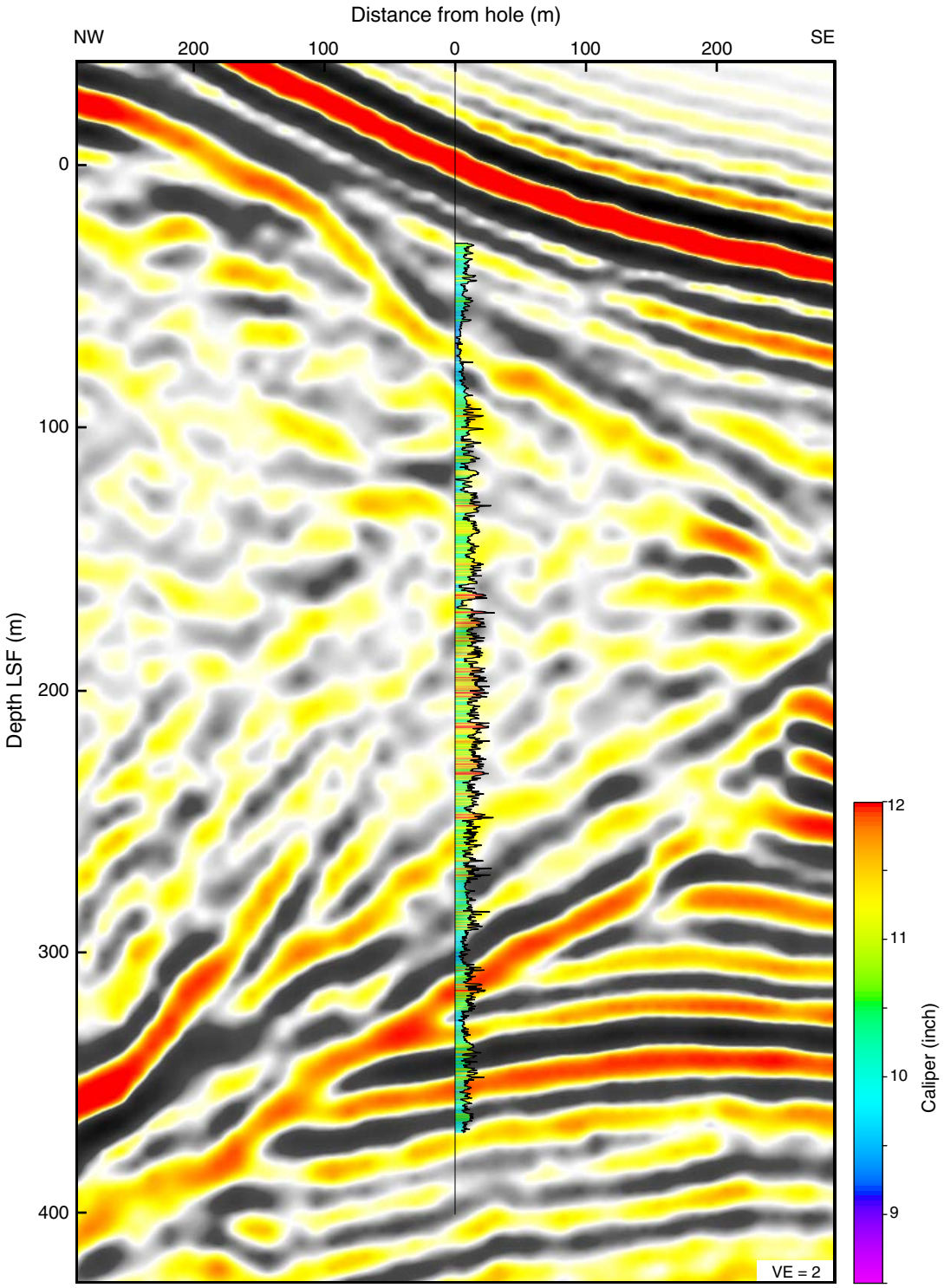

Figure F40. Check shot–corrected prestack depth-migrated seismic profile through Site C0004 at the logging Unit II/III boundary. Superimposed log is sonic velocity. Dashed lines = dipping and flat lying reflector packages described in the text. No vertical exaggeration. SSF = seismic depth below seafloor.

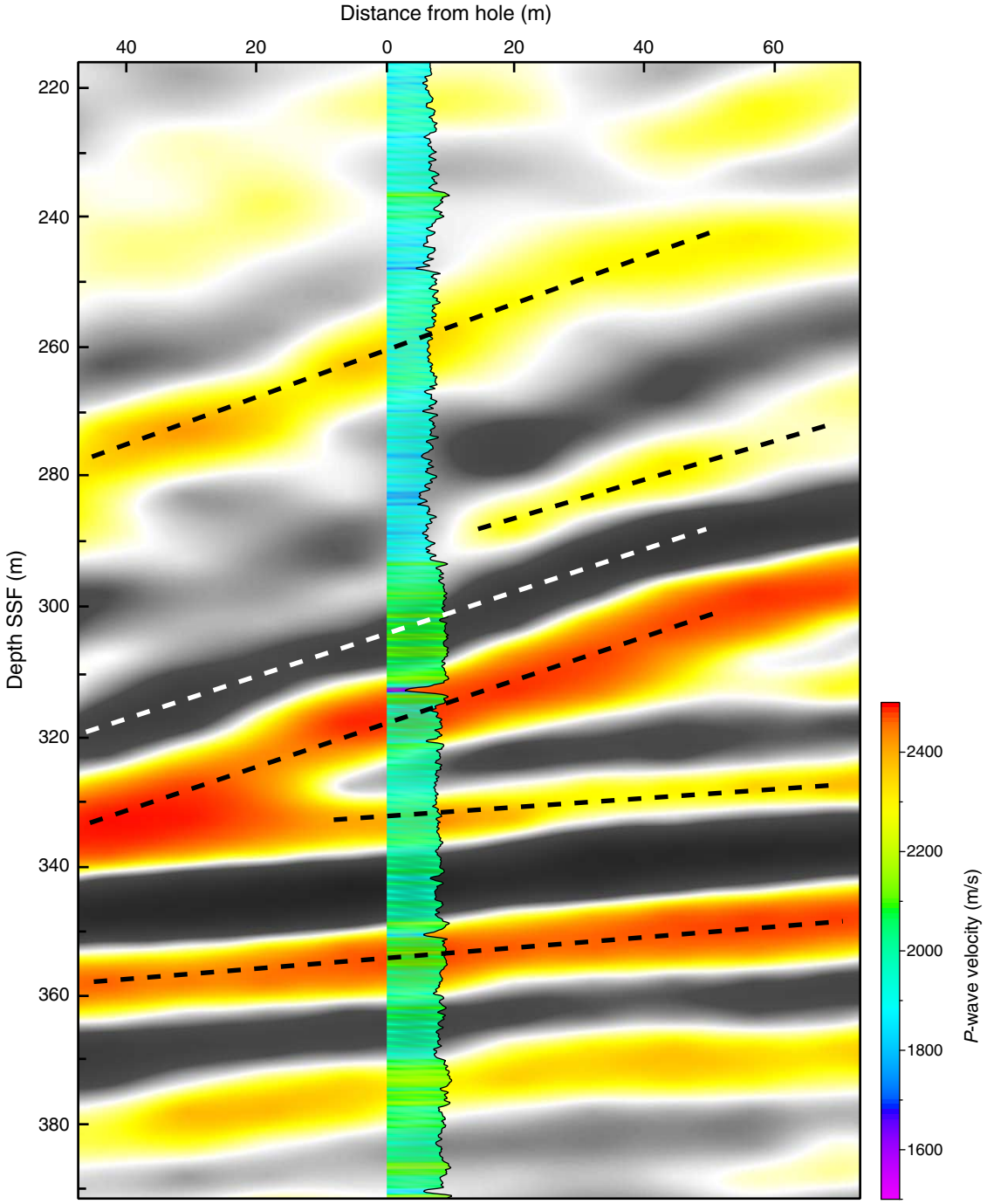

Figure F41. Check shot display showing clear first arrivals from seismicVISION tool. LSF = LWD depth below seafloor.

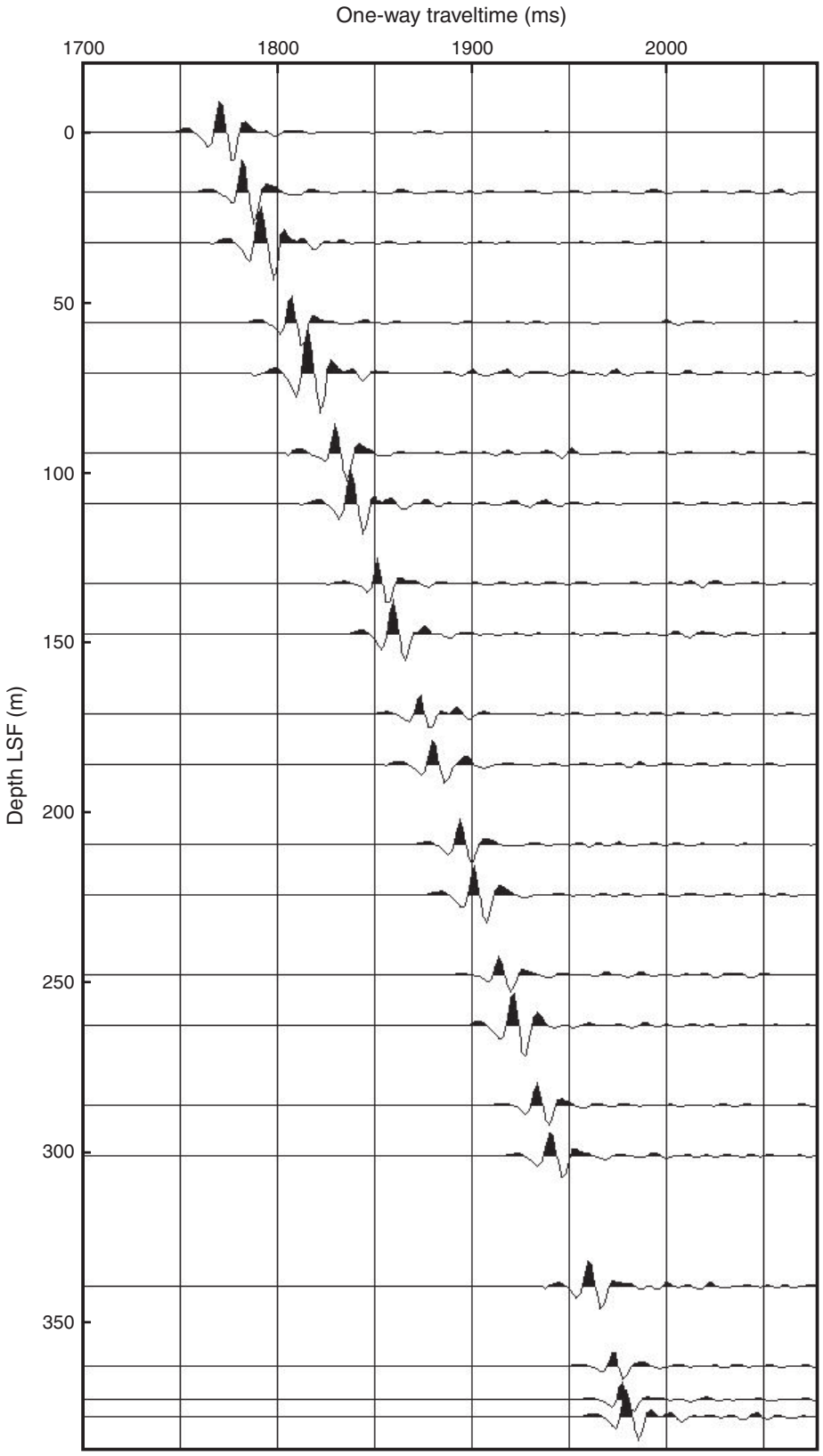

Figure F42. Smoothed check shot interval and real-time sonic log interval velocities. LSF = LWD depth below seafloor.

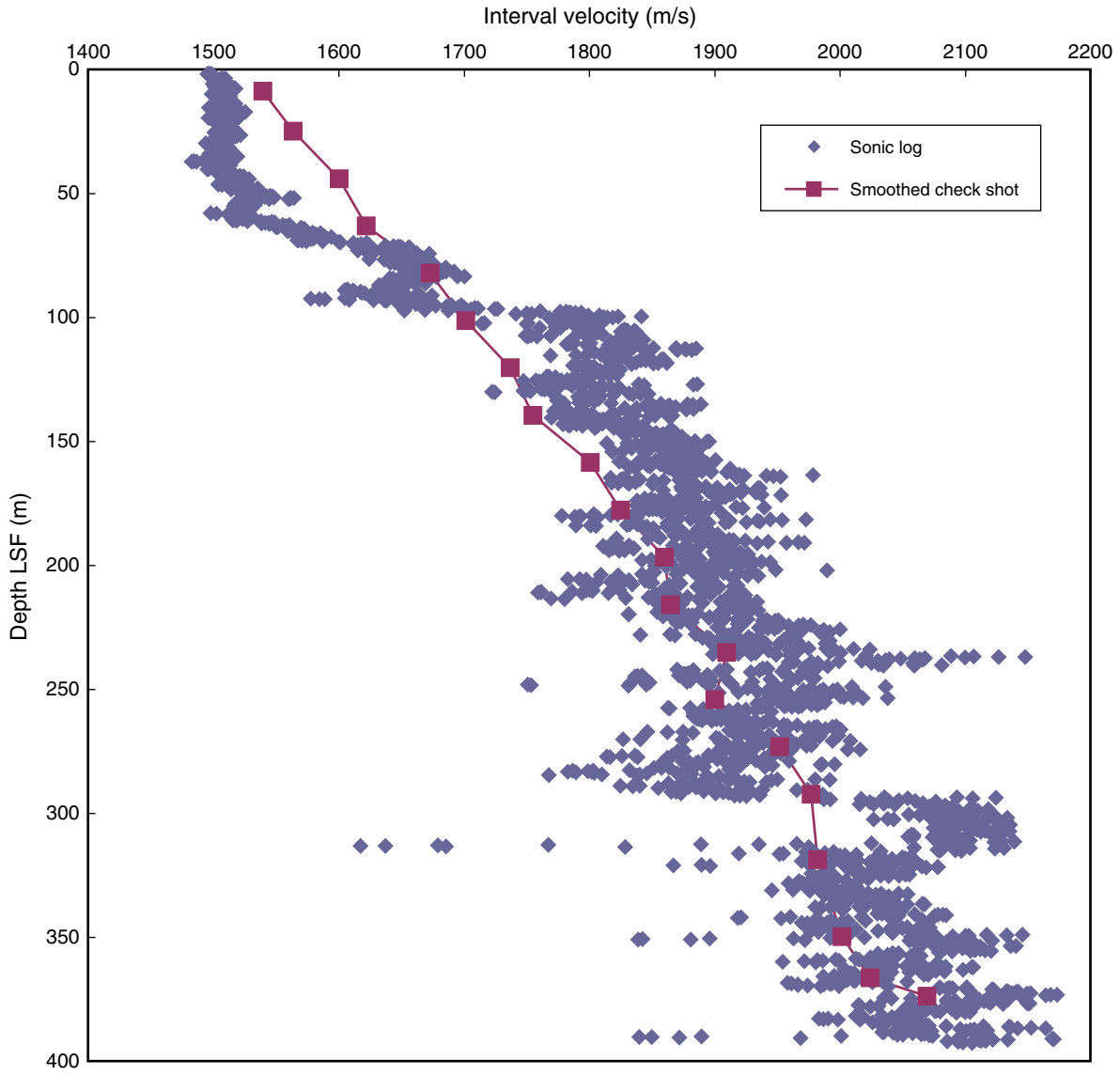

Figure F43. Synthetic seismogram generation for Site C0004. **A.** Time vs. depth curve based on check shot data. **B.** Sonic log in slowness. **C.** Pseudo-density log. **D.** Computed synthetic seismogram shown as five identical traces side by side. **E.** Reflection coefficients determined from the input sonic and density logs. **F.** 256 ms long, 0 ms lag deterministic wavelet used as a source wavelet. **G.** Fifteen traces of Inline 2674 closest to borehole to the northwest. **H.** Synthetic seismogram repeated with positive amplitude filled in red and negative amplitude filled in blue. **I.** Fifteen traces of Inline 2674 closest to borehole to the southeast. **J.** Ultrasonic caliper. **K.** Gamma ray log. Note lack of correspondence of high caliper values and sonic log, suggesting high quality of logs at this site. LSF = LWD depth below seafloor.

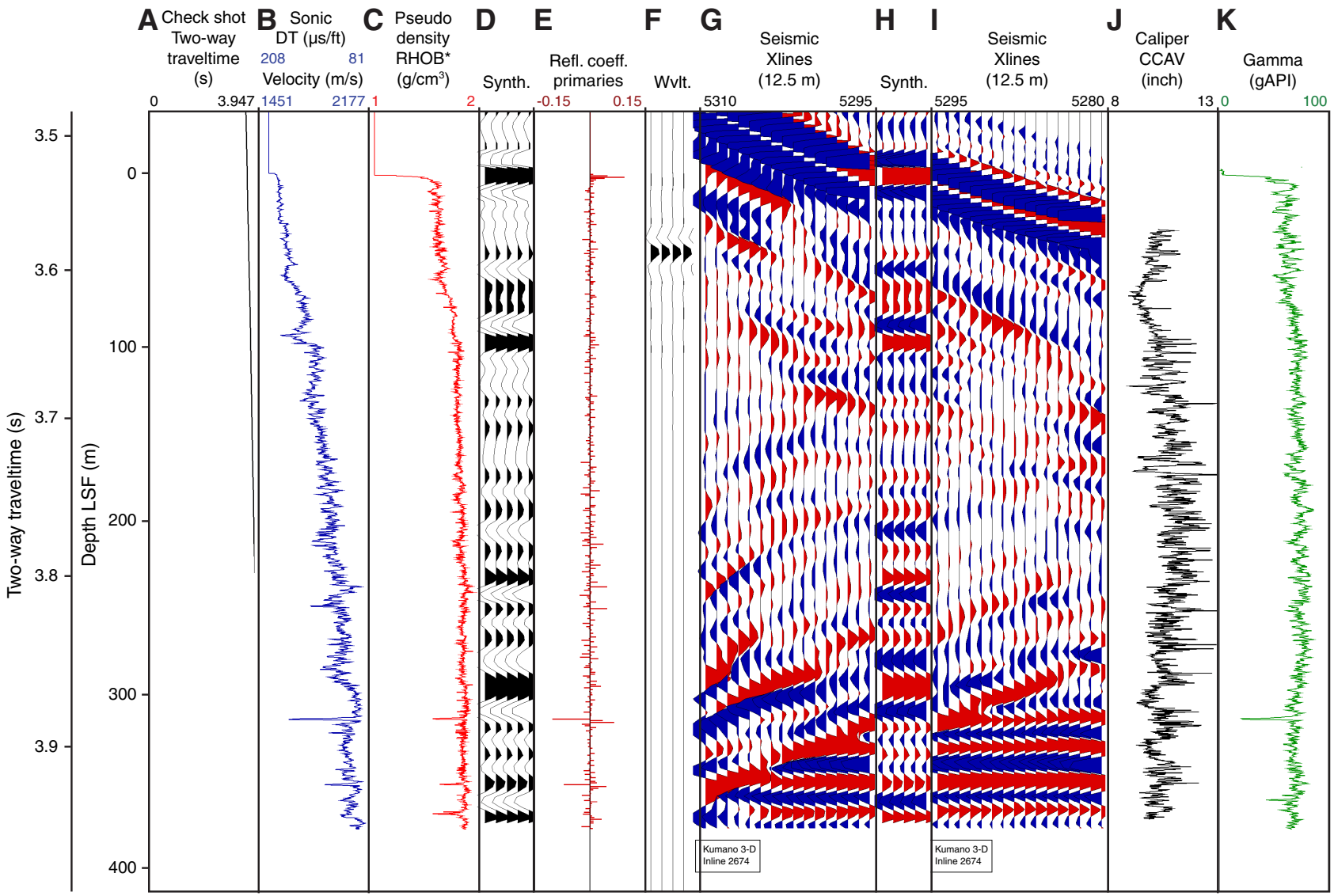

Table T1. Operations summary, Site C0004. (See table notes.)

Hole C0004A
Latitude: 33°13.2424′N
Longitude: 136°43.3349′E
Seafloor (drill pipe measurement from rig floor, m): 2660.5
Distance between rig floor and sea level (m): 28.5
Water depth (drill pipe measurement from sea level, m): 2632

Hole C0004B
Latitude: 33°13.2264′N
Longitude: 136°43.3461′E
Seafloor (drill pipe measurement from rig floor, m): 2665.5
Distance between rig floor and sea level (m): 28.5
Water depth (drill pipe measurement from sea level, m): 2637

Operation	Start Date (2007)	Start Local time (h)	Depth (m LSF) Top	Depth (m LSF) Bottom	Drilled (m LSF)	Comments
Hole C0004A pilot hole			0	400	400	8-1/2 inch pilot hole without MWD-LWD
ROV survey	31 Oct	2130				
Tag seafloor	1 Nov	0430				
Spud-in	1 Nov	0445				Jet-in to 78.5 m LSF and rotary drill to TD
Backream and sweep	1 Nov	1100				Short trip from 2888 to 2736 m DRF
Reach total depth	1 Nov	1845				Pump sweep and spot kill mud
Pull tools out of hole	1 Nov	1930				
Hole C0004B LWD hole	2 Nov	1415	0	400	400	8-1/2 inch LWD (GVR-sonic-SVWD-MWD-APWD-ADN)
ROV survey	2 Nov	1600				
Tag seafloor	2 Nov	1830				
Spud-in						
Ream and sweep	3 Nov	0345				Wiper trip between 2900 and 2765 m DRF
Reach total depth	3 Nov	1230				Pull back one stand, relog to TD, pump kill mud
Pull tools out of hole	3 Nov	1530				
Recover tools on the rig floor	3 Nov	1715				
Recover data	4 Nov	0000				Download all data

Notes: LSF = LWD depth below seafloor. MWD = measurement while drilling, LWD = logging while drilling. ROV = remotely operated vehicle. TD = total depth. DRF = drillers depth below rig floor. GVR = geoVISION resistivity tool, sonic = sonic while drilling (sonicVISION), SVWD = seismicVISION while drilling (seismicVISION), APWD = annular pressure while drilling, ADN = Azimuthal Density Neutron tool (adnVISION).

Table T2. Bottom-hole assembly, Hole C0004B. (See table notes.)

BHA component	Length (m)	Cumulative length from bit (m)
PDC bit	0.350	0.350
Stabilizer/float sub	1.500	1.850
Crossover sub	0.615	2.465
geoVISION	3.084	5.549
sonicVISION	7.624	13.173
Power pulse	8.496	21.669
seismicVISION	4.640	26.309
adnVISION	6.098	32.407
Crossover sub	0.610	33.017
6-3/4 inch drilling collar	9.310	42.327
6-3/4 inch drilling collar	9.313	51.640
6-3/4 inch drilling collar	9.310	60.950
6-3/4 inch drilling collar	9.292	70.242
6-3/4 inch drilling collar	9.312	79.554
6-3/4 inch drilling collar	9.314	88.868
6-3/4 inch drilling collar	9.310	98.178
6-3/4 inch drilling collar	9.316	107.494
Jar	10.215	117.709
6-3/4 inch drilling collar	9.310	127.019
Crossover sub	0.611	127.630
Crossover sub	0.605	128.235
Heavy pipe	37.856	166.091
Heavy pipe	37.876	203.967
Heavy pipe	37.884	241.851
Heavy pipe	37.846	279.697
Crossover sub	0.910	280.607

Notes: BHA = bottom-hole assembly. PDC = polycrystalline diamond compact.

Table T3. Quality control characteristics and sonic log data, Hole C0004B. (See table notes.)

Depth interval (m LSF)				
Top	Bottom	Zone	Quality	Comments
0	94.5	2	1	Formation arrival cannot be distinguished from the mud arrival using the MP wide processed data. Data processed using the leaky-P process were successful in suppressing the mud arrival and obtaining reasonably good picks.
94.5	389.5	1	1	High quality, continuous data, picked using the wide processed data.

Notes LSF = LWD depth below seafloor. MP = mixed processing.

Table T4. Quality control characteristics and resistivity image data, Hole C0004B. (See table notes.)

Depth interval (m LSF)		
Top	Bottom	Comments
—	56	Start GVR rotation, beginning of image log
56	61	Good, but lateral stripes of missing pixels are common
61	94	Very good quality with locally missing pixels
94	95	Vertical stripping of data, loss of image
95	396	Excellent
—	396	End of GVR image log

Notes: LSF = LWD depth below seafloor. GVR = geoVISION resistivity tool.

Table T5. Logging units, Site C0004. (See table notes.)

Depth (m LSF)	Logging Unit	Logging Subunit	Interpretation	Log response
0–67.9	I		Slope sediments, hemipelagic mud	Variable gamma ray, low resistivity
67.9–96.2	II	A	Mass transport deposits	Increasing gamma ray frequency, increasing ring and button resistivity
96.2–160.3		B	Hemipelagic mudstone	Constant high-frequency gamma ray, constant resistivity baselines, increasing velocity
160.3–236.4		C		Cycles in natural gamma ray values, variable resistivity, increasing velocity
236.4–323.8		D		Decreasing natural gamma ray values, repeated intervals of decreasing resistivity and velocity
323.8–TD	III		Underthrust sediments, hemipelagic mud with thin sandy layers	Decreasing natural gamma ray values, variable resistivity, relatively constant velocity

Notes: LSF = LWD depth below seafloor. TD = total depth.

Table T6. Breakout orientation characteristics, Sites C0001 and C0004. (See table note.)

Site	Mean	Number of samples	Standard deviation	95% confidence interval
C0004	50	1289	16	0.86
C0001	66	1111	14	0.82

Note: Although standard deviations overlap between sites, the 95% confidence limits are both <1 degree (19 out of 20 times, sampling the same number of samples out of each population would result in a value within 1 degree of the mean value).

Table T7. Dips and dip directions of the boundaries of seismic packages and two footwall reflectors, Site C0004. (See table notes.)

	Depth SSL (m)	Dip (°) Direction	Dip (°) Angle
Base of slope	2702	165	14
Top of splay	2895	142	15
Bottom of splay	2951	307	11
Footwall 1	2978	248	0
Footwall 2	2998	247	2

Notes: Position of each reflection is indicated in Figure F34. To estimate the dips and dip directions, we used the three-dimensional (3-D) prestack time-migrated seismic volume combined with the velocities provided by the check shot data. Dip directions for reflectors were determined by digitizing a transect ~200 m long centered on the borehole orthogonal to the two-way traveltime contours of each horizon. Dips were then calculated from the end points of these digitized transects, with time to depth correlation computed using the check shot velocities. These estimated dips may have errors which can be caused by our use of a one-dimensional velocity model used for time-depth conversion. This analysis will be improved by using the fully 3-D prestack depth-migrated data now being processed. SSL = seismic depth below sea level.

Table T8. Check shot raw and smoothed traveltimes and calculated interval velocities, Site C0004. (See table notes.)

		Raw		Smoothed	
Depth* (m LSF)	Midpoint depth† (m LSF)	First arrival time* (ms)	Interval velocity† (m/s)	First arrival time* (ms)	Interval velocity† (m/s)
–0.01	8.76	1761.9	1458	1762.0	1540
17.54	24.89	1773.9	1710	1773.4	1564
32.24	44.00	1782.5	1477	1782.8	1600
55.76	63.06	1798.4	1663	1797.5	1622
70.36	82.15	1807.2	1726	1806.5	1673
93.95	101.27	1820.9	1739	1820.6	1701
108.58	120.39	1829.3	1752	1829.2	1737
132.20	139.49	1842.8	1809	1842.8	1755
146.77	158.57	1850.8	1693	1851.1	1801
170.36	177.66	1864.7	2304	1864.2	1825
184.96	196.77	1871.1	1673	1872.2	1860
208.58	215.95	1885.2	2087	1884.9	1865
223.31	235.06	1892.3	1778	1892.8	1910
246.80	254.12	1905.5	2246	1905.1	1900
261.44	273.25	1912.0	1851	1912.8	1952
285.06	292.37	1924.7	2127	1924.9	1977
299.69	318.82	1931.6	1922	1932.3	1982
337.95	349.76	1951.5	1948	1951.6	2002
361.57	366.32	1963.7	1782	1963.4	2024
371.08	373.77	1969.0	2832	1968.1	2070
376.46	—	1970.9	—	1970.7	—

Notes: Smoothed values were used in the generation of synthetic seismograms and time-depth conversion of seismic reflection profiles near the site. * = first arrival time picks associated with depths of observations, † = interval velocities associated with midpoints between depths of observations. LSF = LWD depth below seafloor. — = no data.